

LHCb实验上双粲味重子的寻找

(申请清华大学理学博士学位论文)

培 养 单 位 : 工 程 物 理 系

学 科 : 物 理 学

研 究 生 : 钟 亮

指 导 教 师 : 高 原 宁 教 授

二〇一四年四月

A search for Doubly Charmed Baryon

Ξ_{cc}^+ **at LHCb**

Dissertation Submitted to

Tsinghua University

in partial fulfillment of the requirement

for the degree of

Doctor of Science

in

Particle and Nuclear Physics

by

Liang Zhong

Dissertation Supervisor : Professor Gao Yuanning

April, 2014

关于学位论文使用授权的说明

本人完全了解清华大学有关保留、使用学位论文的规定，即：

清华大学拥有在著作权法规定范围内学位论文的使用权，其中包括：（1）已获学位的研究生必须按学校规定提交学位论文，学校可以采用影印、缩印或其他复制手段保存研究生上交的学位论文；

（2）为教学和科研目的，学校可以将公开的学位论文作为资料在图书馆、资料室等场所供校内师生阅读，或在校园网上供校内师生浏览部分内容；（3）根据《中华人民共和国学位条例暂行实施办法》，向国家图书馆报送可以公开的学位论文。

本人保证遵守上述规定。

（保密的论文在解密后应遵守此规定）

作者签名：_____

导师签名：_____

日 期：_____

日 期：_____

摘要

作为标准模型的一部分，夸克模型已经得到了充分的实验验证。双粲味重子是夸克模型所预言的，但是实验上还没有确切的证据。SELEX实验组观察到了双粲味重子的信号，但他们的结果没有被其他实验组验证。寻找双粲味重子有助于解决这一实验方面的不确定性。除此之外，双粲味重子在理论方面也有重要意义。许多模型都对双粲味重子的性质做出了预言，包括其质量，寿命和在LHC上的产生截面等。寻找并测量双粲味重子的性质可以检验这些模型。

位于欧洲核子研究中心(CERN)的大型强子对撞机(LHC)是世界上能量最高的加速器。LHCb实验是LHC上的四个大型探测实验之一。它是一个单臂前向谱仪，覆盖了2-5的赭速度区间，并具有良好的寻迹和粒子鉴别系统。它的主要目的是精确测量包含底夸克和粲夸克强子的CP破坏和稀有衰变。利用高能质子-质子对撞，LHC可以大量产生双粲味重子，其预计的产生截面达到100nb量级。本文将集中于 Ξ_{cc}^+ ，并使用 $\Xi_{cc}^+ \rightarrow (\Lambda_c^+ \rightarrow pK^-\pi^+)K^-\pi^+$ 来寻找这一重子。我们通过蒙特卡洛样本对这一衰变进行了研究，并使用神经网络优化了选择条件，并测量了 Ξ_{cc}^+ 相对于 Λ_c^+ 的产生截面的上限。由于 Ξ_{cc}^+ 的质量和寿命均未知，而这两个变量都将影响效率进而影响产生截面的测量，我们给出了在不同的寿命假设下，相对截面上限随质量假设的变化曲线。2015年LHC将继续运行，LHCb的硬件触发将有很大的改善，我们将很有希望观测到 Ξ_{cc}^+ 和其他双粲味重子。

关键词：大型强子对撞机，双粲味重子，量子色动力学，粲强子谱

Abstract

As a part of the Standard Model (SM), the quark model has been efficiently tested by experiment. The doubly charmed baryons are predicted by the quark model, but until now there is no solid proof for their existence. The SELEX collaboration reported the signal of doubly charmed baryons, but their results were not confirmed by other experiments. To search for the doubly charmed baryon helps to clear up the experimental situation. Besides, the doubly charmed baryons are also important for theory. Many models predict the properties of the doubly charmed baryons, including their mass, lifetime and the production cross-section at the LHC. Measuring the properties of doubly charmed baryons put a crucial test on these models.

The large hadron collider at CERN is the most power particle accelerator in the world. LHCb is one of the four major experiments at the LHC. It is a single-arm forward spectrometer covering the pseudorapidity range $2 < \eta < 5$, designed for precise measurements of CP violation and rare decays in the hadrons containing b or c quarks. Using the high energy proton-proton collisions, the doubly charmed baryons are expected to be copiously produced at a cross-section of 100 nb level at the LHC. This thesis focuses on Ξ_{cc}^+ and searches through $\Xi_{cc}^+ \rightarrow (\Lambda_c^+ \rightarrow pK^-\pi^+)K^-\pi^+$. The decay is studied with MC samples and the selection criteria are optimised using a neural network. The upper limits on the relative production cross-section of Ξ_{cc}^+ to Λ_c^+ are measured. Since the efficiency depends on the mass and lifetime of Ξ_{cc}^+ , which are considered unknown in this thesis, the upper limits are given as a function of mass hypotheses for five different lifetime hypotheses. In 2015 the LHC will restart collision and the hadronic trigger will be much improved at LHCb, it is very hopeful that Ξ_{cc}^+ and other doubly charmed baryons can be observed.

Key words: LHC; Doubly Charmed Baryon; QCD; Charmed Baryon Spectroscopy

目 录

第 1 章 Introduction	1
1.1 A brief history of particles	1
1.2 The Standard Model	3
1.2.1 The Quantum Chromodynamics	3
1.2.2 The Unification of Electroweak Theory	5
1.3 The Doubly Charmed Baryon Ξ_{cc}^+	6
1.3.1 The quark model	6
1.3.2 The predictions for Ξ_{cc}^+	6
1.3.3 Prediction for Ξ_{cc}^+ mass	8
1.3.4 Prediction for Ξ_{cc}^+ lifetime	9
1.3.5 Ξ_{cc}^+ production cross-section at LHCb	10
1.3.6 Decay modes of Ξ_{cc}^+	13
1.4 Experimental status	14
1.4.1 The SELEX results	14
1.4.2 The FOCUS results	15
1.4.3 The Belle results	15
1.4.4 The BaBar results	15
第 2 章 The LHCb Experiment	23
2.1 The Large Hadron Collider at CERN	23
2.2 The LHCb detector	25
2.2.1 The tracking system	27
2.2.2 The PID system	37
2.3 The LHCb trigger	50
2.3.1 Level-0 trigger	50
2.3.2 High-Level Trigger	51
2.3.3 The TISTOS method	52
2.3.4 The performance of the trigger system	53
2.4 The LHCb software framework	53

第 3 章 The Ξ_{cc}^+ analysis in 2011	57
3.1 Strategy	57
3.2 Data Sample	58
3.3 $\Xi_{cc}^+ \rightarrow \Lambda_c^+ K^- \pi^+$ reconstruction	59
3.4 Selections	60
3.4.1 Stripping and offline cuts	60
3.4.2 Cut-based offline selection	61
3.4.3 Multivariate analysis	64
3.4.4 Trigger requirements	68
3.5 Efficiency ratio determination	70
3.5.1 Ratio of acceptance efficiencies	71
3.5.2 Ratio of stripping and offline efficiency	72
3.5.3 Ratio of PID cut efficiencies	75
3.5.4 MVA cut efficiency	80
3.5.5 Trigger efficiency	80
3.5.6 Summary	83
3.5.7 Note on efficiency of Ξ_{cc}^+ mass window	83
3.6 Yield determination	83
3.6.1 Fit to the Λ_c^+ control mode	83
3.6.2 Fit to the Ξ_{cc}^+ signal in Monte Carlo	84
3.6.3 Yield measurement procedures for Ξ_{cc}^+ in data	85
3.6.4 Decays via a Σ_c	92
第 4 章 Systematic Uncertainties	94
4.1 Tracking efficiency uncertainty	94
4.2 Multiple Candidates	95
4.3 Stripping, offline cuts and MVA efficiency	96
4.4 PID calibration	98
4.4.1 The calibration result	98
4.4.2 The kinematic correlation between final tracks	98
4.4.3 The multiplicity of MC	99
4.4.4 The calibration method itself	105
4.4.5 Summary for PID efficiency	105
4.5 Trigger efficiency	106
4.6 Systematics related to yield measurement	106
4.7 Decay models	107
4.8 Summary	109

第 5 章	Variation of the Efficiency Ratio	110
5.1	Variation of the efficiency ratio with Ξ_{cc}^+ mass	110
5.1.1	Effects from variation of kinematic distributions	110
5.1.2	Correction for Ξ_{cc}^+ mass window	112
5.2	Variation of the efficiency ratio with lifetime	113
5.2.1	Ratio of acceptance efficiency	114
5.2.2	Ratio of stripping and offline efficiency	114
5.2.3	Ratio of PID efficiencies	114
5.2.4	Ratio of MLP efficiency	115
5.2.5	Ratio of L0 efficiency	115
5.2.6	HLT1 and HLT2 efficiency	116
5.2.7	The systematic error for different lifetime	116
5.2.8	Single event sensitivity for different lifetimes	117
第 6 章	Upper Limit Calculation	118
第 7 章	Results	120
第 8 章	Conclusion	127
8.1	Overview of current experimental status	127
8.2	Prospect of Ξ_{cc}^+ search at LHCb and Belle II	127
参考文献	130
致 谢	137
声 明	138
个人简历、在学期间发表的学术论文与研究成果	139

第 1 章 Introduction

The thesis describes the work of searching for the doubly charmed baryon Ξ_{cc}^+ with pp collision data collected at the LHCb detector in 2011. The contents are organized as below: Chapter 1 describes a brief introduction to the theoretical background of the doubly charmed baryons, followed by an overview of the collider and the spectrometer where the data is collected in 2. The selection criteria for the $\Xi_{cc}^+ \rightarrow \Lambda_c^+ K^- \pi^+$ decay are given in Chapter 3, and the associated systematic uncertainties are discussed in Chapter 4. The efficiency variation with Ξ_{cc}^+ mass and lifetime are considered in Chapter 5. The upper limit setting procedure are given in Chapter 6. Chapter 7 presents the results for this search and outlooks the further Ξ_{cc}^+ and other doubly charmed baryons search at LHCb. Finally Chapter 8 summarizes the results.

1.1 A brief history of particles

As Einstein once said, “The most incomprehensible thing about the universe is that it is comprehensible”. One of the amazing achievements of the science is that we understand the universe at a very basic level. The adventure dates back to several thousand years ago, and many great theories to explain the universe emerged between this period. The most important idea of these is the atomic theory, which considers all the matter to consist of indivisible ingredients called atoms. Although many developments have been made for the atomic theory since its first appearance, the essence of the theory has been kept till now.

About 500 B.C., Greek philosophers Leucippus and Democritus, raised the idea that the world is composed of two fundamental ingredients: inseparable atoms and empty void, which is generally regarded as the birth of the atomic theory^[1]. Similar views are advocated by Epicurus and later (A.D 55) by Lucretius. Unfortunately, due to lack of experimental supports, there was no substantial progress in the atomic theory since then until the nineteenth century, when John Dalton proposed all matter are made of atoms to explain the simple number ratio between the elements reacts^[2]. This marks the beginning of the modern atomic theory. Atoms were considered as the most elementary particles for a long time until 1897, when J.J. Thomson discovered the electron in cathode

rays^[3], which disproved the indivisibility of atoms. To explain the electric neutrality of atoms, Thomson introduced the plum pudding model, in which the atom was composed of electron embedded in a uniform sea of positive charge. However, in 1911 Rutherford performed the famous gold foil scattering experiment, which manifested that instead of distributed uniformed, the positive charge are concentrated in a tiny volume called atomic nucleus^[4]. The elementary particles were then changed to the electrons and the nucleus.

In 1917 Rutherford demonstrated that the hydrogen nucleus is present in other nuclei, which illustrates that the atom nucleus is, again, divisible. Later the other component of the nucleus, the neutron, was discovered in 1932 by Chadwick^[5]. The discovery of protons and neutrons explains the element periodic table in a very natural and beautiful way. Apart from protons and neutrons, Hideki Yukawa also predicted the existence of new particles called pions to be the mediating particle of the strong force inside nucleus^[6]. If pions were discovered, then the whole picture of elementary particles would be complete.

A new particle did be discovered in cosmic radiation by Carl Anderson and Seth Neddermeyer in 1936^[7], and it also has a mass very close to Yukuwa's predictions. It was therefore initially thought to be the particle anticipated by Yukawa, but later it was proved not have the desired properties – it barely interacts with nucleons. The true pion was found by Powell, Lattes and Occhiolini in 1947^[8]. The existence of muon, the particle discovered by C.Anderson and S.Neddermeyer, was really unexpected and puzzled physicists. Even stranger, shortly after the discovery of pion, more unforeseen particles were identified in cosmic rays. In the same year, particles called “V0” were discovered through cloud chamber^[9]. In 1951 as many as 15 new particles were added to the “elementary” particle list. The explosion era of elementary particles came with the construction of energetic accelerators. In 1960s there were more elementary particles than the chemical elements. To consider all these particles as elementary was quite unnatural and disobeys the philosophy of the atomic theory. The conservation of strangeness also indicated there could be a classification scheme similar to the periodic table for the crowded world of subatomic particles.

In 1961 Murray Gell-Mann and Yuval Ne'eman made a important progress in the hadron classification. They proposed a model called the Eightfold Way^[10] to organize all the hadrons discovered. What made the model success is that it not only classify the hadrons to a few multilets, but also correctly predicted the existence and the properties

of a new baryon, now known as Ω^- . At the same year a more concise theory called the quark model was advanced by Gell-Mann and George Zweig independently^[11,12]. The new model included only three particles called quarks, but explained the pattern of the hadrons in a elegantly way. The order of the subatomic world was restored. The existence of quarks were verified by deep inelastic scattering (DIS) experiments at SLAC in 1969^[13,14]. Quarks are considered as elementary particles. At that time only three quarks were identified, but Sheldon Glashow, John Iliopoulos and Luciano Maiani advocated the existence of a fourth quark to explain the suppression of the “neural current” weak processes between quarks of different flavour^[15]. In 1974, a new particle, now known as the J/ψ meson, was discovered by Samuel Ting and Burton Richter independently^[16,17]. Later experiments confirmed that J/ψ is the evidence of charm quark. But this is not the end of the story. Two years later in 1976, Makoto Kobayashi and Toshihide Maskawa predicted the existence of the third generation of quarks to explain the CP violation in quark sector^[18]. In the next year, the bottom quark was discovered by Leon M. Lederman^[19]. The top quark, however, is so heavy that it kept behind the scene until 1995^[20,21]. Using these quarks, the quark model predicted the existence of hadrons and most of them have been discovered, except the ones which are difficult to produce.

1.2 The Standard Model

The current picture of particle physics is given by the Standard Model (SM), which is a Quantum Field Theory (QFT) that describes the properties of fundamental particles. The theory is built on the local gauge symmetry $SU(3)_C \otimes SU(2)_L \otimes U(1)_Y$, where $SU(3)_C$ is the symmetry associated with the strong interaction, and $SU(2)_L \otimes U(1)_Y$ is the symmetry related to the electroweak interactions. Therefore the Lagrangian of the SM consists of two parts,

$$\mathcal{L}_{SM} = \mathcal{L}_{QCD} + \mathcal{L}_{EW} \quad (1-1)$$

1.2.1 The Quantum Chromodynamics

Quantum Chromodynamics (QCD) is the fundamental theory for the strong interaction, the interaction that combine quarks and gluons to hadrons. QCD is a non-abelian gauge theory based on the non-abelian gauge group $SU(3)$. Like QED, the theory for the electromagnetic interaction, QCD also has its charges called color and force carriers

called gluons. But the difference is that there are three kinds of colors and eight gluons in QCD, compared with one kind of charge and one photon in QED.

The Lagrangian of QCD is given by

$$\mathcal{L} = \bar{\psi}_q^i (i\gamma^\mu) (D_\mu)_{ij} \psi_q^j - m_q \bar{\psi}_q^i \psi_{qi} - \frac{1}{4} G_{\mu\nu}^a G^{a\mu\nu}, \quad (1-2)$$

where ψ_q^i is the Dirac field of the quark with flavour q and color index i , γ^μ is the Dirac matrix with a Lorentz vector index μ , m_q is the mass of the quark, $G_{\mu\nu}^a$ is the gluon field strength tensor for a gluon with color index a , and D_μ is the covariant derivative in QCD,

$$(D_\mu)_{ij} = \delta_{ij} \partial_\mu - ig_s t_{ij}^a A_\mu^a, \quad (1-3)$$

with g_s the strong coupling constant (we will return to this with more detail later), A_μ^a the gluon field with color index a , and t_{ij}^a proportional to the generator for the SU(3) group in the basic representation

$$\lambda^1 = \begin{pmatrix} 0 & 1 & 0 \\ 1 & 0 & 0 \\ 0 & 0 & 0 \end{pmatrix}, \lambda^2 = \begin{pmatrix} 0 & -i & 0 \\ i & 0 & 0 \\ 0 & 0 & 0 \end{pmatrix}, \lambda^3 = \begin{pmatrix} 1 & 0 & 0 \\ 0 & -1 & 0 \\ 0 & 0 & 0 \end{pmatrix}, \lambda^4 = \begin{pmatrix} 0 & 0 & 1 \\ 0 & 0 & 0 \\ 1 & 0 & 0 \end{pmatrix} \quad (1-4)$$

$$\lambda^5 = \begin{pmatrix} 0 & 0 & -i \\ 0 & 0 & 0 \\ i & 0 & 0 \end{pmatrix}, \lambda^6 = \begin{pmatrix} 0 & 0 & 0 \\ 0 & 0 & 1 \\ 0 & 1 & 0 \end{pmatrix}, \lambda^7 = \begin{pmatrix} 0 & 0 & 0 \\ 0 & 0 & -i \\ 0 & i & 0 \end{pmatrix}, \lambda^8 = \begin{pmatrix} \frac{1}{\sqrt{3}} & 0 & 0 \\ 0 & \frac{1}{\sqrt{3}} & 0 \\ 0 & 0 & \frac{-2}{\sqrt{3}} \end{pmatrix} \quad (1-5)$$

From the QCD Lagrangian the Feynman rules can be derived, as shown in Figure 1.1. Due to the non-abelian nature of QCD, gluons have self-coupling with triplet and quartic vertex.

The strong coupling runs logarithmically with the absolute energy scale, and is governed by the beta function:

$$Q^2 \frac{\partial \alpha_s}{\partial Q^2} = \frac{\partial \alpha_s}{\partial \ln Q^2} = \beta(\alpha_s), \quad (1-6)$$

where the beta function is defined as

$$\beta(\alpha_s) = -\alpha_s^2 (b_0 + b_1 \alpha_s + b_2 \alpha_s^2 + \dots), \quad (1-7)$$

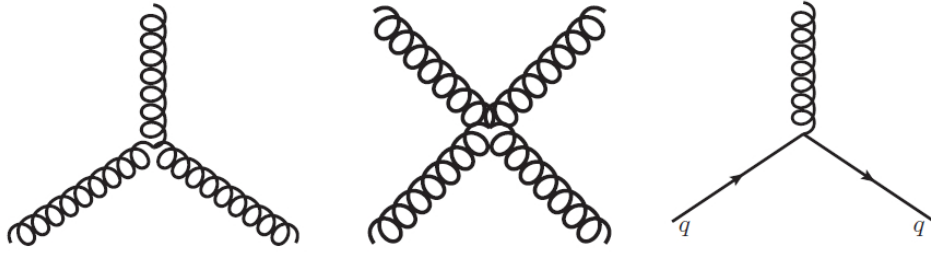


图 1.1 The Feynman rules for QCD. The curly lines are gluons and the solid lines are quarks. The first two diagrams shows triplet and quartic gluon self-interaction, respectively. The third diagram shown the gluon bremsstrahlung of the quark.

where b_0 , b_1 and b_2 are LO (1-loop), NLO (2-loop) and NNLO (3-loop) coefficients, respectively.

To illustrate the dependency explicitly, the strong coupling can be written in a way to compare with the reference scale $Q^2 = M_Z^2$,

$$\alpha_s(Q^2) = \alpha_s(M_Z^2) \frac{1}{1 + b_0 \alpha_s(M_Z^2) \ln \frac{Q^2}{M_Z^2} + \mathcal{O}(\alpha_s^2)}, \quad (1-8)$$

Now consider what happens if we run the coupling towards higher energies. The strong coupling decreases logarithmically with the energy scale, which is a remarkable result called asymptotic freedom. If we run the coupling to another direction, towards smaller energies, the coupling increases rapidly at scales below 1 GeV, which leads to another important feature of QCD called confinement. It is not possible to isolate a single quark or gluon.

1.2.2 The Unification of Electroweak Theory

Electromagnetic (EM) interaction governs the interaction between charged particles and photons, and weak interaction is the interaction caused by the emission or absorption of W and Z bosons. They have very different strength at low energy scale, but later it is found that the reason is that the weak interaction is mediated by massive bosons; the coupling constants of EM and weak interaction are at the same order. Actually the EM and weak interaction can be unified by the Higgs mechanism through the Spontaneous Symmetry Breaking (SSB)^[22–25]. The electroweak theory predicts the existence of W^\pm and Z as the mediate boson for the weak interaction, and the famous Higgs boson to assign mass to other particles.

The Lagrangian of EW interaction therefore reads

$$\begin{aligned}
 \mathcal{L}_{EW} &= \mathcal{L}_g + \mathcal{L}_f + \mathcal{L}_h \\
 &= -\frac{1}{4}W^{a\mu\nu}W_{\mu\nu}^a - \frac{1}{4}B^{\mu\nu}B_{\mu\nu} \quad (\equiv \mathcal{L}_g) \\
 &\quad + \bar{Q}_j i \not{D}_L Q_j + \bar{u}_{Rj} i \not{D}_R u_{Rj} + \bar{d}_{Rj} i \not{D}_R d_{Rj} + \bar{L}_j i \not{D}_L L_j + \bar{e}_{Rj} i \not{D}_R e_{Rj} \quad (\equiv \mathcal{L}_f) \\
 &\quad + |D_\mu h|^2 - \lambda \left(|h|^2 - \frac{v^2}{2} \right)^2 \quad (\equiv \mathcal{L}_h)
 \end{aligned} \tag{1-9}$$

Where \mathcal{L}_g is the kinetic term describing the propagation and interactions between the four gauge bosons W^a ($a=1,2,3$) and B , \mathcal{L}_f is the kinetic term for fermions (quarks and leptons). $\not{D}_L \equiv \gamma^\mu \partial_\mu + i\frac{g}{2}\tau^a \gamma^\mu W_\mu^a + i\frac{g'}{2}\gamma^\mu B_\mu$ and $\not{D}_R \equiv \gamma^\mu \partial_\mu + ig'\gamma^\mu B_\mu$ are the covariant derivatives for left handed fermions and right handed fermions respectively, where g and g' are the coupling constants. With the covariant derivatives the interactions (vertices) between gauge bosons and fermions are introduced. The subscript j in \mathcal{L}_f runs over three generation of fermions(see later): Q, L are left handed doublet for quarks $\begin{pmatrix} u_L \\ d_L \end{pmatrix}$ and leptons $\begin{pmatrix} e_L \\ \nu_L \end{pmatrix}$ respectively, while u_R, d_R, e_R are right handed singlet for quarks and leptons. The \mathcal{L}_h is Higgs field term describing Higgs self interaction and its interaction with gauge bosons, where $D_\mu \equiv \partial_\mu + i\frac{g}{2}\tau^a W_\mu^a + i\frac{g'}{2}B_\mu$.

1.3 The Doubly Charmed Baryon Ξ_{cc}^+

1.3.1 The quark model

As is described in Section 1.1, the quark model was developed to classify the proliferated “elementary particles”. Concerning the first four quarks, i.e. up, down, strange and charm, the quark model foresees two SU(4) multiplets of baryons which are made of these four quarks, as shown in Fig. 1.2. The baryons with zero or one charm quark are already discovered, while the baryons with two or three charm quarks are still in mystery or in controversy. These particles are expected to be difficult to produce, but their existence are highly expected because of the great success of the quark model.

This thesis will focus on the Ξ_{cc}^+ baryon, a baryon with the quark components of dcc .

1.3.2 The predictions for Ξ_{cc}^+

Until now the only experimental signal for the Ξ_{cc}^+ baryon is reported the SELEX collaboration, whose results do not agree with theoretical predictions well, especially for the lifetime and the production rate. In this circumstance, the properties of Ξ_{cc}^+ are

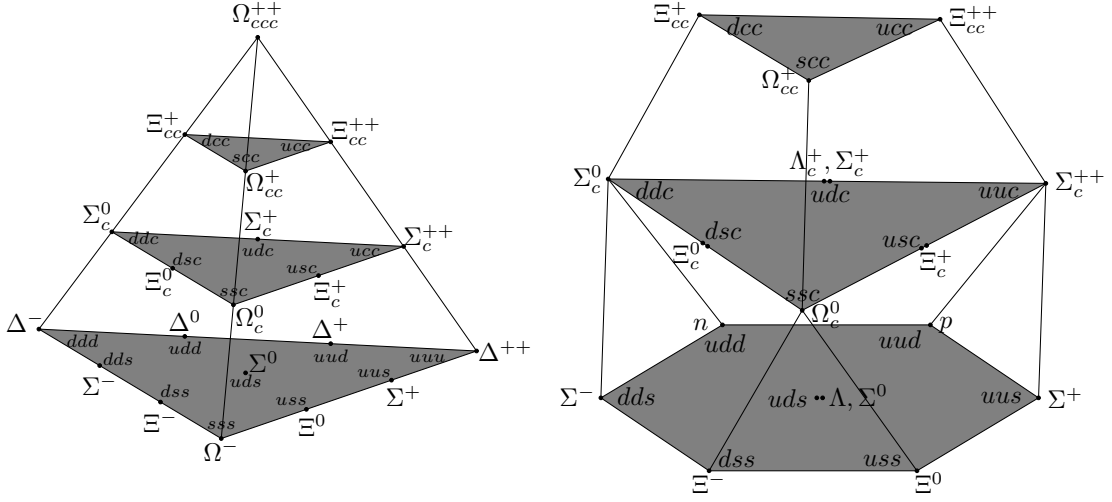


图 1.2 SU(4) multiplets of baryons made of u, d, s, and c quarks. The left plots shows the 20-plet with an SU(3) octet. The right plots shows the 20-plet with an SU(3) decuplet. All baryons in a multiplet have the same spin and parity

considered as unknown in this thesis. Information of Ξ_{cc}^+ properties used in this thesis is extracted from theoretical predictions.

In the theoretical review, doubly charmed baryons can be recognized as a Hydrogen-atom like system. As the mass of quark m_Q is much larger than the QCD scale Λ_{QCD} , the two heavy quarks are bounded into a small (compared with the QCD interaction scale) compact color triplet system. The light quark q then moves surround the tightly bound QQ pair. Based on this special property of doubly charmed baryons, there is a quite long list of literature on predictions of the properties of the Ξ_{cc}^+ baryon based on different theoretical treatments. We do not attempt to have a comprehensive review of the literature, but only some important models, i.e. Heavy Quark Effective Theory (HQET)^[26], potential model^[27-32] and QCD sum rules^[33,34]. The key points of them are described below.

HQET is an effective theory developed for calculation of hadron systems containing a single heavy quark. It provides a simplified picture of processes where a heavy quark interacts with light degrees of freedom by the exchange of soft gluons^[26]. This technique can also be applied to doubly charmed baryons system as doubly charmed baryons have similar structures, except that the diquark in doubly charmed baryons should be taken as a color anti-triplet. Since the mass of charm quark is larger than the QCD energy scale Λ , doubly charmed baryons have an additional flavour symmetry and a spin symmetry^[35,36]. The group theory of these symmetry can make model independent predictions concerning

weak decays of heavy hadrons. HQET therefore allows to calculate physical parameters by a systematic $1/m_Q$ expansion.

QCD sum rule is a technique that provides model independent predictions for hadronic parameters^[37]. The principle of the QCD sum rule is to connect the bound state problem with the short-distance calculable amplitudes. The idea is to start at short distances and move towards larger distances, confinement effects become important, perturbative methods starts to fail and resonances emerge which reflect the fact that gluons and quarks are confined within hadrons^[38]. On one hand the correlation function can be expanded by inserting in a full set of intermediate hadronic states, and the spectral function can be related to the expansion by the dispersion relations. On the other hand the correlation function can be decomposed by the operator product expansion. where coefficients contain short distance contribution and can be calculated in terms of the Lagrangian parameters of the theory with perturbative method. Long distance effects will show up in higher dimensional operators of the expansion, as the vacuum expectation value of gluons and quarks, which is put in by hand, i.e. the experimental results.

The potential model is another approach to predict the mass spectrum of the doubly charmed baryons. The idea is to construct a reasonable potential for the diquark and the baryon, then solve the corresponding Schrödinger equation to obtain the mass spectrum and physics parameters. This method has a clear physical picture and is relatively easy for calculation. Nonetheless it is not a fundamental theory, but only an effective phenomenological model. The predictions of the potential model have discrepancies with the experimental results since non-perturbative QCD and high order corrections are not dealt with but replaced by one simple potential. The results of the potential result highly depend on the potential adopted. The key point is therefore to construct a potential with as much information as possible. For the predictions of doubly charmed baryon, there are various choices for the potential, e.g. relativistic quark model^[27,28] and the non-relativistic quark model^[29–32].

It should be noted that these models are not mutual excluded, instead, in many situations they are combined.

1.3.3 Prediction for Ξ_{cc}^+ mass

The simplest possible approach to predict the mass of doubly charmed baryons is to replace the s in a known charmed baryon with one c quark, and get the difference from

other similar scenarios^[39]. Below is an example for this extrapolation.

$$m(\Xi_{cc}^+) = m(\Xi_c^0) + (m(\Xi_c^0) - m(\Xi^-)) = 2 \times 2471 - 1322 = 3620 \text{ MeV}/c^2 \quad (1-10)$$

where the quark components for these baryons are $\Xi_{cc}^+ : dcc$, $\Xi_c^0 : dsc$, and $\Xi^- : dss$. The true value is expected to be a bit smaller, since the relativistic interaction between cc should be smaller than that of cs . This is not an accurate estimate, but it does give a somewhat sensible result.

The rigorous calculation described in the previous section yield mass predictions major in the range $3500 - 3700 \text{ MeV}/c^2$ ^①, as listed in the Table 1.1.

表 1.1 Theoretical predictions for Ξ_{cc}^+ mass

Reference	Method	Ξ_{cc}^+ mass[MeV/c^2]
[40]	QCD sum rule	3570
[41]	QCD sum rule	3560
[28]	Potential model	3510
[42]	MIT bag model	3520
[43]	Potential model	3579
[44]	Potential model	3676
[30]	Potential model	3612
[45]	Lattice QCD	3608
[46]	Lattice QCD	3549

1.3.4 Prediction for Ξ_{cc}^+ lifetime

In the limit of infinite heavy quark mass, HQET predicts the lifetime of heavy hadrons with the same heavy quark flavour should be equal except corrections from the phase space. This so called ‘spectator ansatz’^[47] is well justified by the lifetime of b hadrons^[48]. However, since the mass of c is not heavy enough, non-spectator effects also give significant contributions to the decay widths^[49]. The non-spectator effects mainly consist of two contributions, Pauli interference (PI), which emerges from the interference between different diagrams of c decay, and weak annihilation between the heavy quark with the light valance antiquark for mesons or weak scattering with the valance quarks for baryons. The total width of Ξ_{cc}^+ can be roughly estimated^[50]

① There are calculations yielding masses larger than $4000 \text{ MeV}/c^2$, but technically it is difficult to blind this large mass range. Therefore these predictions are not considered in this thesis

$$\Gamma_{\text{tot}}[\Xi_{cc}^+] \approx 2\Gamma_c[\Xi_{cc}^+] + \Gamma_{\text{WS}}[\Xi_{cc}^+] \quad (1-11)$$

where $\Gamma_c[\Xi_{cc}^+]$ is the c spectator contribution corrected by the couple effects, and $\Gamma_{\text{WS}}[\Xi_{cc}^+]$ is the weak scattering contribution of c and d . The weak scattering contribution is found to be as large as 60%^[41]. The estimation gives the lifetime

$$\tau[\Xi_{cc}^+] = 0.16 \pm 0.05 \text{ ps} \quad (1-12)$$

More detailed analyses give predictions of the lifetime of Ξ_{cc}^+ at the same order, as listed in Table .

表 1.2 Theoretical predictions for Ξ_{cc}^+ lifetime

Reference	Ξ_{cc}^+ lifetime[fs]
[51]	110
[41]	120
[52]	220
[53]	200
[49]	250

Unfortunately, a Ξ_{cc}^+ baryon with a lifetime of this order cannot have significant displaced vertex at LHCb, therefore there be huge prompt background. To facilitate the selection optimisation, the lifetime value we choose in the Monte Carlo is 333 fs, a bit larger than the predictions. However, the point other lifetime hypotheses will be studied by lifetime weighting, as described in Section ??.

1.3.5 Ξ_{cc}^+ production cross-section at LHCb

In general, doubly charmed baryons are formed in three steps according to the time scale of the reaction:

1. Produce two c quarks through collisions.
2. Bind these two c quarks to a diquark, either $(cc)_3[{}^3S_1]$ or $(cc)_6[{}^1S_0]$.^①
3. The diquark hadronizes into a doubly charmed baryon.

① In current literature some references only considered the diquark in $(cc)_3[{}^3S_1]$ configuration^[54–56], and some consider the diquark in $(cc)_3[{}^3S_1]$ or $(cc)_6[{}^1S_0]$ configuration^[57,58]. The cross-section with both the configurations considered is adopted in this thesis.

The first step is contributed by several subprocesses, including $g + g \rightarrow c\bar{c}\bar{c}$, $g + c \rightarrow c\bar{c}$, $c + c \rightarrow ccg$, and $q + \bar{q} \rightarrow c\bar{c}\bar{c}$ ^[58], which are can be calculated with the perturbation technique^① At collider experiments, *e.g.* LHC, the gluon-gluon fusion diagrams dominate the production, and quark-antiquark annihilation diagrams can be ignored^[54,58]. Using pQCD factorization theorem and the general-mass variable-flavor-number (GM-VFN) scheme, the hadronic production cross-section of two c quarks can be formulated as below:

$$\begin{aligned}
 \sigma &= F_{H_1}^g(x_1, \mu) F_{H_2}^g(x_2, \mu) \otimes \hat{\sigma}_{gg \rightarrow \Xi_{cc}}(x_1, x_2, \mu) \\
 &+ \sum_{i,j=1,2; i \neq j} F_{H_i}^g(x_i, \mu) \left[F_{H_j}^c(x_j, \mu) - F_{H_j}^g(x_j, \mu) \otimes F_g^c(x_j, \mu) \right] \otimes \hat{\sigma}_{gc \rightarrow \Xi_{cc}}(x_1, x_2, \mu) \\
 &+ \sum_{i,j=1,2; i \neq j} \left[\left(F_{H_i}^c(x_i, \mu) - F_{H_i}^g(x_i, \mu) \otimes F_g^c(x_i, \mu) \right) \left(F_{H_j}^c(x_j, \mu) - F_{H_j}^g(x_j, \mu) \otimes F_g^c(x_j, \mu) \right) \right] \\
 &\quad \otimes \hat{\sigma}_{cc \rightarrow \Xi_{cc}}(x_1, x_2, \mu), \tag{1-13}
 \end{aligned}$$

where high order contributions are not included, $F_H^i(x, \mu, m_c)$ (with $H = H_1$ or H_2 ; $x = x_1$ or x_2) is the distribution function of parton i in hadron H , $\hat{\sigma}$ is the cross-section of the corresponding subprocess, μ is the renormalization or factorizing scale.^② The subtraction for $F_H^c(x, \mu)$ is defined as

$$F_H^c(x, \mu)_{SUB} = F_H^g(x, \mu) \otimes F_g^c(x, \mu) = \int_x^1 F_g^c(\kappa, \mu) F_H^g\left(\frac{x}{\kappa}, \mu\right) \frac{d\kappa}{\kappa}. \tag{1-14}$$

The second step is the fusion of the two c quarks into a (cc) -diquark, which could be either in $(cc)_{\bar{3}}[{}^3S_1]$ or $(cc)_6[{}^1S_0]$ configurations. As a summary, the hadronic production of Ξ_{cc} has contributions from

- LO: $g + g \rightarrow (cc)_{\bar{3}}[{}^3S_1]\bar{c}\bar{c}$, $g + g \rightarrow (cc)_6[{}^1S_0]\bar{c}\bar{c}$,
- LO: $g + c \rightarrow (cc)_{\bar{3}}[{}^3S_1]\bar{c}\bar{c}$, $g + c \rightarrow (cc)_6[{}^1S_0]\bar{c}\bar{c}$,
- NLO: $c + c \rightarrow (cc)_{\bar{3}}[{}^3S_1]\bar{c}\bar{c}$, $c + c \rightarrow (cc)_6[{}^1S_0]\bar{c}\bar{c}$,^③

as shown in Figure 1.3, 1.4, and 1.5. The formation of the (cc) -diquark is a non-perturbative process but can be described by a matrix element in the non-relativistic QCD

① Some references^[54,56] do not consider the contribution from extrinsic charm contribution in proton. There are also reference considering the intrinsic charm contribution, but the difference is small.
 ② For convenience, the renormalization scale μ_R for the subprocess and the factorization scale μ_F for factorizing the PDFs and the hard subprocess are taken to be the same, *i.e.* $\mu_R = \mu_F = \mu$.
 ③ The LO extrinsic charm fusion mechanisms only contribute to the purely longitudinal production, *i.e.* $p_T = 0$ ^[58], hence only the NLO mechanisms are considered.

(NRQCD) framework^[58,59]. The relevant matrix elements can be defined as

$$\begin{aligned} (cc)_6[{}^1S_0] : h_1 &= \frac{1}{48} \langle 0 | [\psi^{a_1} \epsilon \psi^{a_2} + \psi^{a_2} \epsilon \psi^{a_1}] (a^\dagger a) \psi^{a_2 \dagger} \epsilon \psi^{a_1 \dagger} | 0 \rangle, \\ (cc)_3[{}^3S_1] : h_3 &= \frac{1}{72} \langle 0 | [\psi^{a_1} \epsilon \sigma^i \psi^{a_2} - \psi^{a_2} \epsilon \sigma^i \psi^{a_1}] (a^\dagger a) \psi^{a_2 \dagger} \sigma^i \epsilon \psi^{a_1 \dagger} | 0 \rangle, \end{aligned} \quad (1-15)$$

where $a_j (j = 1, 2, 3)$ is the color of the valence quark fields and $\sigma^i (i = 1, 2, 3)$ are Pauli matrices, $\epsilon = i\sigma^2$. h_1 and h_3 represent the probability that the two c quarks merge into a diquark with $(cc)_6[{}^1S_0]$ and $(cc)_3[{}^3S_1]$, respectively.

The third step is the hadronization of the diquark. It can be assumed that diquark is bound tightly enough to have a probability near one to fragment to a doubly charmed baryon^[56,60]. Therefore the calculation of the production cross-section for doubly charmed baryons is equivalent to the production of (cc) -diquark. Combining Eq. 1-13, 1-14, and 1-15, the production cross-section can be calculate numerically, and the results without taken charge conjugation into account are listed in Table 1.3.

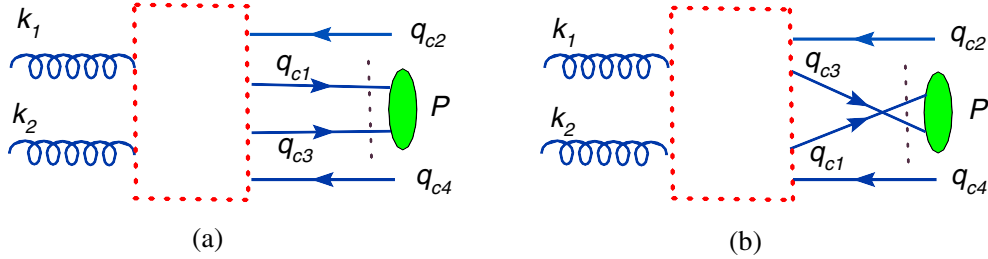


图 1.3 The schematic Feynman diagrams of the gluon-gluon mechanism for the hadronic production of Ξ_{cc} ^[58].

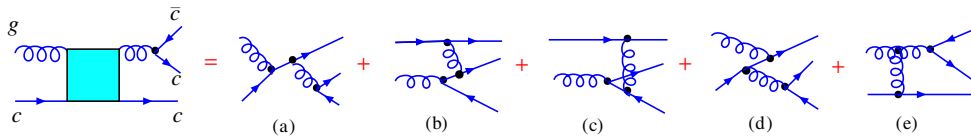


图 1.4 The typical Feynman diagrams for the gluon-charm scattering mechanism for the hadronic production of Ξ_{cc} ^[58].

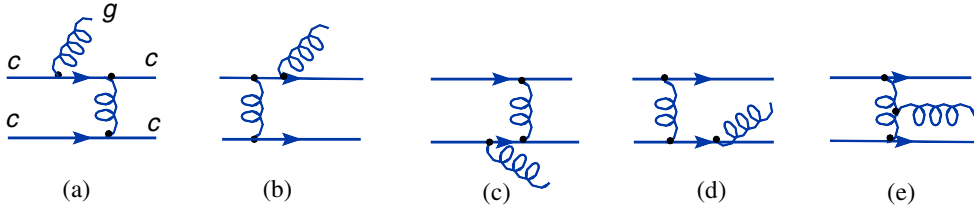


图 1.5 The typical Feynman diagrams for the charm-charm mechanism for the hadronic production of Ξ_{cc} [58].

表 1.3 Ξ_{cc} production cross-section at the LHC

Reference	Ξ_{cc} production cross-section[nb]	Fiducial Cut	Comment
[57]	1800	Not mentioned	
[54]	122	$ y < 1$	Not consider $(cc)_6[{}^1S_0]$ contribution
[58]	63	$ y < 1.5, p_T > 4 \text{ GeV}$	
[61]	59	$1.8 \leq \eta \leq 5.0, p_T > 4 \text{ GeV}$	LHCb acceptance $1.8 \leq \eta \leq 5.0$

The theoretical calculation above predicts the production of doubly charmed baryons inclusively, not for Ξ_{cc}^+ only. The probability that a (cc) diquark fragments into a Ξ_{cc}^+ baryon is assumed to be 40%, according to the measured cross-section of charmed mesons [62]. Therefore, the production cross-section for Ξ_{cc}^+ is

$$\sigma(pp \rightarrow \Xi_{cc}^{\pm} X) = 2 \times (63 + 59) \times 0.4 \approx 100 \text{ nb} \quad (1-16)$$

1.3.6 Decay modes of Ξ_{cc}^+

The Ξ_{cc}^+ baryon is one of the ground states of doubly charmed baryons, therefore it is expected to decay weakly. Enlightened speculations can be made from theory for the decays. Concerning the reconstruction and selection at LHCb detector, these decays should not contain neutral particles in the final states, and should contain a daughter with a long enough lifetime to be separated from prompt background. Some of the possible decays are listed below.

- $\Xi_{cc}^+ \rightarrow \Lambda_c^+ K^- \pi^+$
- $\Xi_{cc}^+ \rightarrow D^0 p K^- \pi^+$
- $\Xi_{cc}^+ \rightarrow D^+ p K^-$

- $\Xi_{cc}^+ \rightarrow \Xi_c^+ \pi^+ \pi^-$
- $\Xi_{cc}^+ \rightarrow \Xi_c^0 \pi^+$

We will focus on the $\Xi_{cc}^+ \rightarrow \Lambda_c^+ K^- \pi^+$ decay in this thesis. When the number of the BF is needed for estimation, 5% will be used, which is simply the BF of $\Lambda_c^+ \rightarrow p K^- \pi^+$ in the PDG^[48]. This may not be an accurate estimate, but it is expected to be the same order of the true value, since the Feynman diagrams of these decays are very similar.

1.4 Experimental status

Many experiments have searched for the doubly charmed baryons, but the experimental knowledge are not quite clear now. The SELEX collaboration reported the signal of doubly charmed baryons, but following searched didn't confirm their results.

1.4.1 The SELEX results

SELEX is a fixed target experiment employing beams of Σ^- , π^- , and protons at around 600 GeV/ c to study the properties of charmed baryons^[63].

In 2002 the SELEX collaboration announced the observation of the Ξ_{cc}^+ baryon with a significance of 6.3σ in the combination of $\Lambda_c^+ K^- \pi^+$ ^[64], whose mass spectrum distribution is shown in 1.6. The p-value of the peak increases from 1.0×10^{-6} to 1.1×10^{-4} (3.9σ) when taking the look-elsewhere effect^[65] into account^[48].

In 2003 a state with the same invariant mass as $\Xi_{cc}^+(3520)$ was reported in the pD^+K^- final state^[66], whose mass spectrum distribution is shown in 1.7.

In 2006 another state with the same invariant mass was reported in the $\Xi_c^+ \pi^+ \pi^-$ final state^[67], whose mass spectrum is shown in Figure 1.8.

Apart from this $\Xi_{cc}^+(3520)$ state, SELEX also observed one excited doubly charmed baryon $\Xi_{cc}^{++}(3780)$, one $\Xi_{cc}^{++}(3460)$, and one $\Xi_{cc}^{++}(3541)$ in the $\Lambda_c^+ K^- \pi^+ \pi^+$ final state; one $\Xi_{cc}^+(3443)$ in the $\Lambda_c^+ K^- \pi^+$ final state^[68][Ⓐ]. The mass spectrum of these final states can be found in Figure 1.9.

There were several anomalies in the SELEX observation. While the measured mass, $3518.7 \pm 1.7 \text{ MeV}/c^2$, agreed with theoretical predictions, the lifetime they measured was consistent with zero, which was incompatible with theoretical calculations. The SELEX observation also implied a production cross-section of Ξ_{cc}^+ much higher than

Ⓐ Recently they also reported a $\Xi_{cc}^{++}(3452)$ in $\Lambda_c^+ K^- \pi^+ \pi^+$ and $\Xi_c^+ \pi^- \pi^+$ final states^[69].

expected. While the theory calculates the Ξ_{cc}^+ production to total charm production to be $\sigma_{\Xi_{cc}^+}/\sigma_{\text{charm}} \sim 10^{-6} - 10^{-5}$ at SELEX^[41], the ratio at SELEX was estimated to be 2.1×10^{-2} .

1.4.2 The FOCUS results

The FOCUS collaboration is a heavy-flavour photoproduction experiment with a centre-of-mass energy of 200 GeV. They searched for Ξ_{cc}^+ and Ξ_{cc}^{++} baryons in various final states, but didn't find significant evidence for either of them, as shown in Figure 1.10. If only the two decay modes searched for by SELEX are used, then no event is observed in the SELEX signal region, as shown in Figure 1.12. Note FOCUS failed to observe Ξ_{cc}^+ from 19400 constructed Λ_c^+ , compared to 15.8 Ξ_{cc}^+ events from 1650 Λ_c^+ at SELEX. If we assume both of the two experiments are reliable, then the presence probability of one $(g, c\bar{c})$ vertex at SELEX must be an order of magnitude higher than that of FOCUS.^[70], which implies SELEX should observe at least one thousand Ω_c baryons, given that FOCUS observed 111.5 Ω_c events. However, the total sample of SELEX only contains 107 ± 22 Ω_c events^[67].

1.4.3 The Belle results

Belle is an asymmetric-energy e^+e^- experiment optimised for b physics. They reported the search for doubly charmed baryons Ξ_{cc}^+ with 461.5 fb^{-1} data sample using $\Lambda_c^+ K^- \pi^+$ final states in 2006, but failed to observe any significant signal^[71], as shown in Figure 1.13. Recently they had an update on the doubly charmed baryons search with a data sample of 980 fb^{-1} ^[72], where they included the decay $\Xi_{cc}^+ \rightarrow \Xi_c^0 \pi^+$ and also searched for the Ξ_{cc}^{++} baryon. Figure 1.14 shows the invariant mass distribution of the Ξ_{cc}^+ and Ξ_{cc}^{++} candidates using $\Lambda_c^+ K^- \pi^+(\pi^+)$ final states. Figure 1.15 and Figure 1.16 show the mass spectrum of Ξ_{cc}^+ and Ξ_{cc}^{++} candidates using $\Xi_c^0 \pi^+(\pi^+)$, respectively. No significant Ξ_{cc} signal observed in these final states.

1.4.4 The BaBar results

BaBar is an asymmetric-energy e^+e^- experiment optimised for b physics at SLAC. They searched for the Ξ_{cc}^+ baryon in the final states $\Lambda_c^+ K^- \pi^+$ and $\Xi_c^0 \pi^+$, and the Ξ_{cc}^{++} baryon in the final states $\Lambda_c^+ K^- \pi^+ \pi^+$ and $\Xi_c^0 \pi^+ \pi^+$. The distributions of the mass difference $\Delta M(\Xi_{cc} - \Lambda_c^+)$ and $\Delta M(\Xi_{cc} - \Xi_c^0)$ are shown in Figure 1.17.

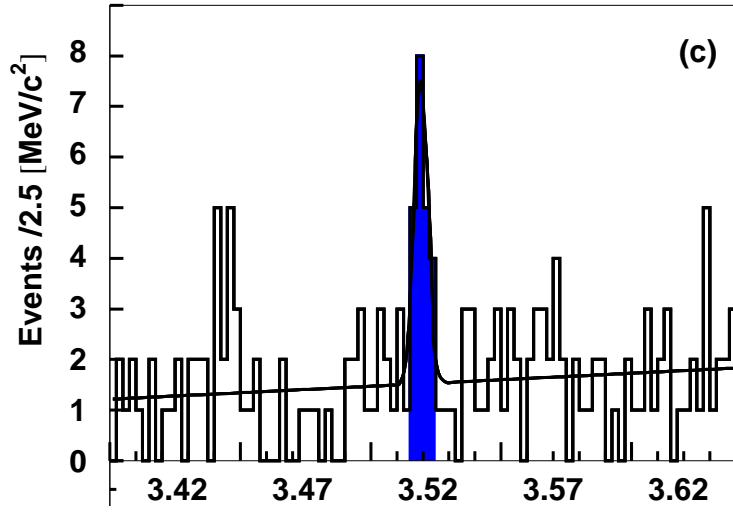


图 1.6 The $\Lambda_c^+ K^- \pi^+$ mass distribution shown in $2.5 \text{ MeV}/c^2$ bins. The fit function is a Gaussian signal plus a linear background.

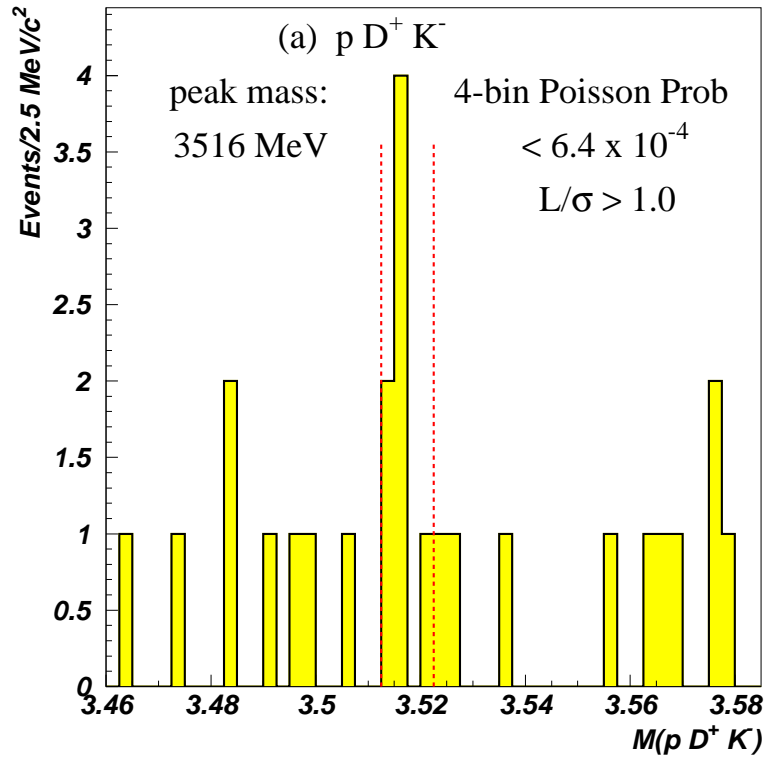


图 1.7 The $p D^+ K^-$ mass distribution shown in $2.5 \text{ MeV}/c^2$ bins. The fit function is a Gaussian signal plus a linear background.

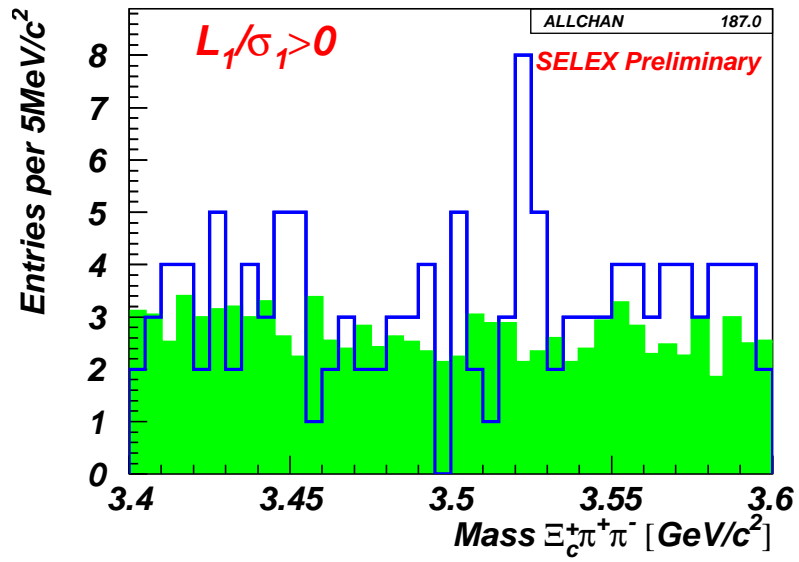


图 1.8 The $\Xi_c^+ \pi^+ \pi^-$ mass distribution shown in 5 MeV/c^2 bins. The green histogram is the estimate of the combinatoric background.

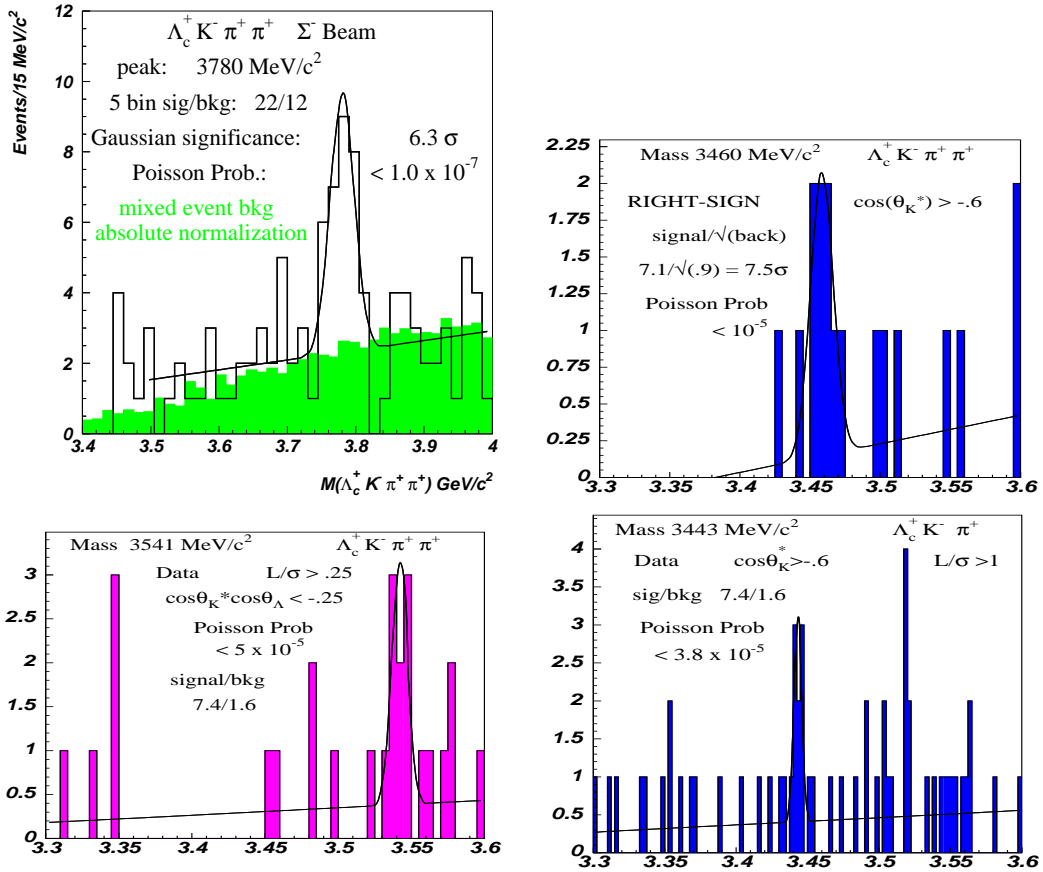


图 1.9 Other states reported by the SELEX collaboration. Top left for the observation of $\Xi_{cc}^{++}(3780)$, top right for $\Xi_{cc}^{++}(3460)$, bottom left for $\Xi_{cc}^{++}(3541)$, and bottom right for $\Xi_{cc}^{++}(3443)$.

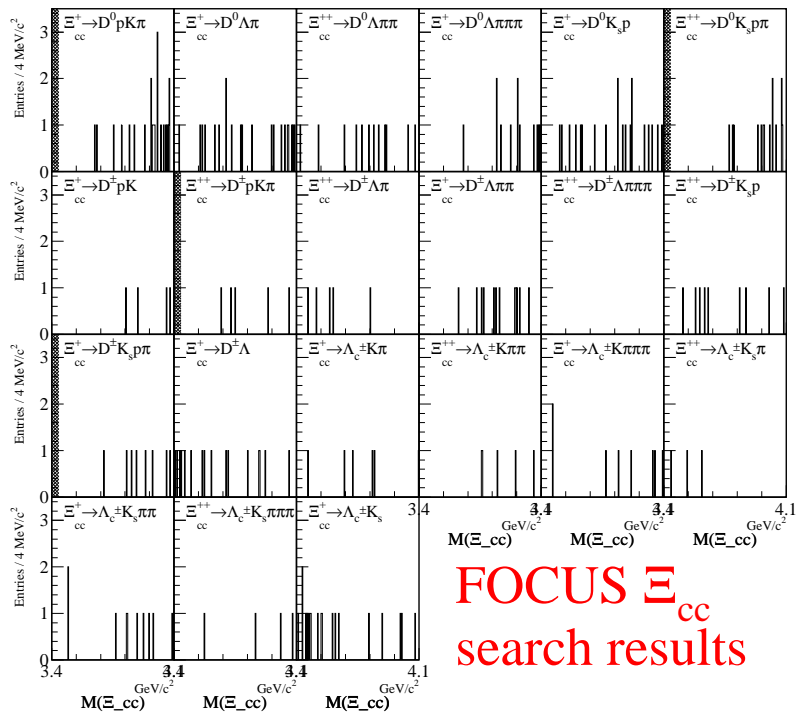


图 1.10 The mass spectrum of doubly charmed baryon candidates in various decay modes.

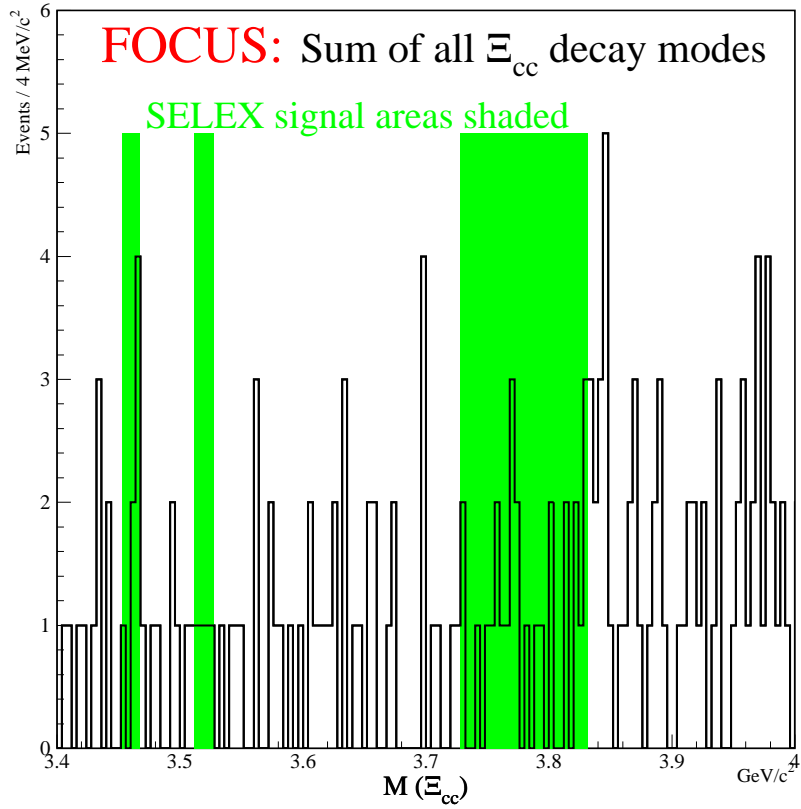


图 1.11 The mass spectrum of all the charmed baryon candidates. The three shaded regions correspond to three states reported by SELEX, $\Xi_{cc}^{++}(3460)$, $\Xi_{cc}^+(3520)$, and $\Xi_{cc}^{++}(3780)$.

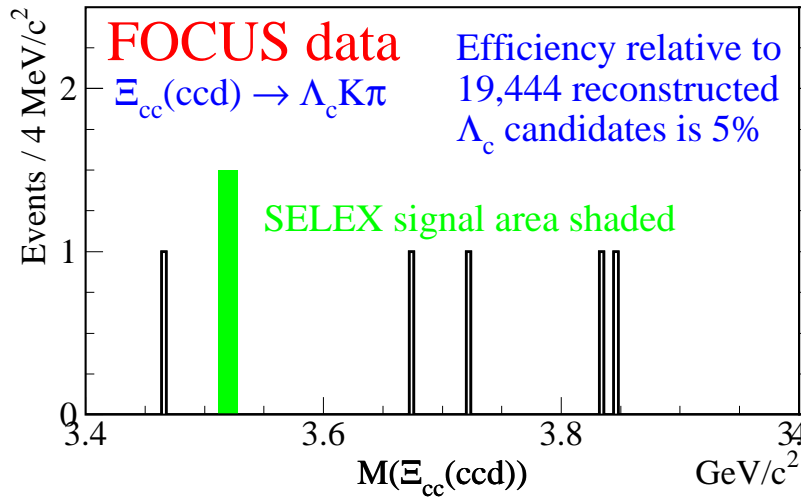


图 1.12 The invariant mass distribution of the Ξ_{cc}^+ candidates (left) and the Ξ_{cc}^{++} candidates (right) for FOCUS. The shaded region in the left plot correspond to the state $\Xi_{cc}^+(3520)$, and the regions in the right plot correspond to the state $\Xi_{cc}^{++}(3460)$ and $\Xi_{cc}^{++}(3780)$.

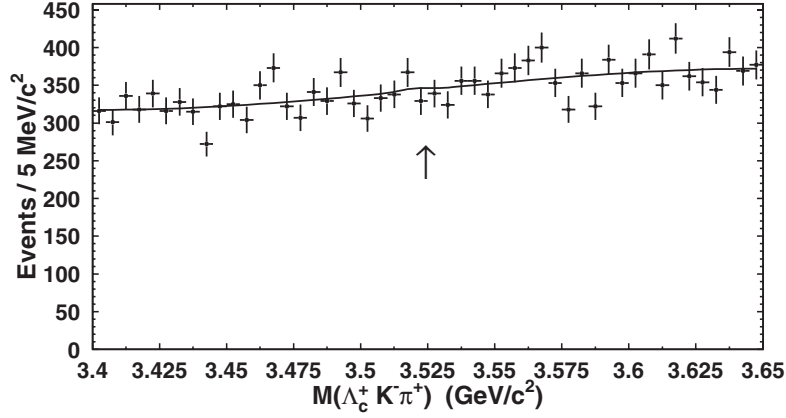


图 1.13 The invariant mass distribution of $\Lambda_c^+ K^- \pi^+$. The mass of the SELEX candidate is indicated by an arrow.

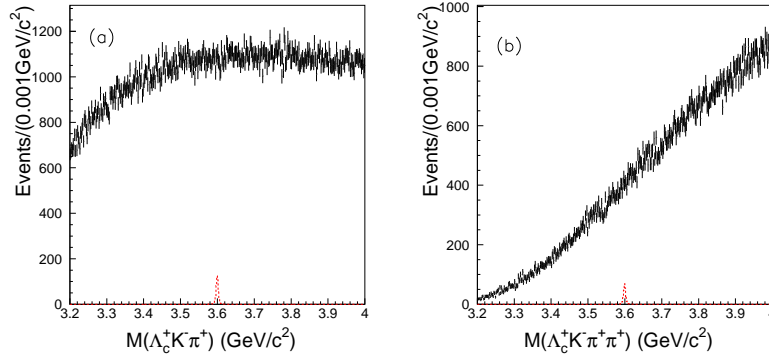


图 1.14 The invariant mass distribution of the Ξ_{cc} candidates for $\Lambda_c^+ K^- \pi^+$ (left) and $\Lambda_c^+ K^- \pi^+ \pi^+$ (right) final state. The dashed histograms are signal MC assuming $\sigma(e^+ e^- \rightarrow \Xi_{cc}^{+(+)}) = 500 \text{ fb}^{-1}$ and $\mathcal{B}(\Xi_{cc}^{+(+)} \rightarrow \Lambda_c^+ K^- \pi^+ (\pi^+)) = 5\%$.

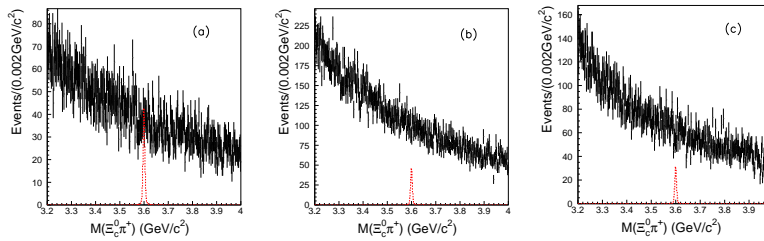


图 1.15 The invariant mass distribution of the Ξ_{cc}^+ candidates for $\Xi_{cc}^0 \pi^+$ final state with Ξ_{cc}^0 reconstructed from $\Xi^- \pi^+$, $\Lambda K^- \pi^+$, and $p K^- K^- \pi^+$. The dashed histograms are signal MC assuming $\sigma(e^+ e^- \rightarrow \Xi_{cc}^+) = 500 \text{ fb}^{-1}$, $\mathcal{B}(\Xi_{cc}^+ \rightarrow \Xi_{cc}^0 \pi^+ (\pi^+)) = 5\%$ and $\mathcal{B}(\Xi_{cc}^0 \rightarrow \Xi^- \pi^+) = 5\%$.

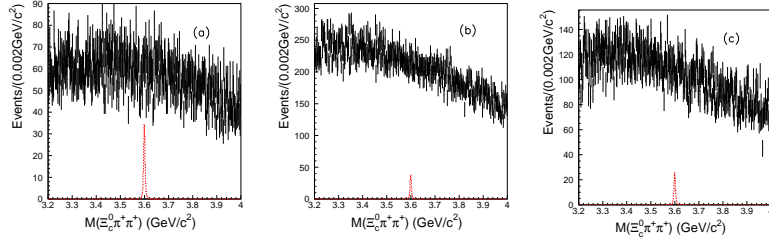


图 1.16 The invariant mass distribution of the Ξ_{cc}^{++} candidates for $\Xi_c^0\pi^+$ final state with Ξ_c^0 reconstructed from $\Xi^-\pi^+$, $\Lambda K^-\pi^+$, and $pK^-K^-\pi^+$. The dashed histograms are signal MC assuming $\sigma(e^+e^- \rightarrow \Xi_{cc}^{++}) = 500 \text{ fb}^{-1}$, $\mathcal{B}(\Xi_{cc}^{++} \rightarrow \Xi_c^0\pi^+(\pi^+)) = 5\%$ and $\mathcal{B}(\Xi_c^0 \rightarrow \Xi^-\pi^+) = 5\%$.

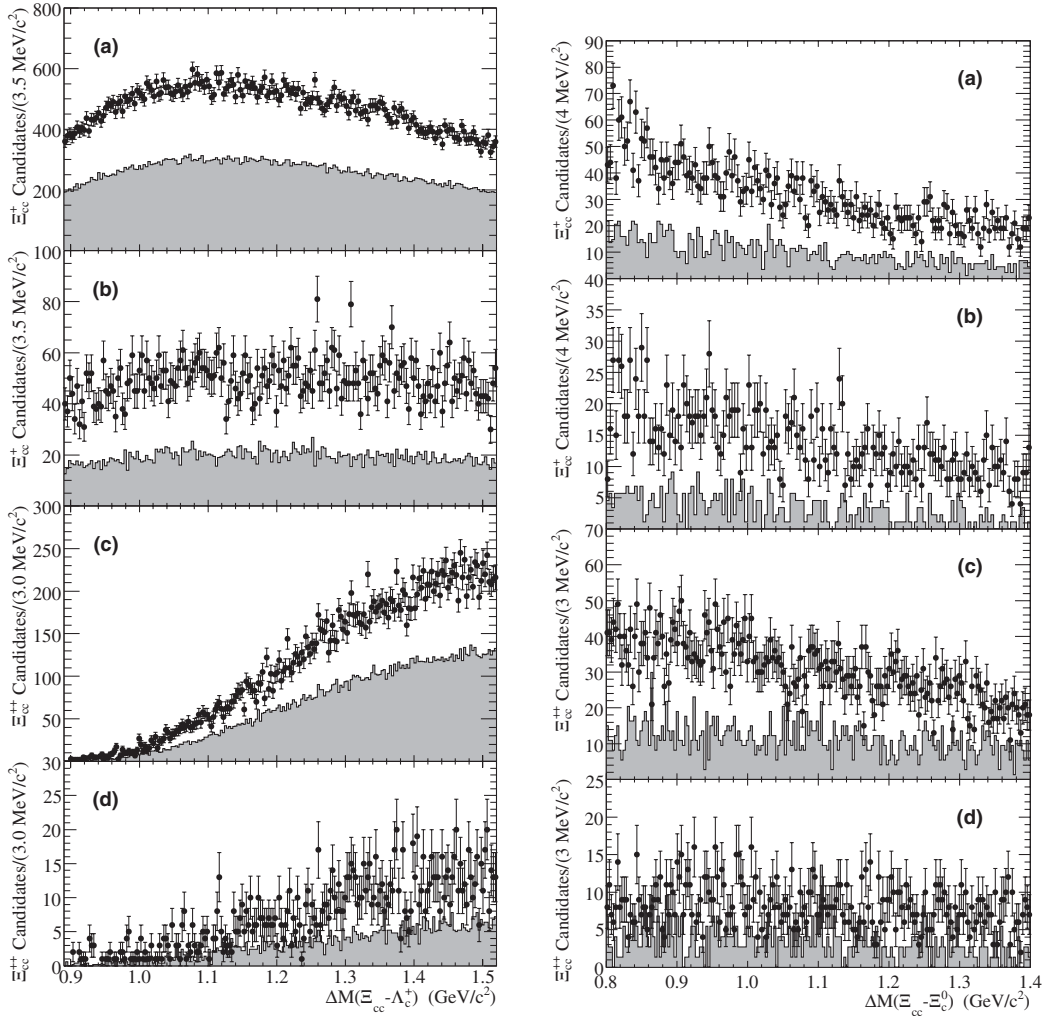


图 1.17 The distributions of the mass difference $\Delta M(\Xi_{cc} - \Lambda_c^+)$ (left) and $\Delta M(\Xi_{cc} - \Xi_c^0)$ (right) for (a,b) Ξ_{cc}^+ and (c,d) Ξ_{cc}^{++} candidates with (a,c) no p^* requirements and (b,d) $p^* > 2.3 \text{ GeV}/c$ ($2.0 \text{ GeV}/c$ for right plot), where p^* is the momentum of Ξ_{cc} candidates in the centre-of-mass system. Shaded histograms correspond to candidates in the sideband region of Λ_c^+ .

第 2 章 The LHCb Experiment

2.1 The Large Hadron Collider at CERN

The Large Hadron Collider (LHC)^[73], is a two-ring superconducting proton-proton collider, located in a 26.7 km long tunnel at CERN, Geneva. The LHC is designed to be a multi-TeV machine since there is a no-lose theorem which ensures that the LHC is certain to discover something at this energy scale^[74]. First, although the SM is extremely successful, one of the most important piece of this model, the Higgs boson, was still missing (at 1980s). The mass of the Higgs boson can not be calculated from the SM directly, but it could be constrained by the precision measurements of the weak interaction^[75]. The global fit shows the Higgs boson should have a mass smaller than 250 GeV^[76]. Second, there are aesthetic arguments and cosmological evidences which indicate there must be physics beyond the SM. Supersymmetry is by far the most intensely studied class of theories as a possible candidate of new physics. The naturalness of supersymmetry implies that new physics must appear at the 1 TeV energy^[77]. With the ability to access physics at TeV scale, the LHC can either discover the Higgs boson, or find new physics beyond the SM, or even both.

In the planned running conditions, LHC has two 7 TeV counter-rotating proton beams containing 2808 bunches separated by 25 ns intervals, with 1.15×10^{11} protons in each bunch. Before the proton beams enter the LHC, they need to be accelerated to a certain energy, which is accomplished by other accelerators. The layout of the whole beam acceleration chain is shown in Fig. 2.1???. Before the acceleration begins, protons are produced from a hydrogen duoplasmatron source, which strips electrons from the hydrogen atoms^[78,79]. They are then fed into the Linear accelerator 2 (Linac 2)^[80,81], which accelerates the protons to the energy of 50 MeV/ c^2 , and inject the beam to the Proton-Synchrotron-Booster (PSB), where protons are further accelerated to 1.4 GeV in one of the PSB's four rings and delivered to the Proton-Synchrotron (PS), which pushes protons to 25 GeV and divides them to form the nominal LHC 25 ns bunch train. After transferred to the Super-Proton-Synchrotron (SPS), where protons are further accelerated to 450 GeV, the beam finally enters the LHC ring, which accelerates protons to the desired

energy.

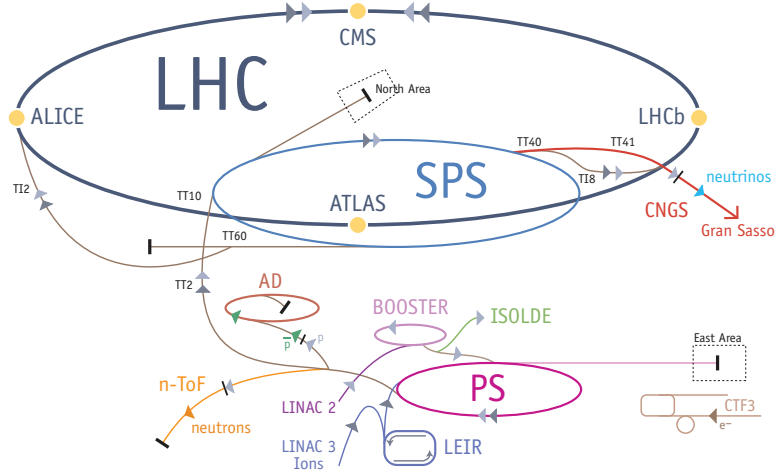


图 2.1 The layout of the LHC accelerator complex.

To manipulate beams at an energy of multi-TeV, a bending magnetic field close to the limit of current technologies, 8.33 T, is required. This strong magnetic field is achieved by cooling 1232 magnets with super-fluid Helium to an operating temperature of 1.9 K.

Four main detectors are installed along the LHC ring for different physics purposes. The two general purpose detectors, the ATLAS^[82] and CMS^[83] experiment, aim to discover the Higgs boson and search for new physics directly. The LHCb^[84] experiment is optimized for precision measurements of CP violation parameters and rare decays of hadrons containing *b* and *c* hadrons. The ALICE^[85] experiment is the dedicated heavy-ion physics program at the LHC.

In November 2009, LHC circulated two proton beams simultaneously at the first time. On March 30, 2010, LHC successfully collided two proton beams at the energy of 7 TeV. In 2010 and 2011, LHC took data at a centre of mass energy of 7 TeV. In 2012, the centre-of-mass energy raised to 8 TeV. Figure 2.2 shows the delivered integrated luminosity for each detector in each year.

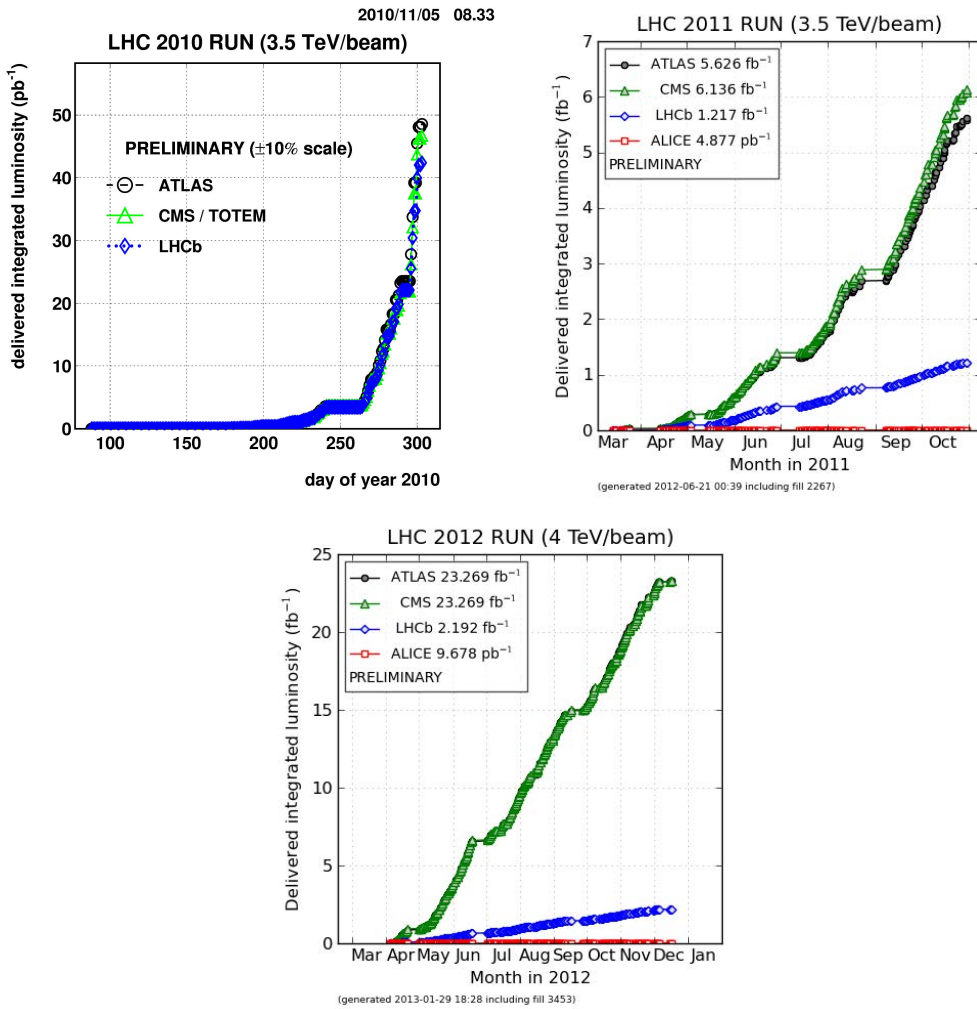


图 2.2 The delivered integrated luminosity for each detector in (top left) 2010, (top right) 2011 and (bottom) 2012, respectively. LHC delivered 50 pb^{-1} , 6 fb^{-1} and 25 fb^{-1} for ATLAS and CMS, and 40 pb^{-1} , 1.2 fb^{-1} and 2.2 fb^{-1} for LHCb in 2010, 2011 and 2012, respectively.

2.2 The LHCb detector

The LHCb is an experiment designed to precisely test the SM and to search for indirect evidence of new physics at loop level in CP violation and rare decays of beauty and charm hadrons. The SM has been tested at a very high precision and works very well to explain all the experimental data. However, there is only one source of CP violation in the SM, i.e. the CKM mechanism^[18]. This is not enough to explain the amount of matter in the universe. A new source of CP violation must exist. Many new physics models produce additional contribution of CP violation and generate decay modes which is forbidden or highly suppressed in the SM. A precision measurement of the SM

parameters could potentially uncover new physics beyond the SM. Heavy flavour physics, especially b physics, is theoretical cleaner in the SM, hence an ideal place to proceed new physics tests. LHCb measures the total $b\bar{b}$ cross section at $\sqrt{s} = 7$ TeV to be $288 \pm 4(\text{stat.}) \pm 48(\text{syst.}) \text{ mb}^{[86]}$, and the total $c\bar{c}$ at $\sqrt{s} = 7$ TeV to be $1419 \pm 12(\text{stat.}) \pm 116(\text{syst.}) \pm 65(\text{frag}) \text{ mb}^{[62]}$. With this unprecedented large samples of charm and beauty hadrons, LHCb can impose a very stringent test on the SM.

The dominated production mechanism for $b\bar{b}$ pairs at the LHC is the gluon-gluon fusion, which results in highly correlated kinematics between the $b\bar{b}$ pairs and a violent boost along the beam axis for the particles produced, as is shown in Figure 2.3. The LHCb detector is then designed to be a single arm spectrometer, with a forward angular acceptance of 10 mrad to 300 mrad in the bending plane and 10 mrad to 250 mrad in the non-bending plane. Covering only 4% of the 4π solid angle, LHCb collects 27% of b or \bar{b} hadrons. LHCb is located at the LHC interaction point 8. The positive z -axis of the LHCb coordinate system is adopted to coincide with the direction of LHC beam 1 (clock-wise beam), and the positive y -axis points upwards from the ground.

The nominal LHC luminosity is of order $10^{34} \text{ cm}^{-2}\text{s}^{-1}$, which could cause a detector occupancy much higher than the LHCb can accept. Also, the high luminosity leads to multiple proton-proton interactions in one collision. As a result, the b -tagging and lifetime analysis will be difficult due to the ambiguities in the primary vertices determination. Therefore, the luminosity at LHCb is decreased to $2 \times 10^{32} \text{ cm}^{-2}\text{s}^{-1}$. This is achieved by a local de-focussing of the LHC beams at the LHCb interaction point. Running at a lower luminosity also reduces the radiation damage to the detector.

A precise tracking system and an efficient Particle IDentification (PID) system are essential to perform precise measurements of heavy flavour physics. At LHCb the tracking system is composed of the vertex locator(VELO), the trigger tracker (TT), the inner tracker (IT), the outer tracker (OT) and the dipole magnet. The PID system consists of two Ring-Imaging Cherenkov detectors (RICH1 and RICH2), the electromagnetic calorimeter (ECAL), the hadron calorimeter (HCAL) and muon detectors. The layout of the LHCb detector is shown in Figure ???. The detailed descriptions of the various subdetectors will be given in the following sections.

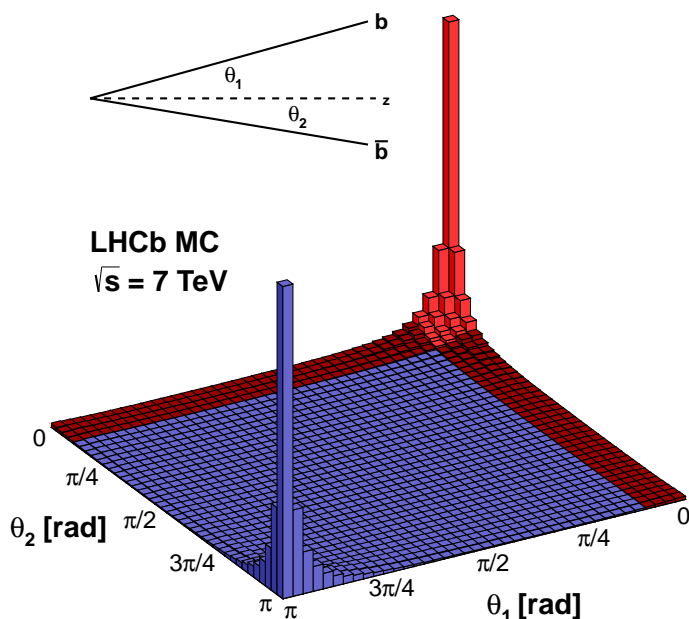


图 2.3 Simulated distribution of polar angles of b or \bar{b} hadrons with respect to the beam axis.

2.2.1 The tracking system

The tracking system serves to reconstruct charged particles and to measure their momentum. Tracks are reconstructed across the spectrometer by combining hits in VELO with that in the main trackers. After the reconstruction, tracks are extrapolated to the VELO region to perform the vertex fit^[87].

2.2.1.1 The VELO

The VELO is a silicon detector that provides precise measurements of tracks close to the interaction region. These tracks are used to determine the secondary vertices, which are signatures of heavy flavour decays.

The VELO consists of 21 tracking stations, each divided to two retractable modules sensors from the beam (see below), as shown in Figure 2.4. To improve the resolution of the primary vertex (PV), some of the stations are installed upstream of the nominal interaction point. The pile-up veto system, the two additional stations located upstream of the VELO, are used for the luminosity measurement (see 2.3). The modules are designed to be a semi-circular plate rather than a simpler rectilinear scheme to use cylindrical geome-

try ($R\phi$ coordinates), which improves the performance of track and vertex reconstruction at LHCb trigger. To achieve a better resolution of the impact parameters, the inner radius of the module should be as close to the beam axis as possible for a shorter track extrapolation length. However, due to yet-unknown closed-orbit variation of the LHC, the allowed closest approach to the beam axis is 5 mm ^[84], with the sensitive area begins at a distance of $\sim 8\text{ mm}$. During beam injection and acceleration, the increased size of the beam spot requires two halves of the VELO retracted by a distance of 3 cm . When closed, the two modules of each station are required to overlap to cover the full azimuthal acceptance and to improve alignment. The outer radius of the module is designed to be 42 mm . Each module contains two different kinds of silicon sensor on two sides, one to measure radial coordinate (R -sensor) and one to measure azimuthal angles (ϕ -sensor). Each sensor, R -type or ϕ -type, has 2048 readout channels. To minimize occupancy and reduce strip capacitance, the R -sensors are divided into four regions, each with 512 concentric strips. The strip pitch varies linearly from the inner edge ($38\text{ }\mu\text{m}$) to the outer edge ($102\text{ }\mu\text{m}$) to keep the strip occupancy approximately constant across the region and to ensure that measurements along a track contribute equally to the impact parameter precision. The ϕ -sensors are divided radially into two sections to reduce occupancy and to limit the strip pitch at the outer edge. The inner section has 683 strips with an angle of 20° to the radial direction and the pitch increasing linearly from the inner radius ($38\text{ }\mu\text{m}$) to the boundary, while the outer section has 1365 strips with an angle of -10° to the radial direction and the pitch increasing linearly from the boundary ($39\text{ }\mu\text{m}$) to the outer radius. In order to provide a stereo effect the ϕ -sensors in adjacent modules have opposite skews with respect to each other.

The VELO has an excellent performance during the data-taking period. Figure 2.6 shows the VELO reconstructed PV resolution in 2010 data as a function of the number of tracks used to reconstruct the vertex. It can be found that for a vertex reconstructed by 25 tracks, a resolution of $14\text{ }\mu\text{m}$ in x and $75\text{ }\mu\text{m}$ in z can be achieved. For early 2011 data, the resolution is almost the same, as shown in Figure 2.7. Figure 2.8 shows the impact parameter resolution for the early 2011 data and the simulated sample as a function of the inverse of the transverse momentum (p_T). Due to the imperfect Monte Carlo modeling, e.g. the multiple scattering and the material description is not inaccurate, some discrepancies are observed between data and simulated sample. The VELO meets the requirements of tracking and vertexing at LHCb, and has key contributions to the

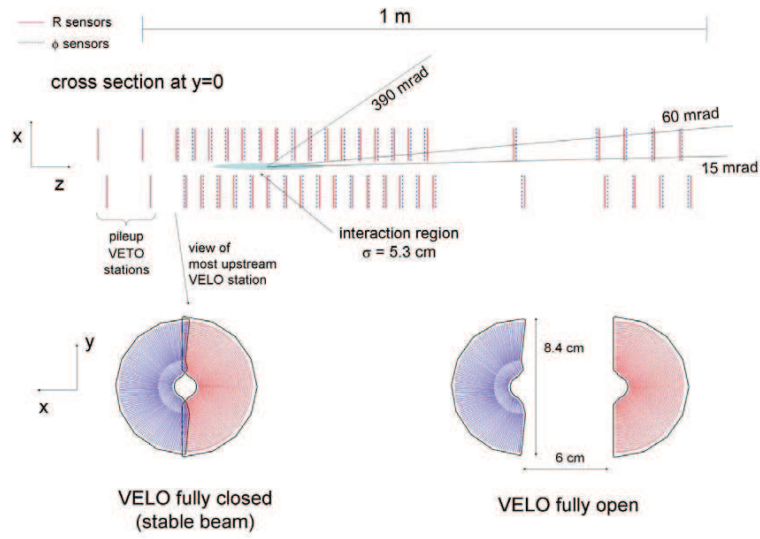


图 2.4 The top plot shows the cross section of the VELO in the $x - z$ plane at $y = 0$, with the subdetector in the fully closed position. The VELO consists of 21 tracking stations, each divided to two retractable modules. The two pile-up stations located at upstream of the VELO are also shown. The bottom plots show the front-face of the module in the (left) fully closed and (right) fully open position.

LHCb physics results.

2.2.1.2 The trigger tracker

The TT, located between the RICH1 detector and the dipole magnet, is a silicon microstrip detector with a strip pitch of about $200 \mu\text{m}$. The TT consists one stations with four rectangular detection layers, which is approximately 150 cm in width and 130 cm in height to cover the full LHCb acceptance. The layout of the third layer TT detection layer is shown in Figure 2.9. The four layers are settled in the sequence of $x - u - v - x$, with the strips in the x layers arranged vertically, while the strips in the u and v layers rotated $+5^\circ$ and -5° . The TT has an active area of about 8.4 m^2 with 143360 readout strips. To facilitate the tracking algorithm, the four layers are grouped into two pairs, (x, u) and (v, x) , which are partitioned about 27 cm along the beam axis. Each layer is divided to upper half and lower half, each comprised of a row of seven silicon sensors orgnized into two or three readout sectors depending on their position relative to the beam pipe. The orgnization of a half module close to the beam pipe is illustrated in Figure 2.10.

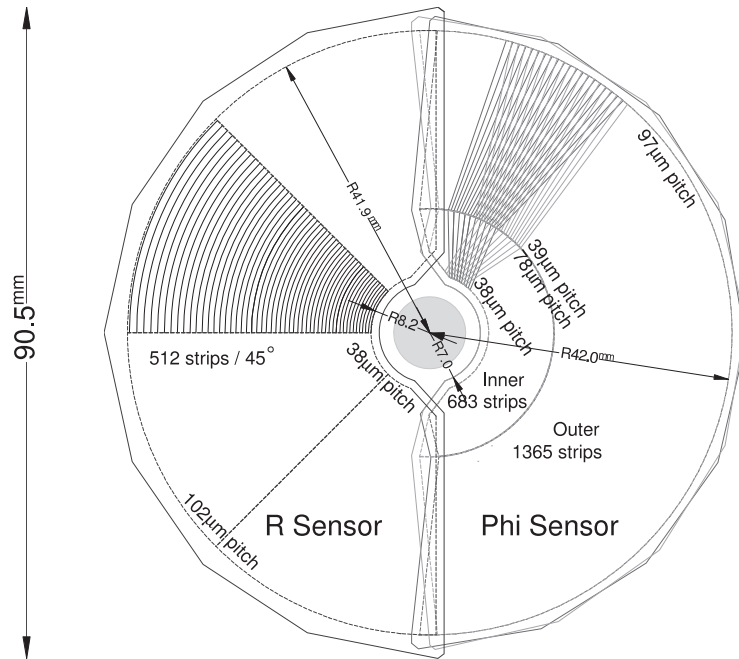


图 2.5 The VELO silicon sensors, with part of strips shown. For ϕ -sensors, strips on two adjacent modules are indicated.

2.2.1.3 The inner tracker

The tracking stations (T-stations) T1-T3 are divided into two regions: the Inner Tracker (IT) and the Outer Tracker (OT). Each station of the IT is a silicon microstrip subdetector consisting of four layers, with each covers 120 cm in width and 40 cm in height. The IT has an active area of 4.0 m² with 129024 readout strips. The same arrangement of the four layers as the TT is repeated in each station of IT. The layout of an x detection layer in the second IT station is shown in Figure 2.11. The IT only covers approximately 2% of the LHCb acceptance, but it is estimated that about 20% of tracks pass through it.

The OT covers the rest of the detector acceptance at the tracking stations T1-T3, up to 300 mrad in the horizontal plane and 250 mrad in the vertical plane. As the particle flux is much lower in the outer region, the OT is designed as a drift-time subdetector employing straw-tube technology, as shown in Figure 2.12. Each station of the OT contains four layers with the same pattern as for the TT and the IT. Each layer has several gas-tight straw-tube modules, with each containing two staggered layers of drift-tubes filled with a mixture gas of Argon (70%) and CO₂ (30%) for a fast drifting time (below 50 ns) and sufficient drift-coordinate resolution (200 μm). The cross-section of a straw-tube module

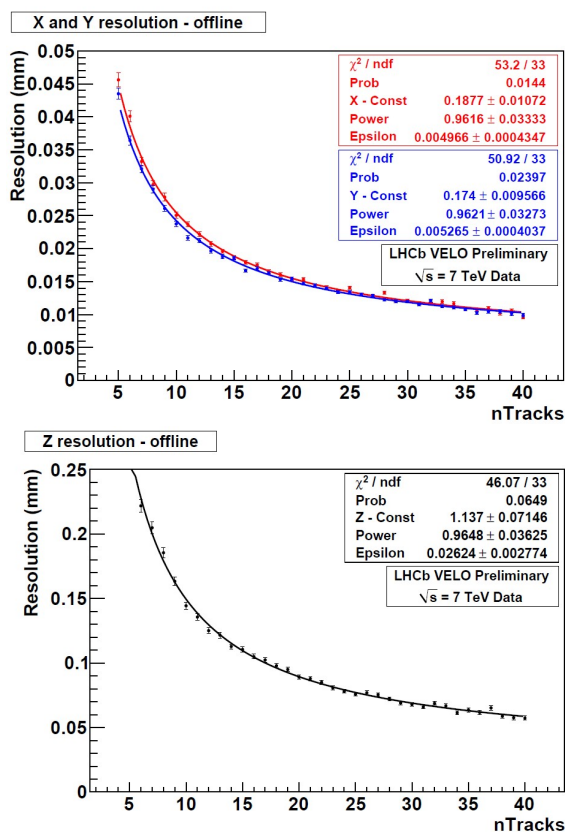


图 2.6 The resolution of VELO reconstructed PV in (left) x and y direction and (right) z direction. is displayed in Figure 2.13. The whole OT detector consists of 168 long and 96 short modules and contains about 55000 single straw-tube channels.

2.2.1.4 The magnet

A strong magnetic field is essential for high-precision momentum measurements. Originally the LHCb magnet was designed to be a super-conducting magnet, but later it was found that a super-conducting magnet requires an unacceptable investigation cost and takes a long time to construct and operate, which is a serious shortcoming at LHCb since the polarity of the magnetic field need to be regularly inverted to minimise the systematic uncertainty. Therefore, in LHCb the magnetic field is provided by a dipole magnet, located downstream of the TT and upstream of the tracking station T1. The magnet covers the full acceptance of ± 250 mrad vertically and of ± 300 mrad horizontally. To achieve the planned integrated magnetic field of 4 Tm for tracks of 10 m and to provide a field as strong as possible in the regions between the VELO and the TT while to suppress the field strength in RICH detectors, the magnet is subdivided into two identical coils

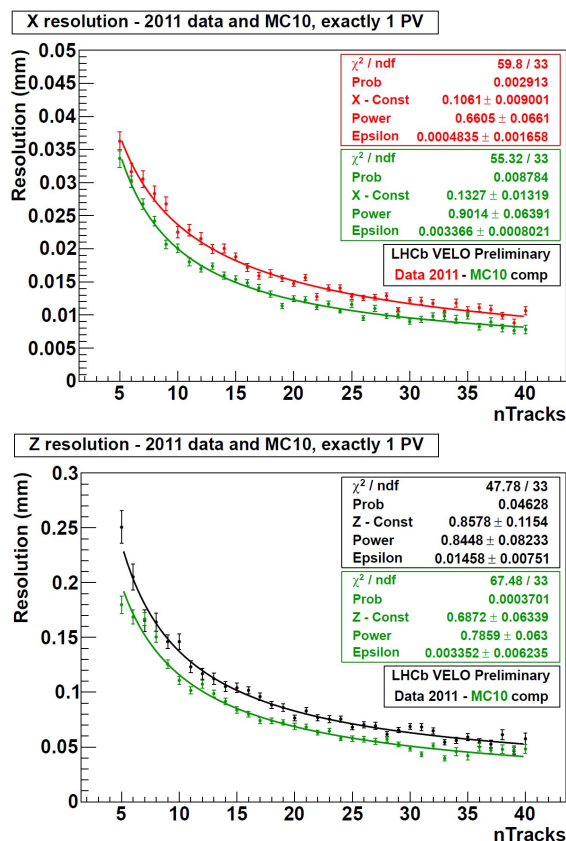


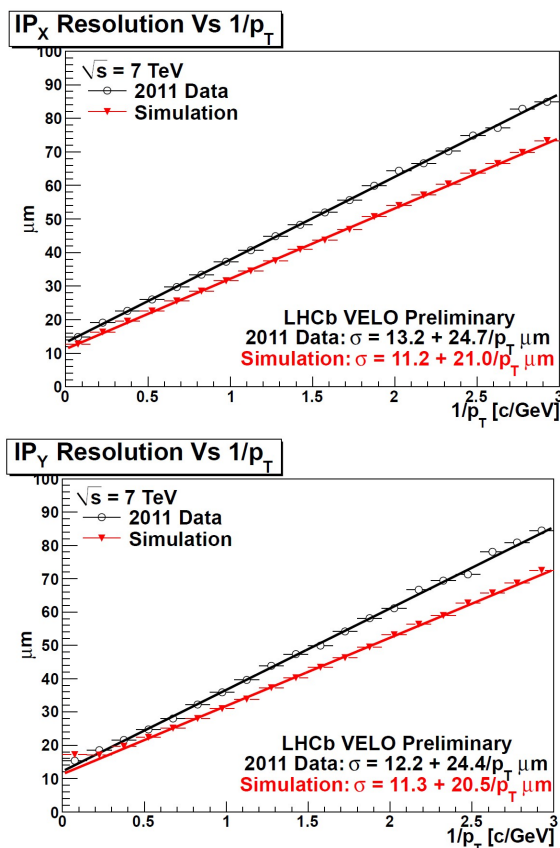
图 2.7 The resolution of VELO reconstructed PV in (left) x and (right) z direction for early 2011 data.

placed mirror-symmetrically to each other in the magnet yoke. To have the required momentum resolution for charged particles, the magnetic field integral $\int Bdl$ must be determined with a relative precision of order of 10^{-4} , and the position of the B-field peak with a precision of a few millimeters. The magnetic field was mapped with an array of Hall probes. The measured vertical field on z axis is shown in Figure 2.14 for both magnet polarities.

2.2.1.5 The track finding algorithm

Charged particles leave hits in one or more of the tracking subdetectors. Depending on the paths charged particles transverse the detector, the following class of tracks are defined, as illustrated in Figure 2.15.

- **Long tracks** transverse all of the tracking subdetectors from the VELO to T stations. They have the most accurate momentum determination and therefore the most important tracks for physics analysis.

图 2.8 The IP resolution in (left) x and (right) y direction.

- **Upstream tracks** transverse through the VELO and the TT. Typically they are low momentum tracks which are bent out of the detector acceptance by the magnet. However, they pass through the RICH1 and may generate Cherenkov photons if their momentum is large enough. Therefore they are capable for understanding the backgrounds in the RICH PID algorithm. Although their momentum resolution is poor, they can also be used for flavour tagging or b -hadron decay reconstruction.
- **Downstream tracks** transverse through the TT and the T stations. In the most concerned cases they are the daughter particles of long-lived particles, such as K_S^0 or Λ .
- **VELO tracks** only leave hits in the VELO. In general they have large angle with respect to the beam axis or move backward. They are useful for PV reconstruction.
- **T tracks** only leave hits in the T stations. They are typically from secondary interactions but useful for RICH2 global pattern recognition.

The tracking algorithm is the procedure to restore the trajectories of charged particles using the hits in the trackers. The reconstruction process starts with a search of track seeds

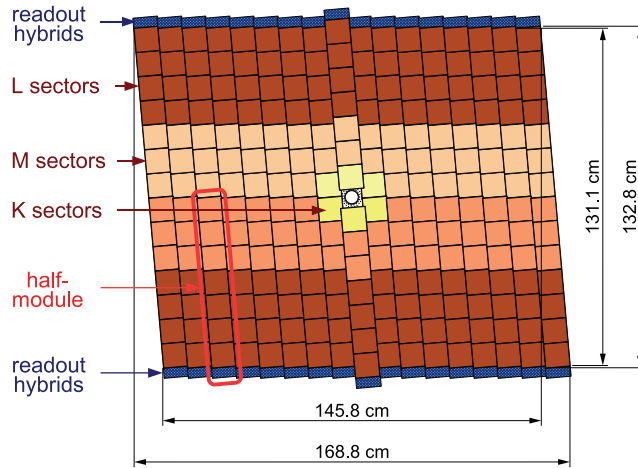


图 2.9 The layout of the third TT detection layer. Different readout sectors are indicated in different colors.

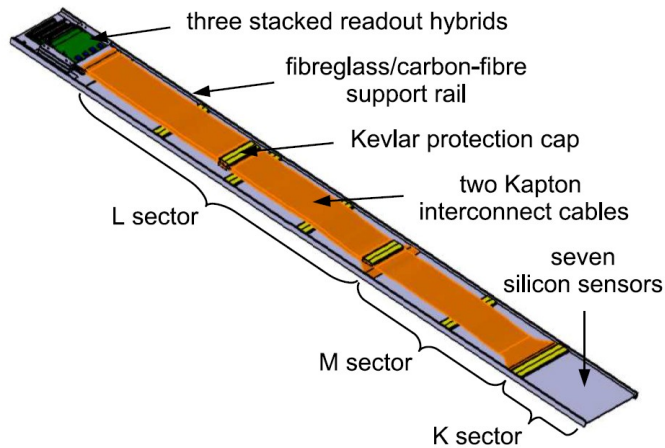


图 2.10 View of a TT detector module close to the beam pipe.

in the VELO, where the magnet field is sufficiently low that tracks can be considered as straight lines. The VELO seeds are then extended to the TT and T stations to find long tracks. This method, called forward tracking, already find a large fraction of long tracks. The hits used by forward tracking are discarded to save computing time. The search of seeds is also performed in the T stations, and the T seeds are matched to the VELO seeds left from the forward tracking to increase the reconstruction efficiency of long tracks. The VELO seeds not used by the forward tracking or tracking algorithm is extrapolated to TT stations to form upstream tracks. Downstreams is made by adding the TT hits to the T seeds. The VELO and T seeds that have not been used for a long, upstream and

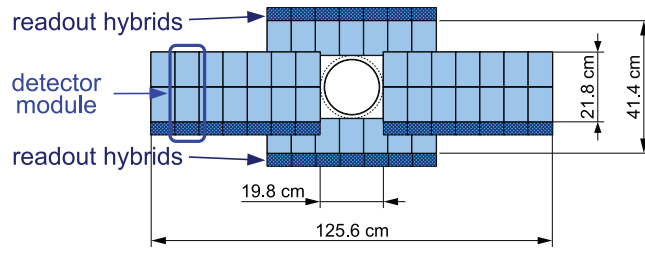


图 2.11 Layout of an x detection layer in the second IT station.

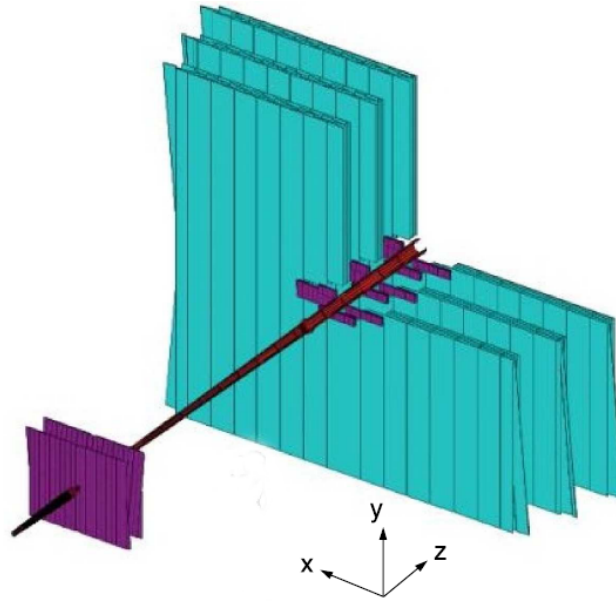


图 2.12 Arrangement of straw tube modules of the OT (cyan) in layers and stations. The TT and IT (purple) is also shown.

downstream track are classified as a VELO or T track. An example of a reconstructed event is displayed in Figure 2.16.

The nominal momentum resolution of the tracking system is $\delta p/p = (0.4 - 0.8)\%$ depending on the track momentum^[88], as shown in Figure 2.17. The tracking efficiency is measured by a data-driven method, the tag-and-probe method. This method employs two-body decays with one daughter particle, the “tag” leg, fully reconstructed, while the other daughter particle, the “probe” leg, reconstructed only using part of the detector information^[89]. The probe leg should carry enough information such that the number of the mother particles n_0 can be obtained from fit. The probe leg is then matched to fully reconstructed track, and the number of the mother particles n_1 can be found. The

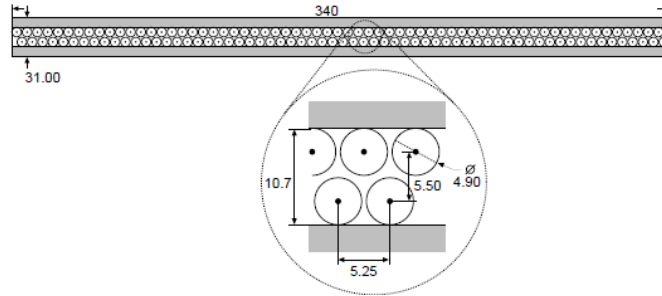


图 2.13 The cross-section of a straw-tubes module.

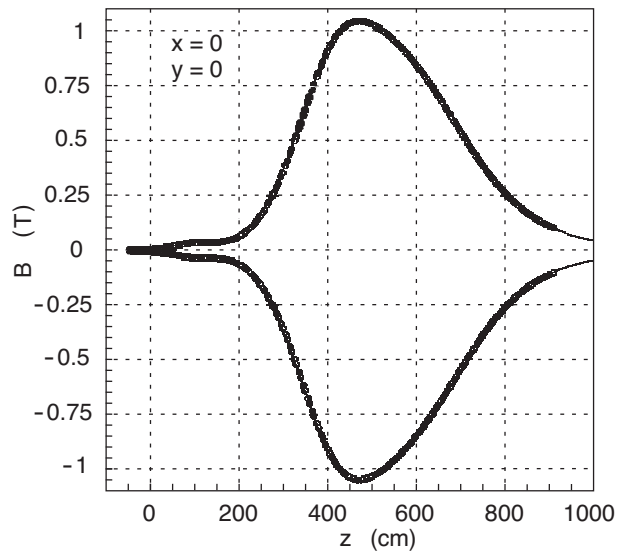


图 2.14 The vertical magnetic field along the z axis for both polarities.

efficiency is defined as

$$\varepsilon = \frac{n_1}{n_0} \quad (2-1)$$

Using $J/\psi \rightarrow \mu^+\mu^-$ decays, the tracking efficiency for data and MC in 2010 and 2011 are measured as a function of momentum and pseudo-rapidity as shown in Figure ???. The discrepancy between data and MC is small but corrections are needed. The application of this correction will be described in Section 3.5.2.1.

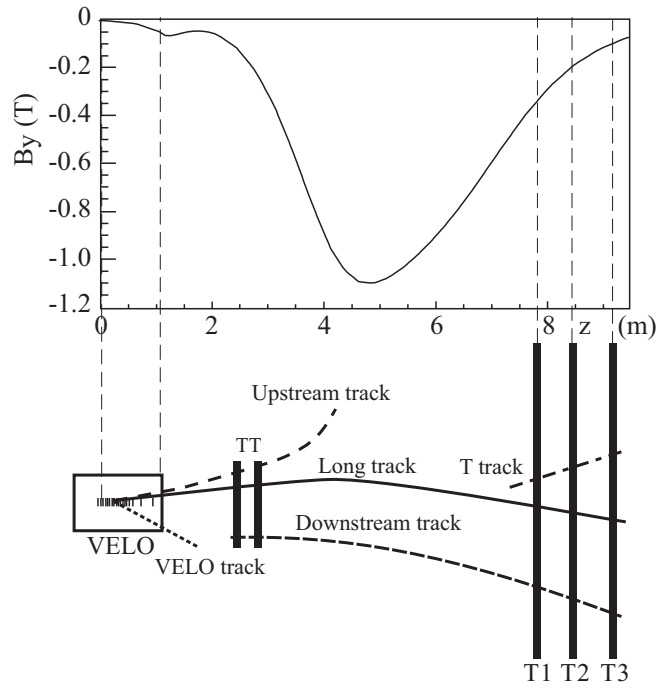


图 2.15 An illustration of the various track types: long, upstream, downstream, VELO and T tracks. The upper plot shows the main magnetic field component (B_y) as a function of the z coordinate^[84].

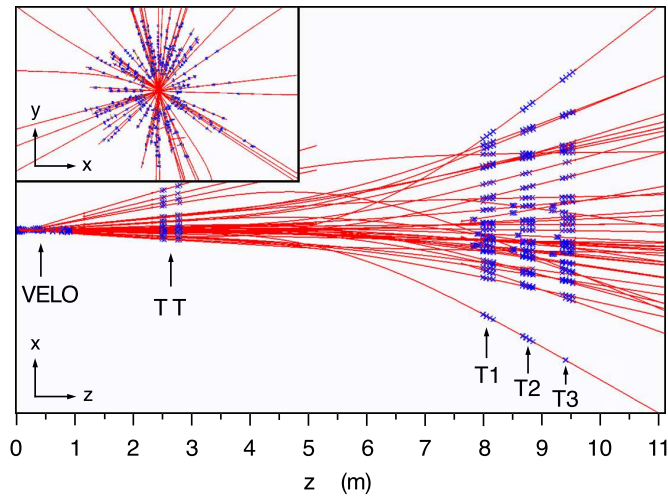


图 2.16 An example of the reconstructed tracks and assigned hits in an event. The insert plot shows a zoom in the vertical plane perpendicular to the beam into the VELO region^[84].

2.2.2 The PID system

LHCb intends to perform high precision measurements on b and c decays. In many instances the signal mode has physical backgrounds with similar topologies but one or

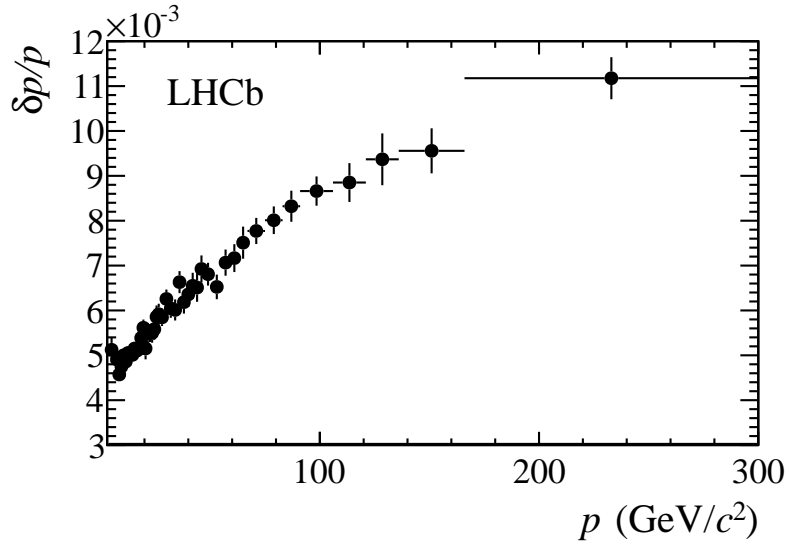


图 2.17 Relative momentum resolution as a function of the momentum for long tracks.

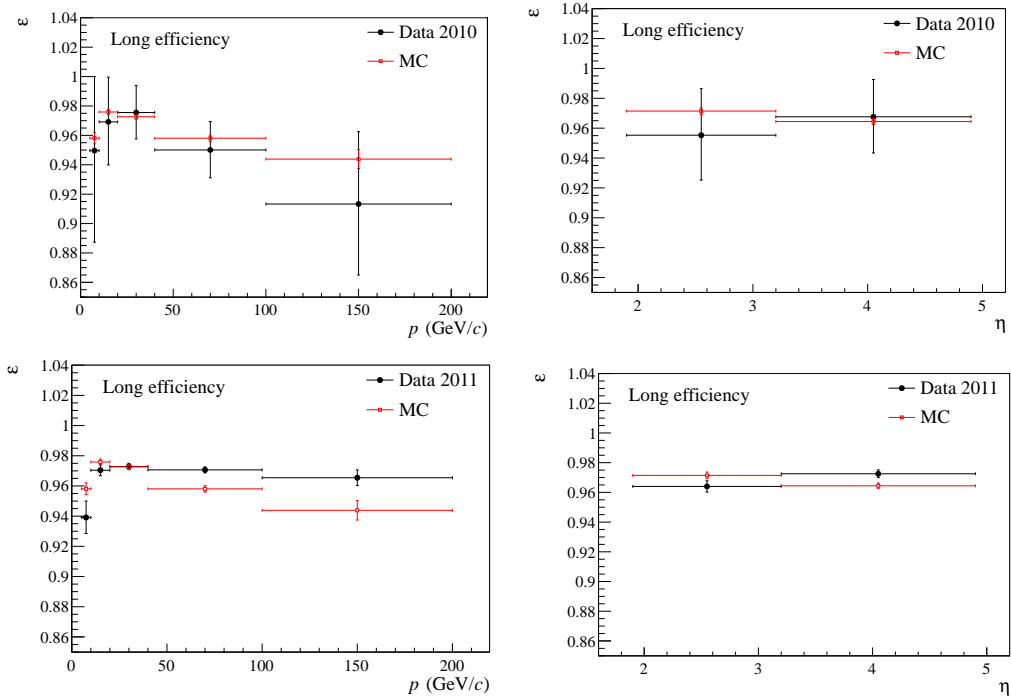


图 2.18 Tracking efficiency for data and MC in 2010 (top) and 2011 (bottom) as a function of momentum (left) and pseudo-rapidity (right). Efficiency from MC simulation is also shown.

more daughter particles changed. It is therefore essential to have an excellent discrimination between the tracks for the LHCb physics program. The PID system at LHCb includes the RICH detectors, the ECAL, the HCAL and the muon system.

2.2.2.1 The RICH detectors

The separation of hadrons, especially pions and kaons, is one of the fundamental requirements for LHCb. At LHCb the discrimination is accomplished by the RICH system, which uses the Cherenkov effect to identify different types of hadrons. The Cherenkov effect is the phenomenon that a charged particle emits a photon in the medium when it travels at a speed greater than the speed of light in that medium^[90]. The angle between the emitted photon and the instantaneous momentum of the particle is

$$\cos \theta = \frac{c}{nv}, \quad (2-2)$$

where c is the speed of light in vacuum, n is the refractive index of the medium and v is the speed of the particle. If the emission angle θ and the refractive index n is known, the velocity of the particle can be determined. Combined with the momentum information from the tracking system, the identity of the particle can be known.

LHCb needs to discriminate hadrons over a momentum range from 2 GeV/ c to beyond 100 GeV/ c . Two RICH detectors, RICH1 and RICH2 with different radiators, are constructed to cover this large momentum range. The distribution for the three RICH radiators from simulated events are shown in Figure 2.19. The RICH1 detector is optimized for identifying charged particles with low momentum of ~ 1 GeV/ c to 60 GeV/ c , therefore it uses aerogel and C₄F₁₀ gas as the radiators. It is located between the VELO and the TT, upstream of the dipole magnet to detect low momentum particles that may be swept out the acceptance by the magnet. The RICH1 covers the whole LHCb acceptance. To minimize the material budget for track reconstruction, spherical and flat mirrors are introduced to reflect and focus the Cherenkov photons onto Hybrid Photon Detectors which are situated outside of the acceptance. A schematic view of RICH1 is shown in Figure 2.20. The RICH2 detector, downstream of the T stations, covers a smaller acceptance of 120 mrad horizontally and 100 mrad vertically. It provides identification for charged particles with a momentum range of ~ 15 GeV/ c to beyond 100 GeV/ c , therefore CF₄ gas is used as the radiator. The mirror systems are also required to reflect and focus the photons to HPD. Figure 2.21 is a schematic view of the RICH2.

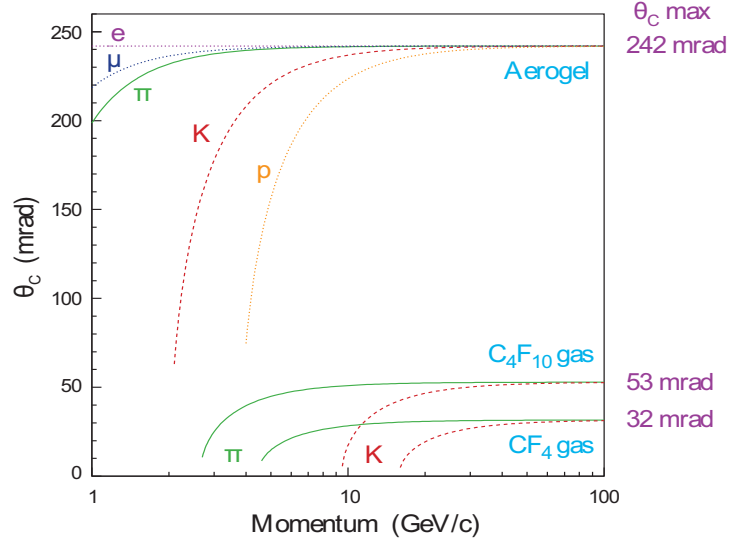


图 2.19 The simulated distribution of the Cherenkov angle as a function of particle momentum for three radiators^[84].

The particle identities are determined using a global likelihood algorithm^[91,92], where information from all the tracks, all radiators, and all the HPD photons of a given event are considered simultaneously^[93]. The algorithm calculates a likelihood for each particle hypothesis by comparing the predicted and observed distribution of the photo-electrons detected, and choose the hypothesis with the maximum likelihood. At the beginning of the algorithm, all the charged tracks are assumed to be pion, since pion is the most common type of tracks at LHCb, and the likelihood for this initial hypothesis is computed. Considering the first track, the mass hypothesis of the first track is change to electron, muon, kaon and proton, while hypotheses for other tracks are fixed, then the likelihood for each set of hypothesis are calculated. The first track is determined to be the mass hypothesis which gives the largest increase in the likelihood. This process is repeated for every track; the iteration stops when all tracks have been set to their optimal hypotheses, and no further improvement in the event likelihood can be found^[94]. The discrimination between different mass hypothesis are accomplished by the delta-log-likelihood, or DLL, which is defined as the log-likelihood difference between two different particle hypotheses of a track while keep the other tracks unchanged. As an example,

$$DLL_{K\pi} = \ln \left(\frac{L(t_1, t_2, \dots, t_i = K, \dots, t_n)}{L(t_1, t_2, \dots, t_i = \pi, \dots, t_n)} \right) \quad (2-3)$$

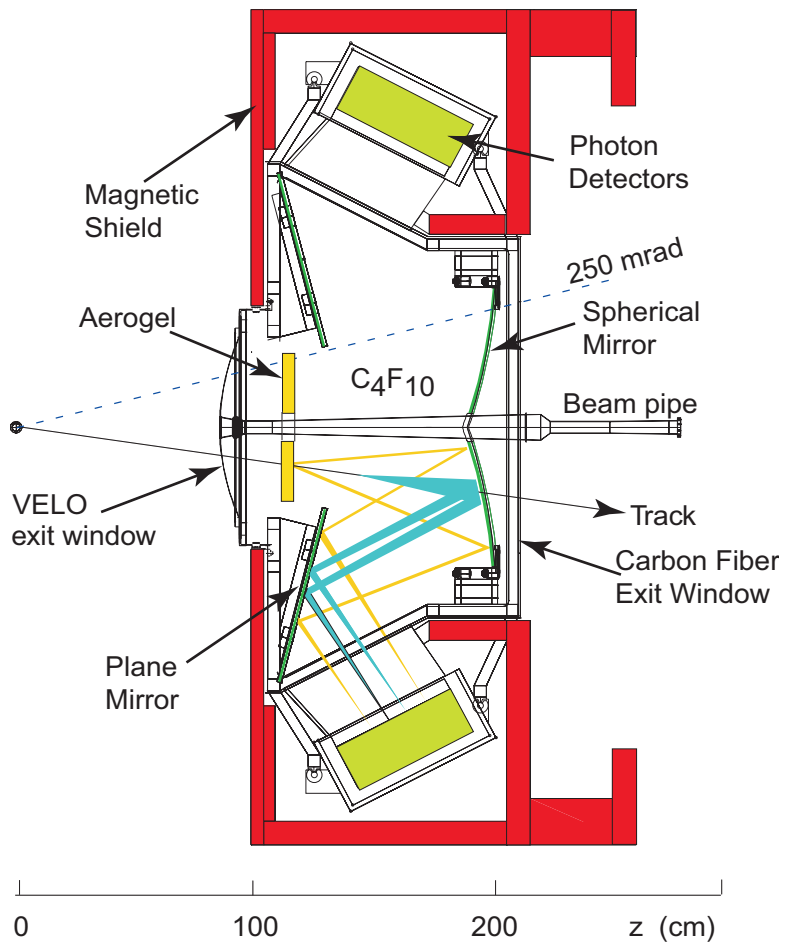


图 2.20 Schematic view of the RICH1 detector.

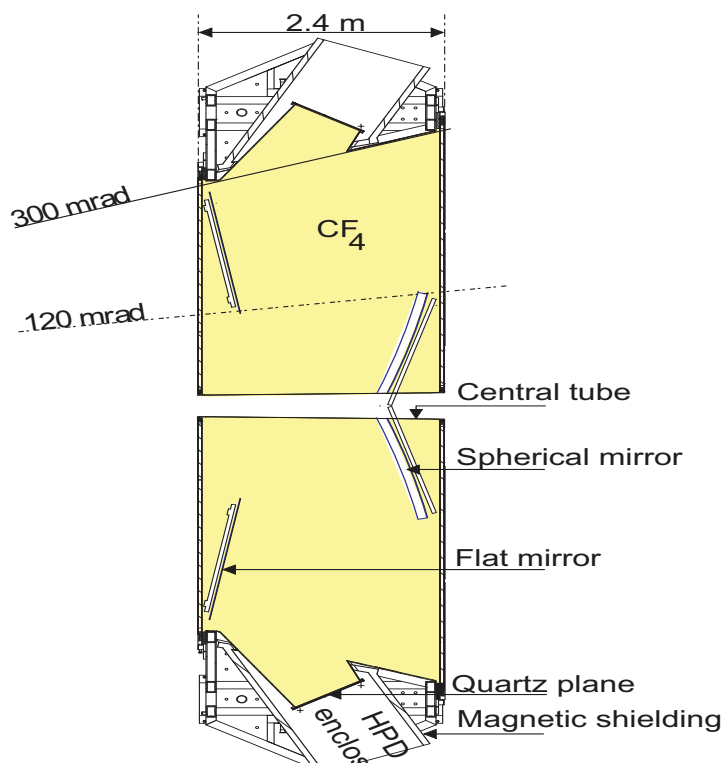


图 2.21 Schematic view of the RICH2 detector.

where $L(t_1, t_2, \dots, t_i, \dots, t_n)$ is the likelihood function, t_i is the i th track of the event.

In order to study the performance of the RICH system on data, large statistics samples of genuine K , π , and p are needed. Such control samples should be selected without any PID-related selection applied, otherwise the efficiency will be biased. The following decays, $\Lambda \rightarrow p\pi^-$, and $D^* \rightarrow (D^0 \rightarrow K^-\pi^+)\pi^+$ are selected only using the kinematic information. The residual background is subtracted with the *sPlot* technique^[95], where the invariant mass of Λ , D^* is chosen as the discriminating variable. Requiring kaons to be more consistent with the kaon hypothesis than the pion hypothesis, i.e $DLL(K - \pi) > 0$, the average kaon efficiency over the momentum range of 2 – 100 GeV/ c is found to be $\sim 95\%$, while the misidentification probability of pions is 10%. With tighter cuts the misidentification probability of pions could be reduced to $\sim 3\%$ with a kaon efficiency of $\sim 85\%$, as illustrated in Figure 2.22. Figure 2.23 demonstrates the discrimination between protons and pions. For $DLL(p - \pi) > 0$ and $DLL(p - \pi) > 5$, the average selection efficiency for protons is about 95% and 85%, while on average about 5% and 3% of pions is misidentified, respectively. Figure 2.24 shows the separation for protons and kaons. The performance of p K separation is similar as for p π at high momentum, but at low momentum the discrimination is much worse.

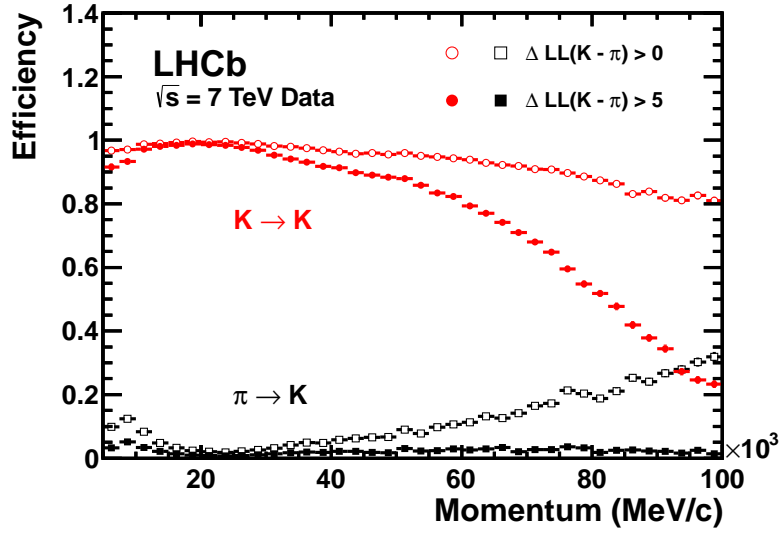


图 2.22 Kaon identification efficiency and pion misidentification rate measured on data as a function of track momentum. Two different $\Delta\log\mathcal{L}(K - \pi)$ requirements have been imposed on the samples, resulting in the open and filled marker distributions, respectively.^[94]

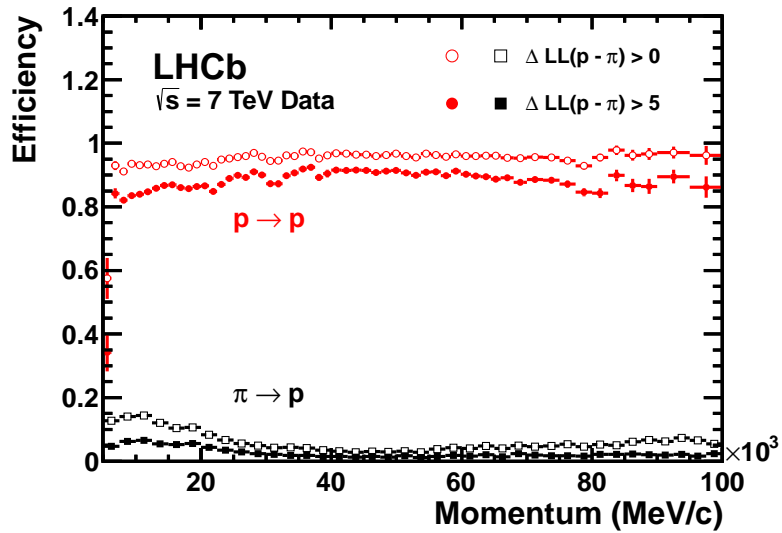


图 2.23 Proton identification efficiency and pion misidentification rate measured on data as a function of track momentum. Two different $\Delta\log\mathcal{L}(p - \pi)$ requirements have been imposed on the samples, resulting in the open and filled marker distributions, respectively.^[94]

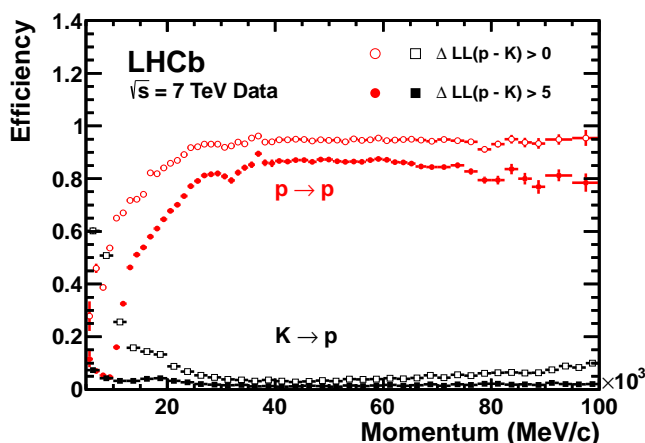


图 2.24 质子识别效率和 kaon 误识别率 measured on data as a function of track momentum. Two different $\Delta \log \mathcal{L}(p - K)$ requirements have been imposed on the samples, resulting in the open and filled marker distributions, respectively.^[94]

2.2.2.2 The LHCb calorimeters

The LHCb calorimeter system is designed to provide information for electrons, π^0 /photons and hadrons, which is crucial for the hardware level trigger and physics analyses involving electrons and neutral particles. It consists of four subdetectors: the scintillator pad detector (SPD), the preshower (PS), the electromagnetic calorimeter (ECAL) and the hadronic calorimeter (HCAL)^[84]. The calorimeters, located downstream of the first muon station, cover the LHCb acceptance of 25 mrad to 300 mrad horizontally and 25 mrad to 250 mrad vertically, where the inner acceptance is determined by the acceptable dose level.

The SPD/PS are composed of two almost identical planes of rectangular pads of high granularity, with a 15 mm thin lead converter inserted between^[84]. The SPD makes a distinction between high E_T electrons and high E_T photons and π^0 s, since only charged particles can interact with the scintillator of the SPD. The PS rejects the background of high E_T charged pions by detecting longitudinal segmentation of the electromagnetic shower initiated by the lead converter^[96]. The scintillation photons of the SPD/PS are transmitted to a Photo-Multiplier (PMT) by a single wavelength-shifting (WLS) fibres readout out using multianode photomultiplier tubes (MAPMT), as shown in Figure 2.25.

The ECAL, located downstream of the SPD/PS, is required to discriminate between electrons and hadrons, give a modest energy resolution while have a acceptable radiation resistance. It therefore adopts the reliable shashlik calorimeter technology, i.e. individual

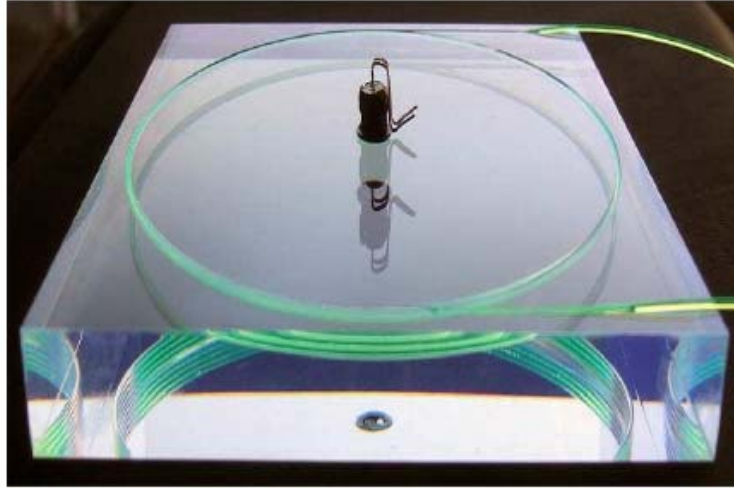


图 2.25 A SPD/PS detector cell with the WLS fibre layout and the LED housing in the middle^[84].

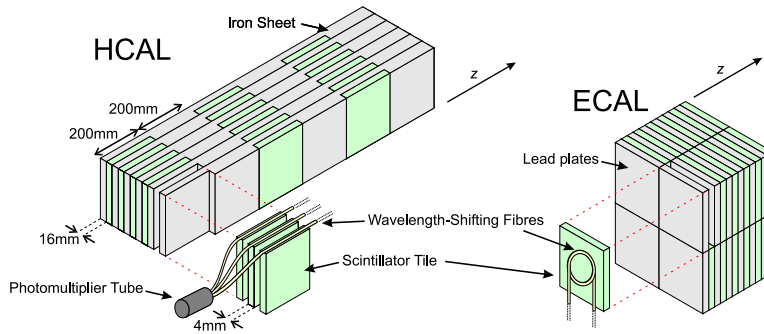


图 2.26 Schematic view of the LHCb HCAL (left) and ECAL (right), showing scintillator tiles, absorber plates and WLS readout fibres.

modules made of 4 mm thick scintillator tiles interleaved by 2 mm thick lead absorber plates (see Figure 2.26). The scintillation light is collected by the WLS fibres embedded in the tiles. The energy resolution of the ECAL is found to be

$$\frac{\sigma_E}{E} = \frac{10\%}{\sqrt{E}} \oplus 1\%, \quad (2-4)$$

where E is measured in GeV.

The particle density varies drastically from the inner section to the outer section, three lateral regions with different segmentation is then adopted for the SPD, PS and ECAL to match the detector occupancy, as shown in Figure 2.27. To allow for a faster hardware-level trigger decision and simplify the energy reconstruction, the segmentation

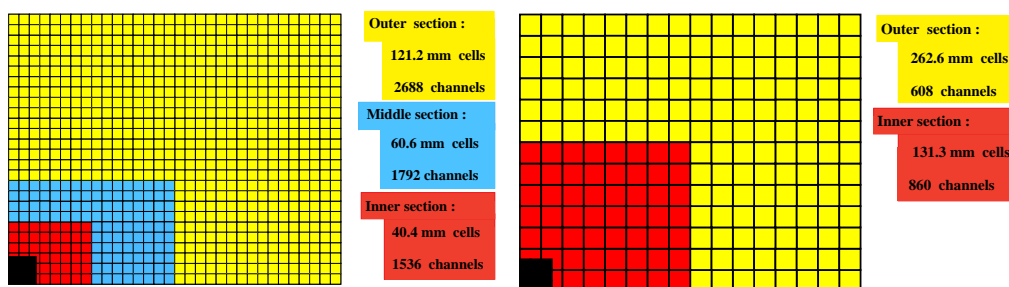


图 2.27 Lateral segmentation of the SPD/PS and ECAL (left) and HCAL (right), showing one quarter of the front face. The cell dimensions in the left figure are for the ECAL.

in the SPD and PS is scaled to match that of the ECAL projectively.

The HCAL, installed after the ECAL, is mainly used for hardware-level trigger, therefore the primary requirement is a fast response time rather than a high energy resolution. To make the hadrons deposit as much energy as possible in the detector, the HCAL is constructed in a sampling structure with iron as absorber, and scintillating tiles as active material (see Figure 2.26). The scintillating tiles has its orientation run parallel to the beam axis. The scintillation light is transported to PMT housed at the back side by WLS fibres, which run along the detector. The energy resolution of the HCAL is found to be

$$\frac{\sigma_E}{E} = \frac{(69 \pm 5)\%}{\sqrt{E}} \oplus (9 \pm 2)\%, \quad (2-5)$$

where E is measured in GeV. The HCAL is segmented into two region with larger cell size, as illustrated in Figure 2.27.

2.2.2.3 the MUON system

The muon system, consisting of five rectangular shape muon stations, provides identification for muons, which present in many important analysis at LHCb such as CP violation measurements and rare decays. Muons have a greater penetrating ability than other particles due to its lepton nature and large lifetime. Accordingly M2-M5 stations of the muon system are installed at the most downstream of LHCb, while M1 station is located before the calorimeters to improve the p_T measurement for trigger and full reconstruction. All the muon stations covers the same angular acceptance, 16 mrad to 300 mrad in the horizontal plane and 20 mrad to 258 mrad in the vertical plane, which means all their transverse dimensions are adjusted according to their distance from the interaction

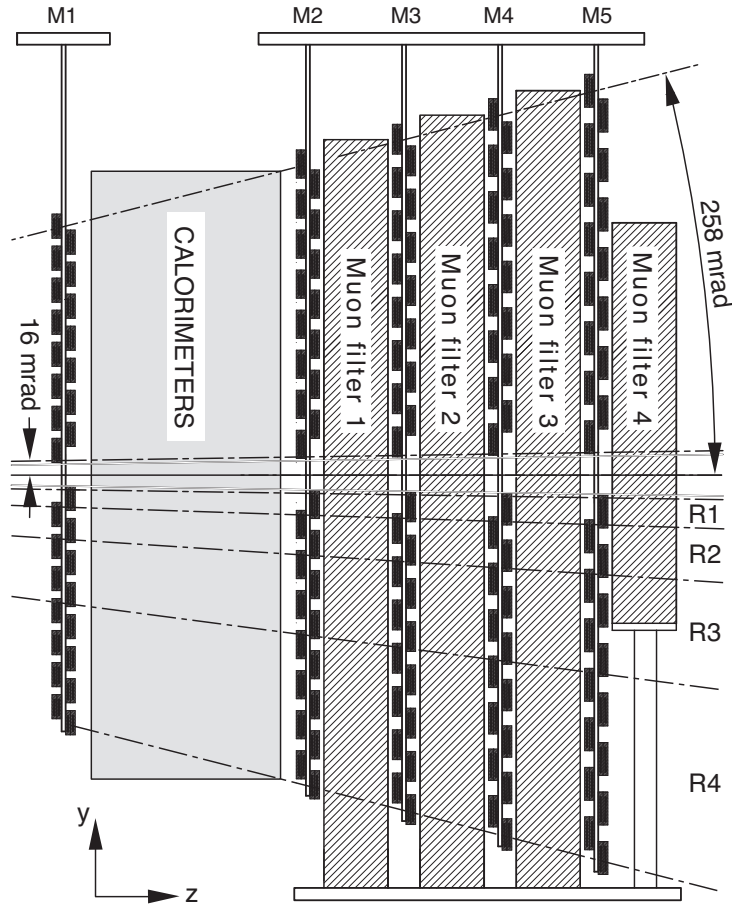
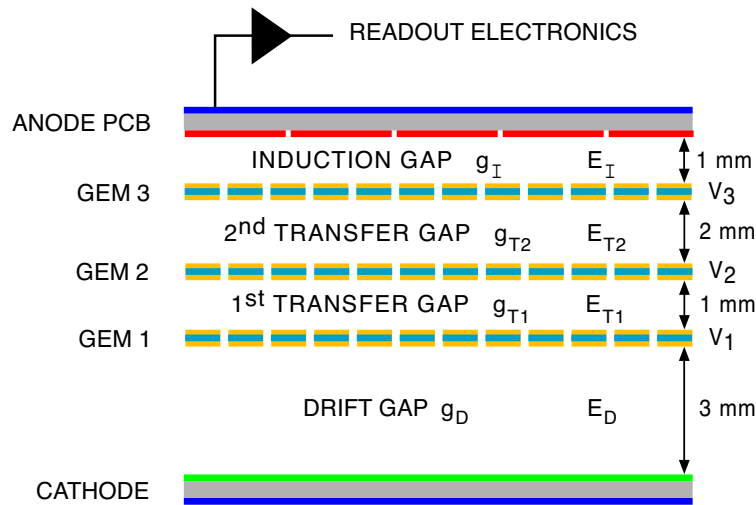


图 2.28 Side view of the muon system, with regions R1–R4 indicated^[84].

point. The particle flux decreases rapidly in the lateral direction, therefore each station is divided into four regions (R1–R4) so that the channel occupancy are roughly the same for each region of a given station. A sideview of the muon system is depicted in Figure 2.28.

The inner region (R1) of M1 station has the highest particle flux in all the regions, it is hence constructed to be two superimposed triple Gas-Electron-Multiplier (triple-GEM) detectors for the consideration of enhancing the radiation resistance^[97], while the rest of M1 and M2–M5 consists of multi-wire proportional chambers (MWPC)^[98]. Triple-GEM detectors are composed of three perforated gas electron multiplier foils sandwiched between an anode and a cathode plane, and the drift gap between foils is filled with a mixture of Ar/CO₂/CF₄. A cross section of the triple-GEM detector is shown in Figure 2.29. The two triple-GEM detectors of M1R1 are used in the logic OR state. In M2–M5 the MWPCs have four equal gas gaps with two adjacent gaps readout together in OR to create a


 图 2.29 Schematic view of the cross-section of a triple-GEM detector^[84].

double gap layer. In R2-R4 of M1 station the MWPCs only have two gas gaps, which are readout independently, to reduce the material in front of the ECAL. The gas used for MWPCs is also a mixture of Ar/CO₂/CF₄ but with different fractions.

2.2.2.4 The muon identification procedure and performance

The muon identification strategy is divided in three steps^[99,100]:

- A loose selection of muon candidates (called IsMuon) based on the penetration length of the muon candidates through the calorimeters and iron filters. This selection provides high efficiency for muons while reduces the hadron misidentification rate to percent level.
- Computation of likelihoods for the muon and non-muon hypotheses, based on the pattern of hits around the extrapolation to muon stations of charged particles. The difference between the logarithm of muon and non-muon hypotheses is used as the discrimination variable.
- Computation of a combined likelihood with information from the calorimeter and RICH systems included. The difference between the logarithm of muon and non-muon hypotheses is used as the discrimination variable.

The performance of the muon identification is extracted from large statistics samples of muon, pion, kaon, and proton, which are selected using kinematical requirements only. These samples could be purified further with a tag-and-probe technique if needed. The

pion, kaon, and proton samples are selected using the same decays as for RICH performance evaluation. The muon sample is enriched using the inclusive $B \rightarrow J/\psi X$ decay. The identification efficiency for muon and misidentification rate for pion, kaon, and proton are shown in Figure 2.30. The performance of the muon identification depends on the track momentum. With the IsMuon and muDLL cuts, the average muon efficiency could be at the level of 93%, while the misidentification rate is suppressed below 0.6%^[100].

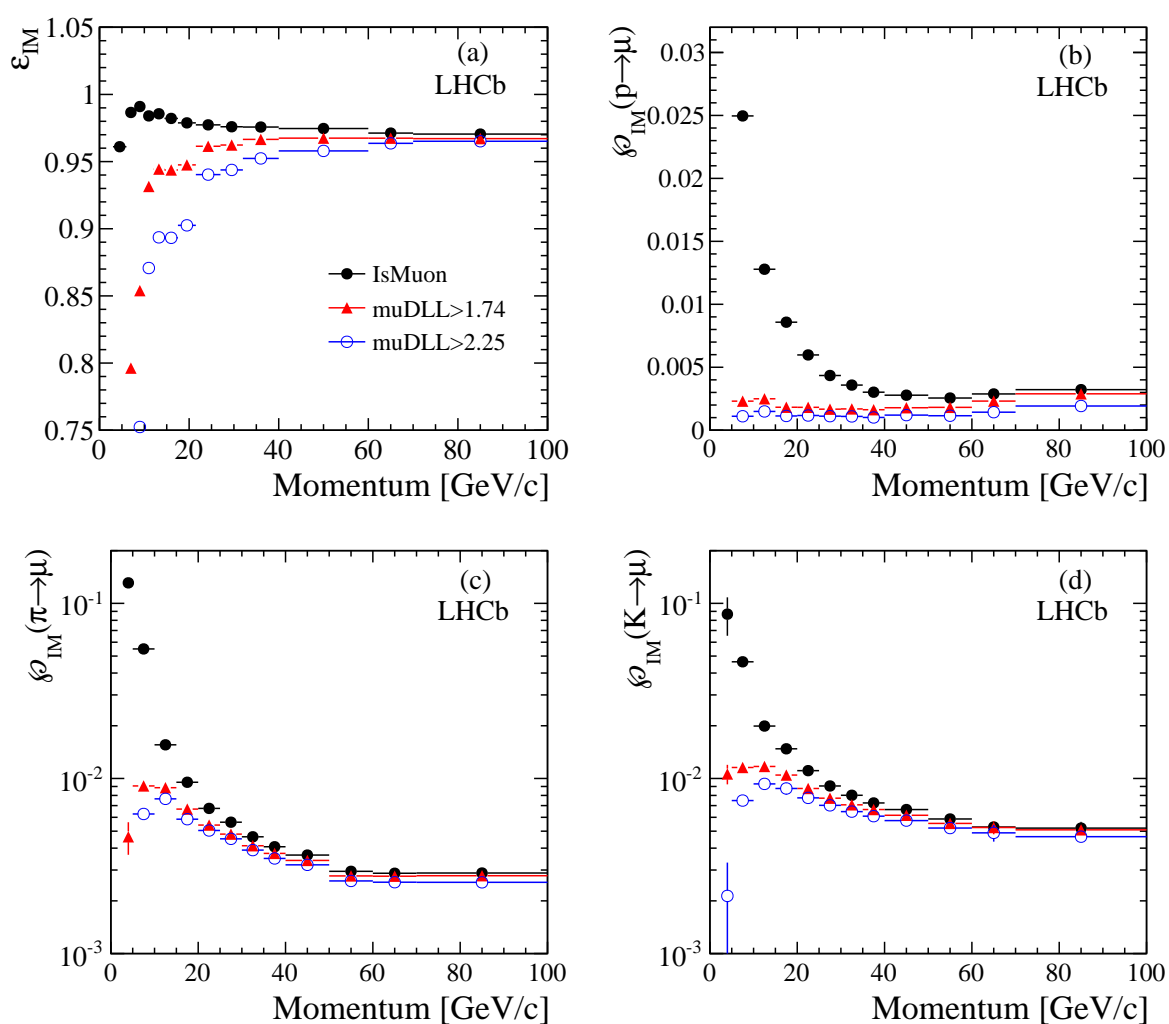


图 2.30 Muon efficiency (a) and misidentification rate for protons (b), pions (c) and kaons (d) as a function of the particle momentum for the IsMuon requirement alone (black solid circles) and with the additional cuts $\text{muDLL} \geq 1.74$ (red triangles) and $\text{muDLL} \geq 2.25$ (blue open circles)^[100].

2.3 The LHCb trigger

As a hadron collider, most of the collisions events at the LHC do not produce decays of interest. An efficient trigger system is fundamental to only keep the events we want to study further. The LHCb trigger system consists of two levels: the Level-0 (L0) and the High Level Trigger (HLT). The L0 is implemented at hardware level, and the HLT is a software trigger run on an online computing farm called the Event Filter Farm (EFF)^[84,101,102].

2.3.1 Level-0 trigger

The L0 trigger reduces the inelastic event rate of 16 MHz to about 1 MHz, the maximum rate at which the full detector response can be readout^[103]. L0 is divided to three independent parts, the L0-Calorimeter trigger, L0-Muon trigger and the L0-PileUp trigger. The trigger decisions from these triggers are combined in L0 Decision Unit (L0DU), and further transferred to the Readout Supervisor board (RS). The RS decides to accept or throttle a L0 trigger based on the information of L0DU and the availability of other subdetectors and the EFF. The trigger decisions from L0DU is sent to the Readout Supervisor board (RS). The RS decides to accept or reject the event based on the information of L0DU and the availability of other subdetectors and the EFF.

The L0-Calorimeter trigger selects the event using information from the SPD, PS, ECAL and the HCAL. As stated in Section 2.2.2.2, the calorimeters are segmented into cells to balance the detector occupancy. The L0-Calorimeter system then calculates the transverse energy deposited in clusters of 2×2 cells, using only cells of the same size. The transverse energy is defined as

$$E_T = \sum_{i=1}^4 E_i \sin \theta_i \quad (2-6)$$

where E_i is the energy deposited in cell i and θ_i is the angle between the beam axis and the hypothetical connection line between the interaction point and the center of the cell. Three types of candidates are defined based on the hit and E_T information as follows:

- hadron candidate (L0Hadron): the HCAL cluster with the highest E_T .
- photon candidate (L0Photon): the ECAL cluster with the highest E_T , with 1 or 2 PS cells hit and no hit in the SPD cells corresponding to the PS cells.
- electron candidate (L0Electron): the same requirements as for a photon candidate

with in addition at least one SPD cell hit in front of the PS cells.

The E_T threshold is set for each type of the candidates. The results from L0-Calorimeter system are then compared to these thresholds, and if lower, the event will be rejected. The total number of hits in the SPD is also determined, which is used to veto events which contain too much tracks to be processed in a reasonable time in the HLT.

The muon system is divided into four quadrants in $x - y$ plane with each connected to a L0 muon processor. The processors look for the two muon track candidates with the largest and second largest p_T in their quadrant. The L0-Muon trigger sets a threshold on either the largest p_T of the eight candidates (L0Muon) or a threshold on $p_T^{largest} \times p_T^{2ndlargest}$ (L0DiMuon).

The L0-PileUp system consists of two planes of $R-$ sensors placed upstream of the VELO system. It is originally implemented to reject events with several primary vertices, but given LHCb is running at a higher μ than foreseen in the design, events with pile-up are not rejected. It provides trigger for beam-gas events which are used in the determination of the luminosity. –cite

2.3.2 High-Level Trigger

High-Level Trigger is a series of algorithms written in C++ to process the events accepted by L0, and 26110 copies of it run in the EFF. The HLT is implemented in two stages, HLT1 and HLT2. Each stage consists of trigger lines, each of which is dedicated to a certain class of events of interest. The lines are configured by a python script, which defines reconstruction algorithms and selection criteria. HLT2 will only be executed for the events which are accepted by at least one of the lines of the HLT1.

The selection of the HLT1 lines begins with the selections on the VELO tracks. Hlt1 lines which do not require muons select VELO tracks based on their smallest impact parameter (IP) to any PV as well as the quality of the VELO track. For events selected by L0Muon or L0DiMuon, a fast muon identification is performed by matching VELO tracks with the hits in the muon chambers. The momentum of the selected VELO tracks is determined accurately using a Kalman filter based track fit with a simplified material geometry description. The invariant mass resolution of $J/\psi \rightarrow \mu^+\mu^-$ in the HLT is only 3% larger than in the offline reconstruction.

The event rate from HLT1 is low enough so that forward tracking of all VELO tracks can be performed in HLT2, although the track matching between VELO tracks and

T tracks does not happen due to time constraint. Information from all subdetectos can be used. HLT2 consists of several inclusive beauty hadron trigger lines and many exclusive charm and beauty hadron trigger lines. The inclusive beauty hadron trigger lines select b -hadron signals using a multivariate method based on two signatures: a displaced and high transverse momentum track, and a displaced vertex containing this track and other 1-3 tracks^[104]. The exclusive trigger lines select prompt charm decays, and other interesting decays which cannot be triggered by the inclusive lines. For bandwidth reason, trigger lines with plethoric production rate are prescaled; events which meet all the selection cuts of these trigger lines will be discarded randomly.

2.3.2.1 Deferral trigger

In 2012 a novel technique, deferral trigger, was introduced to the trigger system^[105]. In normal operation the beams of the LHC are dumped when their intensity decays below some threshold. It could take a few hours to start another fill. Before the implementation of the HLT deferral system, the EFF were in idle during this interfill period and the computation power were wasted. To keep the EFF running when LHC is preparing for the next collision, a fraction of the events which are accepted by L0 are cached in EFF storage instead of processed. When the beams are dumped, the EFF can process these events. The net result is that the available computing power increased approximately 20% in 2012.

2.3.2.2 The TCK

Both L0 and HLT can be configured via a unique hexadecimal key, named Trigger Configuration Key (KEY), which defines the sequence of lines included in the trigger and the thresholds and selection criteria for these lines.

2.3.3 The TISTOS method

The trigger efficiency is always evaluated relative to the offline reconstruction and selections. However, the inefficiency due to the possible alignment inaccuracies and different reconstruction algorithms in trigger and offline has to be taken into account. The trigger efficiency can be determined by a data-driven method called TISTOS^[102]. Two categories of the data sample, TOS and TIS, are defined as follows:

- TOS (Trigger On Signal): the signal candidate or one of its constituent parts triggered the event;
- TIS (Trigger Independent of Signal): the event was triggered independently of the presence of the signal candidate.

By definition, the efficiency of TOS events can be determined as

$$\varepsilon^{\text{TOS}} = \frac{N_{\text{TOS—Sel}}}{N_{\text{Sel}}}, \quad (2-7)$$

where N_{Sel} is the size of the hypothesized sample that is filtered by the selection but not by the trigger, and $N_{\text{TOS—Sel}}$ is the size of the sample been selected and TOSed. However, N_{Sel} is not an observable since in real data all the events are selected by some trigger lines otherwise they will not be recorded. The TIS sample could provide an unbiased sample for selection if the correlation between TIS and selections is small enough. Then the TOS efficiency is given by

$$\varepsilon^{\text{TOS}} = \frac{N_{\text{TISTOS—Sel}}}{N_{\text{TIS—Sel}}}. \quad (2-8)$$

2.3.4 The performance of the trigger system

The performance of the trigger system is extracted using the TISTOS method. L0Hadron selects decays with hadrons in the final state. The performance of L0Hadron is shown in Figure 2.31 for $B^0 \rightarrow D^+\pi^-$, $B^+ \rightarrow D^0\pi^+$, $D^0 \rightarrow K^-\pi^+$ and $D^+toK^-\pi^+\pi^+$ as a function of p_T of signal mesons. The TOS efficiency of L0Hadron is very sensitive to the p_T of signal mesons due to the E_T cut of tracks in L0.

Hlt1TrackAllL0 is an HLT1 line which is executed for all L0 triggers. It selects hadron decays with a finite lifetime, e.g. $\Lambda_c^+ \rightarrow pK^-\pi^+$ decay. The performance of Hlt1TrackAllL0 is shown in Figure 2.33 for $B^0 \rightarrow D^+\pi^-$, $B^+ \rightarrow D^0\pi^+$, $D^0 \rightarrow K^-\pi^+$ and $D^+toK^-\pi^+\pi^+$ as a function of p_T of signal mesons. Hlt1TrackAllL0 provides a very efficient trigger for heavy flavour decays with a finite distance from their PV.

2.4 The LHCb software framework

The LHCb software framework consists of a series of projects built on Gaudi, an experiment independent event data processing framework^[106]. Gaudi is an object-oriented

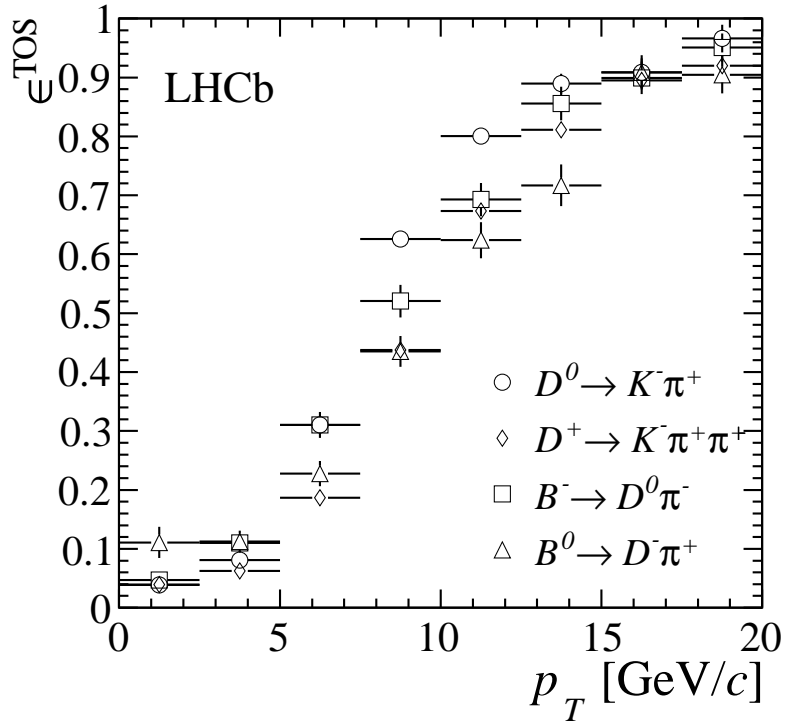


图 2.31 The TOS efficiency of L0Hadron as a function of p_T of signal mesons^[102].

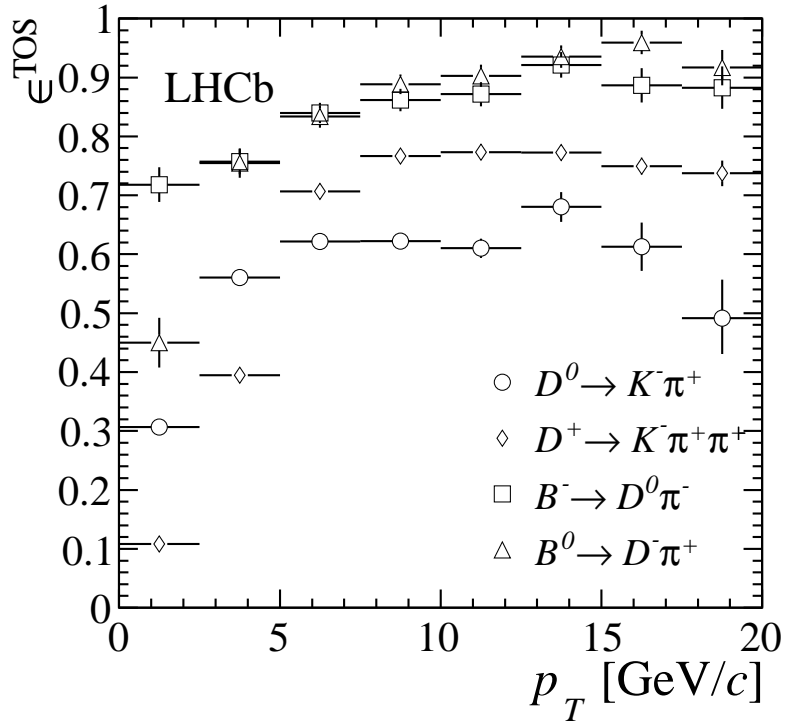


图 2.32 The TOS efficiency of H1t1TrackAllL0 as a function of p_T of signal mesons^[102].

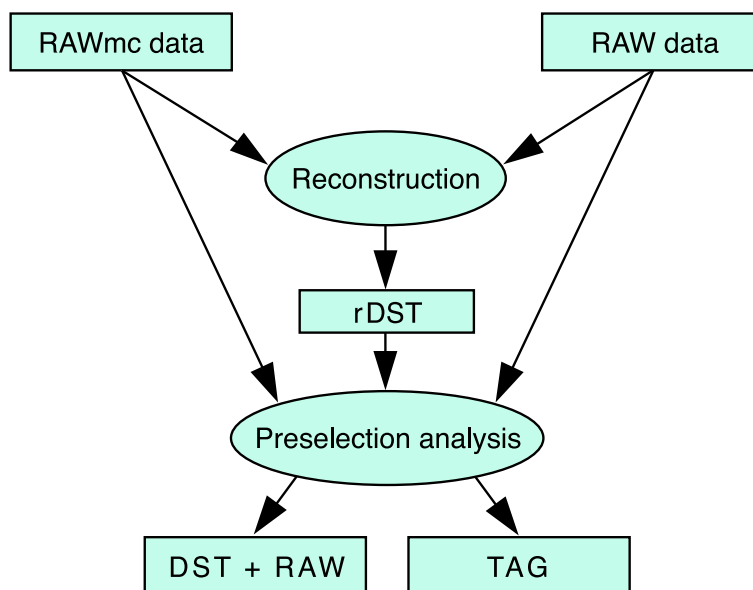


图 2.33 The TOS efficiency of H1t1TrackAllL0 as a function of p_T of signal mesons^[102].

C++ framework that provides common interfaces and services for building HEP experiment data processing frameworks. The main LHCb software projects are built for different level of data processing, from simulation to reconstruction and final analysis.

2.4.0.1 Simulation

Monte Carlo (MC) events generation at LHCb is handled by the GAUSS project^[107–110]. GAUSS builds a framework for event generation, and invokes toolkits available in the HEP community at each stages of MC, from event generation to particle decay and full detector simulation. The main generator for GAUSS is PYTHIA^[111], but it is also possible to migrate dedicate generators for production. This is extremely useful if a specific particle has such a small production cross-section that PYTHIA is very inefficient to produce it. An example for this is Ξ_{cc}^+ , which is difficult to generate directly from PYTHIA due to two heavy quarks. A dedicate generator, GENXICC^[112–114], is therefore developed for hadronic production of Ξ_{cc}^+ . It is written in a PYTHIA-compatible format and can be easily incorporated into PYTHIA. The interface between GENXICC and GAUSS has been implemented, so that it can be used within the LHCb software framework^[115]. The decay of particles is simulated by EVTGEN^[116], and the interaction of the generated particle with the detector and its response are implemented using the GEANT4^[117,118].

The output of GAUSS are transferred to BOOLE^[119], which emulates the detector re-

sponse using the information of GAUSS. This includes the readout electronics and L0 trigger as well as the noise, cross-talk and spill-over from previous bunch crossings. The output of BOOLE is in the same format as for real data, and after that the MC sample are processed in the same way as for real data.

2.4.0.2 Trigger

The HLT (software trigger) is implemented by a project called Moore^[120]. Moore can either run in the online EFF to process online data from the LHCb DAQ system, or offline on real data or MC samples digitalized by BOOLE. It can be used in two modes: rejection mode and flagging mode. In former case only the events pass the trigger lines are saved, while in the latter case all the events are saved and the pass/fail information for all trigger lines are added.

2.4.0.3 Reconstruction

The project for performing the track reconstruction at LHCb is called BRUNEL^[121]. It proceeds MC samples and real data in the same way. The BRUNEL not only reconstructs all the charged tracks, but also performs particle identification for the tracks found in RICH, ECAL and muon system.

2.4.0.4 Data Analysis

DAVINCI^[122] is the LHCb physics analysis software for final event reconstruction. With various dedicated packages, DAVINCI is very versatile for event reconstruction, including the flavour tagging, the lifetime fit and vertex reconstruction, etc. The DAVINCI produces ntuples for local analyses.

第 3 章 The Ξ_{cc}^+ analysis in 2011

This chapter presents the search for the doubly charmed baryon Ξ_{cc}^+ at LHCb using 2011 data. The Ξ_{cc}^+ baryon is searched by $\Xi_{cc}^+ \rightarrow \Lambda_c^+ K^- \pi^+$, and $\Lambda_c^+ \rightarrow p K^- \pi^+$. To minimize the systematic uncertainties, the Ξ_{cc}^+ production cross-section is measured relative to that of Λ_c^+ , and the upper limits for the ratio is given across a large invariant mass range for five different lifetime hypotheses. The contents are organized as follows: the strategy is reviewed in Section ??, the data samples used are described in Section 3.2, followed by an overview of the selection criteria for the Ξ_{cc}^+ analysis in Section 3.4. The determination of the yield is given in Section 3.6, followed by the description of the efficiency ratio in Section 3.5. The systematic uncertainties are considered in Section ??, and the upper limits for each lifetime hypothesis are calculated in Section ??. Finally, the results will be presented in Section ??.

3.1 Strategy

The Ξ_{cc}^+ baryon is searched through the decay $\Xi_{cc}^+ \rightarrow \Lambda_c^+ K^- \pi^+$, where Λ_c^+ is reconstructed through $\Lambda_c^+ \rightarrow p K^- \pi^+$. In order for our result to be compared to theory predictions and to other experiments, it is not enough to measure (or put a limit on) the yield alone. The cross-section or the ratio of cross-sections of Ξ_{cc}^+ and an appropriate control mode should be given. But the decay $\Xi_{cc}^+ \rightarrow \Lambda_c^+ K^- \pi^+$ has a comparatively short lifetime and moderate Q -value, which make it very different from b -hadron decays, and the non-zero lifetime separates it from strong decays of Ξ_c resonances. Instead, inclusive Λ_c^+ production, again reconstructed through $\Lambda_c^+ \rightarrow p K^- \pi^+$. This reduces systematic uncertainties (including full cancellation of the Λ_c^+ branching fraction, which has an uncertainty of 26%^[48]). It also allows for a direct comparison with previous experiments that quoted a similar ratio.

The production cross-section of the Ξ_{cc}^+ baryon can be expressed as

$$\sigma_{\Xi_{cc}^+} = \frac{N_{\Xi_{cc}^+}}{\mathcal{L} \times \varepsilon_{\Xi_{cc}^+} \times \mathcal{B}(\Xi_{cc}^+ \rightarrow \Lambda_c^+ K^- \pi^+) \times \mathcal{B}(\Lambda_c^+ \rightarrow p K^- \pi^+)} \quad (3-1)$$

where $\sigma_{\Xi_{cc}^+}$ is the production cross-section we want to measure, $N_{\Xi_{cc}^+}$ is the yield of Ξ_{cc}^+ after all the selections, \mathcal{L} is the integrated luminosity, $\varepsilon_{\Xi_{cc}^+}$ is the selection efficiency for

this decay, and $\mathcal{B}(\Xi_{cc}^+ \rightarrow \Lambda_c^+ K^- \pi^+) \times \mathcal{B}(\Lambda_c^+ \rightarrow p K^- \pi^+)$ is the adjoint branching fraction of the Ξ_{cc}^+ decay.

Similarly, for the Λ_c^+ baryon, the production cross-section is given by

$$\sigma_{\Lambda_c^+} = \frac{N_{\Lambda_c^+}}{\mathcal{L} \times \varepsilon_{\Lambda_c^+} \times \mathcal{B}(\Lambda_c^+ \rightarrow p K^- \pi^+)} \quad (3-2)$$

Using $\Lambda_c^+ \rightarrow p K^- \pi^+$ as the normalization channel, the production ratio can be measured as

$$R \equiv \frac{\sigma(\Xi_{cc}^+) \mathcal{B}(\Xi_{cc}^+ \rightarrow \Lambda_c^+ K^- \pi^+)}{\sigma(\Lambda_c^+)} = \frac{N_{\text{sig}} \varepsilon_{\text{con}}}{N_{\text{con}} \varepsilon_{\text{sig}}} \quad (3-3)$$

where sig and con refer to the signal (Ξ_{cc}^+) and control (Λ_c^+) modes.

The subconscious bias from subjective cognition is very likely to bias physics results in an involuntary way, especially for an analysis to search for a particle. Therefore, the analysis is performed with a blind approach: the signal region is kept blinded throughout the whole process, until all the analysis procedures are frozen. Since the mass of Ξ_{cc}^+ is unknown, a large signal region corresponding to $3.3 < m(\Xi_{cc}^+) < 3.8 \text{ GeV}/c^2$ is blinded. Correctly reconstructed signal should peak both in $m(\Xi_{cc}^+)$ and in $m(\Lambda_c^+)$. The errors on these two variables are correlated, so in practice we work with $m(\Lambda_c^+)$ and the mass difference δm , defined as

$$\delta m \equiv m(p K^- \pi^+ K^- \pi^+) - m(p K^- \pi^+) - m(K^-) - m(\pi^+) \quad (3-4)$$

where $m(p K^- \pi^+)$ is the reconstructed mass of the Λ_c^+ candidate.

3.2 Data Sample

The search for the doubly charmed baryon Ξ_{cc}^+ is performed with the data collected at a center-of-mass energy of 7 TeV at LHCb, corresponding to an integrated luminosity of 0.65 fb^{-1} . The data is reconstructed by the standard LHCb data processing of Reco12, Stripping17. The Ξ_{cc}^+ and Λ_c^+ candidates are extracted from the stripping lines `StrippingXiccXiccPlusToLcKPi` and `StrippingXiccControlLc` in stream `Charm`, respectively.

Monte-Carlo samples of Λ_c^+ are generated in the normal way with PYTHIA. However, as mentioned in Section ??, the default PYTHIA configuration is very inefficient for Ξ_{cc}^+ production due to the presence of two heavy charm quarks in Ξ_{cc}^+ . Therefore, the generator GENXICC is employed for hadronic production of Ξ_{cc}^+ at LHCb. The mass and lifetime of

Ξ_{cc}^+ are not known, and the input parameters for the generator have been chosen based on the theoretical predictions: $m(\Xi_{cc}^+) = 3500 \text{ MeV}/c^2$ and $\tau(\Xi_{cc}^+) = 333 \text{ fs}$. The efficiency varies with mass and lifetime, and this will be taken into account when the upper limits for different mass and lifetime hypotheses are given. The Monte-Carlo samples of Λ_c^+ and Ξ_{cc}^+ are produced under the following circumstances: GAUSS v41r3, BOOLE v23r1, MOORE v12r8g1, BRUNEL v41r1p1 and DAVINCI v29r1p1. The samples have been flagged with TCK0x40760037 and Stripping17, the same criteria as data, except all the prescale factors are set to 1.

3.3 $\Xi_{cc}^+ \rightarrow \Lambda_c^+ K^- \pi^+$ reconstruction

A schematic of the topology of a $\Xi_{cc}^+ \rightarrow \Lambda_c^+ K^- \pi^+$ decay is shown in Figure 3.1. In each proton-proton collision event PVs are reconstructed from all the tracks which have been reconstructed by the VELO. As we do not consider the Ξ_{cc}^+ from b hadrons decay, the Ξ_{cc}^+ signal always originates from PV. With a moderate lifetime of 300 fs, the Ξ_{cc}^+ travels a short but sizable distance and decays to Λ_c^+ , K^- , and π^+ to form a secondary vertex. The Λ_c^+ has a lifetime of 200 fs, therefore it could also move a short distance before decays to p , K^- , and π^+ . In the reconstruction process, three tracks which consist of proton, kaon, and pion hypotheses are searched and combined within selection criteria to form Λ_c^+ candidates; two more tracks that consist of kaon and pion hypotheses and have not been used in the Λ_c^+ reconstruction will be combined with the Λ_c^+ to form Ξ_{cc}^+ candidates.

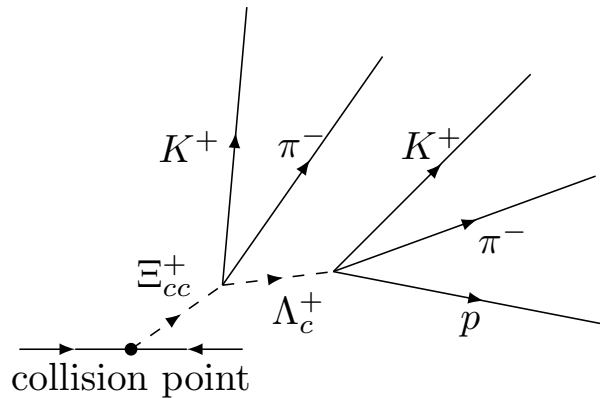


图 3.1 The Ξ_{cc}^+ decay topology, on which the selection criteria are based

3.4 Selections

The decay $\Xi_{cc}^+ \rightarrow \Lambda_c^+ K^- \pi^+$ is purely hadronic, and the lifetime of Ξ_{cc}^+ and Λ_c^+ baryon are moderate (~ 200 fs), therefore a large fraction of combinatorial background is expected. To keep the background level as low as possible, both Ξ_{cc}^+ and Λ_c^+ candidates are required to pass stripping, offline rectangular cuts and trigger requirements, which are aligned as much as possible to minimise the systematic uncertainties. In addition, a multivariate selection are applied to the Ξ_{cc}^+ mode only (i.e. not to the Λ_c^+ control mode). This is needed because the expected Ξ_{cc}^+ yield is many orders of magnitude smaller than that for Λ_c^+ , so stronger background suppression is required.

3.4.1 Stripping and offline cuts

The variables used in the stripping and offline selection include:

- the *impact parameter (IP)* χ^2 of a track or particle candidate with respect to PV. The impact parameter is the perpendicular distance from the PV to the momentum vector of the track or candidate. The IP χ^2 is calculated as the difference between the χ^2 of the PV reconstructed with and without the track or candidate under consideration. The larger the IP χ^2 is, the more unlikely the track or candidate originates from the PV.
- the *decay vertex χ^2 per degree of freedom (d.o.f)* of a mother particle, which measures the goodness of a fit to the decay vertex. A small decay vertex χ^2/ndf means the vertex is well constrained.
- the *PV constrained DecayTreeFitter (DTF)^[123] vertex χ^2 per d.o.f* of a mother particle, which requires the mother particle originates from the PV. The DecayTreeFitter is a technology to fit the decay chain from upstream to downstream, which has the advantage of propagating the information from a mother particle to the daughters.
- the *track χ^2/ndf* , which indicates the quality of the track fit. This variable can be used to remove poorly-reconstructed tracks.
- the *flight distance χ^2* , which is calculated for a candidate as the difference between the PV fit χ^2 with and without the tracks from the its reconstructed decay vertex added to the PV. The FD χ^2 is large when the candidate has a long lifetime, since they decay away from PV and the tracks from its reconstructed decay vertex do not form a good vertex with the PV tracks.

- the *cosine of the decay angle with respect to the PV, or DIRA*, which is defined as the cosine of the angle between the reconstructed momentum and the vector between the PV and the reconstructed decay point. If a decay point is correctly reconstructed, the value should be very close to 1. If the particle is not from PV or it only travels a very limited distance from the PV, the DIRA could deviate from 1.
- the *maximum distance of the closest approach between all possible pairs of particles, or MAXDOCA*. It is a measure of how well these tracks are constrained to a common point. If these tracks come from the same vertex, MAXDOCA should not be too large.
- the *z component difference between the decay vertex of Ξ_{cc}^+ and Λ_c^+* , which requires Λ_c^+ decays downstream of Ξ_{cc}^+ to suppress Λ_c^+ from other sources.
- the *Delta-Log-Likelihood, or DLL*, constructed from the PID log-likelihood, which discriminates between different particle hypotheses. As an example, a cut of $DLL(K - \pi) > 0$ means the track is more consistent to be a K than a π .
- the *transverse momentum, p_T* , is the component of the momentum of the candidate in the plane which is perpendicular to the direction of the proton beams. Large phase space usually implies large daughters' p_T .

The preselection criteria and the signal mode and control mode are listed in Table 3.1. For the Λ_c^+ control mode the same cuts as for the selection of the Λ_c^+ in Ξ_{cc}^+ are used, except that the cosine of the decay angle (DIRA) to the PV of Λ_c^+ is required to be > 0.999 . Note there is a prescale factor of 0.05 for the control Λ_c^+ , which means the control Λ_c^+ selection criteria is only processed on 5% of the total data; other data will be discarded.

3.4.2 Cut-based offline selection

After the stripping selection, Ξ_{cc}^+ candidates are refitted with DecayTreeFitter with the Ξ_{cc}^+ constrained to originate from the PV. The χ^2 of the fit is required to be smaller than 50 to suppress the combinatorics background. Besides, the IP χ^2 of Ξ_{cc}^+ is required to be smaller than 20. Other selections are more stringent PID cuts on the final state tracks. The offline selections are summarised in Table 3.3.

表 3.1 Preselection criteria for the Ξ_{cc}^+ decay.

Ξ_{cc}^+	DIRA Vertex fit $\chi^2/ndof$ Flight distance $\chi^2/ndof$ p_T Invariant mass DTF PV fit χ^2 IP χ^2	> 0.999 < 10 > 16 $> 2000 \text{ MeV}/c$ $< 4500 \text{ MeV}/c^2$ < 50 < 20
Tracks from Ξ_{cc}^+	p p_T Track $\chi^2/ndof$ Kaon PID DLL($K - \pi$) Pion PID DLL($\pi - K$) IP χ^2	$> 2000 \text{ MeV}/c$ $> 250 \text{ MeV}/c$ < 4 > 10 > 5 > 4
Λ_c^+	DIRA Vertex fit $\chi^2/ndof$ Flight distance $\chi^2/ndof$ p_T MAXDOCA Invariant mass At least one daughter with IP χ^2 z separation between Ξ_{cc}^+ and Λ_c^+ vertices	> 0.98 < 10 > 36 $> 1000 \text{ MeV}/c$ $< 0.5 \text{ m}$ $2185 < M < 2385 \text{ MeV}/c^2$ > 30 $> 0.01 \text{ mm}$
Tracks from Λ_c^+	p p_T Track $\chi^2/ndof$ Proton PID DLL($p - \pi$) Kaon PID DLL($K - \pi$) Pion PID DLL($\pi - K$) IP χ^2	$> 2000 \text{ MeV}/c$ $> 250 \text{ MeV}/c$ < 4 > 10 > 10 > 5 > 4

表 3.2 Preselection criteria for the control Λ_c^+ decay.

Λ_c^+	DIRA	> 0.999
	Vertex fit $\chi^2/ndof$	< 10
	Flight distance $\chi^2/ndof$	> 36
	p_T	$> 1000 \text{ MeV}/c$
	MAXDOCA	$< 0.5 \text{ m}$
	Invariant mass	$2185 < M < 2385 \text{ MeV}/c^2$
	At least one daughter with IP χ^2	> 30
	z separation between Ξ_{cc}^+ and Λ_c^+ vertices	$> 0.01 \text{ mm}$
Tracks from Λ_c^+	p	$> 2000 \text{ MeV}/c$
	p_T	$> 250 \text{ MeV}/c$
	Track $\chi^2/ndof$	< 4
	Proton PID DLL($p - \pi$)	> 10
	Kaon PID DLL($K - \pi$)	> 10
	Pion PID DLL($\pi - K$)	> 5
	IP χ^2	> 4

 表 3.3 Offline cuts applied after the stripping. The same DLL cuts are used for the daughter tracks of the Ξ_{cc} and the Λ_c^+ .

Particle	Variable	Cut value
Ξ_{cc}^+	PV Fit χ^2	< 50
	Impact Parameter χ^2	< 20
K^-	DLL($K - \pi$)	> 10
π^-	DLL($\pi - K$)	> 5
p^+	DLL($p - \pi$)	> 10

3.4.3 Multivariate analysis

After the rectangular cuts, the background level is still overwhelming, as illustrated in Figure 3.2. To suppress background as much as possible, an artificial neural network (ANN) is trained to squeeze every bit of information out of the pp collision data.

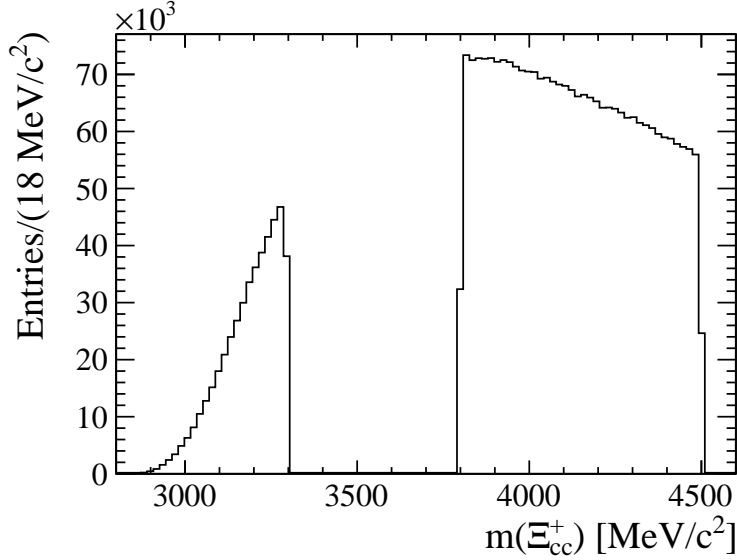


图 3.2 The invariant mass distribution of the Ξ_{cc}^+ candidates after all the rectangular cuts applied. The signal region is blinded.

3.4.3.1 Neural Network

The neural network is a sophisticated and powerful tool for statistical classification and prediction. It is a mathematical model based on the neural structure of the brain^[124]. Natural neurons receive signals through synapses. When the signals surpass a certain threshold, the neuron is activated and emits a signal through the axon. The signal might be sent to another synapse, and might activate other neurons. The modelling of ANN follows basically the same but much more simplified approach. The basic elements in an ANN are nodes, which receive inputs from other nodes (like the strength of the signals). The sum of weights is passed to an activation function to determine the activation status of the node. For the sake of simplicity, the nodes are usually organized in a structure called multilayer perceptron – nodes are divided into several layers and only the nodes in the adjacent layers are connected. To use the ANN for selection, the weights should be computed; this is called training. The ANNs used in HEP community are supervised

ANN, which infers a function from with categorised data, *i.e.* the category of the input, either signal or background, is labelled^[125]. If the input training sample do not have enough statistics to determine all the weights precisely, the neural network may suffer from statistical fluctuation and describes random errors of the training sample instead of underlying relationship, therefore the efficacy of the network is biased. This is called overtraining. To evaluate the efficacy correctly, the ANN is applied to a statistical independent sample. The multivariate selection used for our selection is implemented with the MLP neural network from the TMVA package^[126].

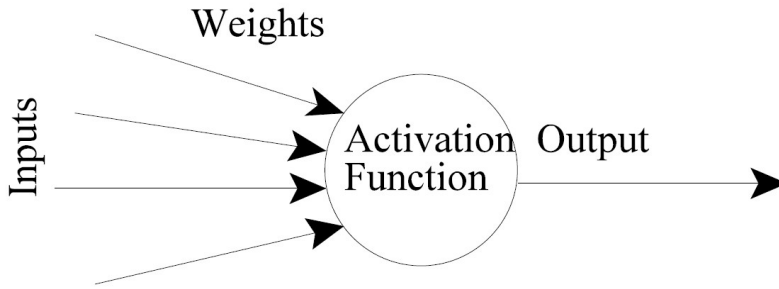


图 3.3 The modelling of an artificial neural network.

The input nodes, or variables, are chosen so as to depend only weakly on the Ξ_{cc}^+ lifetime. The signal sample is the truth-matched Ξ_{cc}^+ Monte Carlo events with the same cuts as data. The truth-matching is done with the background category tool^[127]. Since the trigger efficiency is low and the MC statistics is limited, the neural network training and the cut optimisation are done before applying trigger requirement. This allows us to have enough events for training. The signal sample contains 3690 events, half for training and another half for testing. The background sample is obtained from Ξ_{cc}^+ mass sidebands. Since the mass range of $[3300, 3800]$ MeV/c^2 is blind, the lower sideband is chosen to be $[3100, 3300]$ MeV/c^2 , and the upper sideband is $[3800, 4000]$ MeV/c^2 . The background sample has 5000 events, with all the cuts applied, also half for training and another half for testing. For the purposes of the MLP training and testing, a Λ_c^+ mass window of ± 40 MeV/c^2 was applied. This background sample was not excluded from the main analysis, because there is no indication of overtraining, and the training sample is small compared to the total background (about 3.5% of candidates).

The input variables used for neural network training are listed in the following:

- Ξ_{cc}^+ MAXDOCA

- Ξ_{cc}^+ IP χ^2
- Ξ_{cc}^+ decay vertex χ^2
- The smallest p_T of the three Ξ_{cc}^+ daughters
- Ξ_{cc}^+ DecayTreeFitter χ^2 with a PV constraint
- Λ_c^+ decay vertex χ^2
- Λ_c^+ IP χ^2
- Λ_c^+ flight distance χ^2
- Λ_c^+ MAXDOCA

The distribution of these input variables are shown in Fig. 3.4. The blue lines are the signal Monte Carlo, and the red shaded are the sideband background.

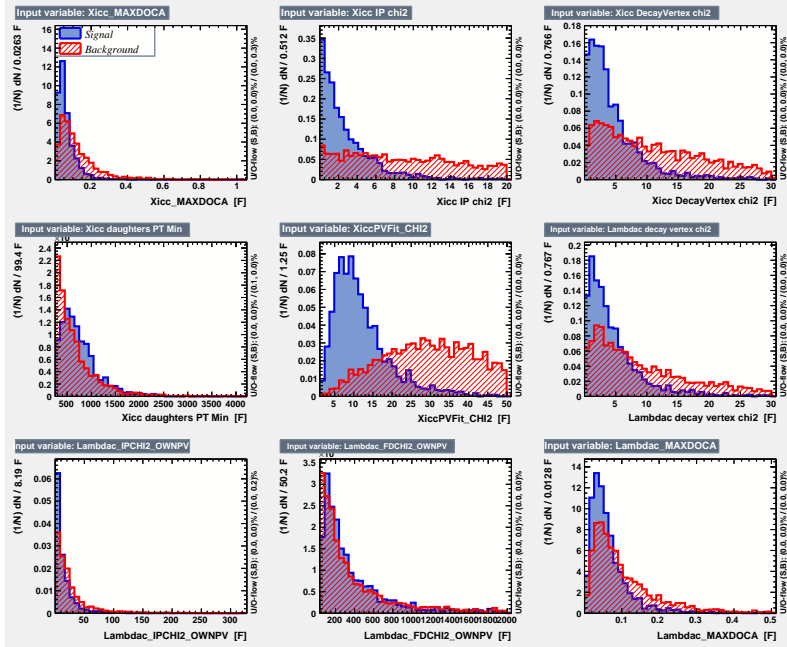


图 3.4 The distribution of input variables for the MLP. The blue lines are the signal Monte Carlo, and the red shaded are the sideband background.

The MLP response for signal (blue) and background (red) are shown in Figure 3.5. The test and training samples agree well for both signal and background, indicating there is no overtraining. The corresponding ROC curve is displayed in Figure 3.6. The optimisation cut is determined by maximising the expected significance $s/\sqrt{s+b}$, where s and b are the expected signal and background counts in the signal region. For the purposes of this optimisation, the expected signal s is estimated based on the theoretical cross-section, the luminosity and the efficiency from MC, and the expected background

is estimated with the extrapolation from $m(\Xi_{cc}^+)$ sidebands. The optimal cut is chosen to be $\text{MLP} > 0.8$. The efficiency of this cut relative to the MLP input sample is found to be $\varepsilon_{\text{sig}}^{\text{mlp}} = 55.7\%$. The estimated retention on combinatoric background in the Λ_c^+ signal region is 4.2%.

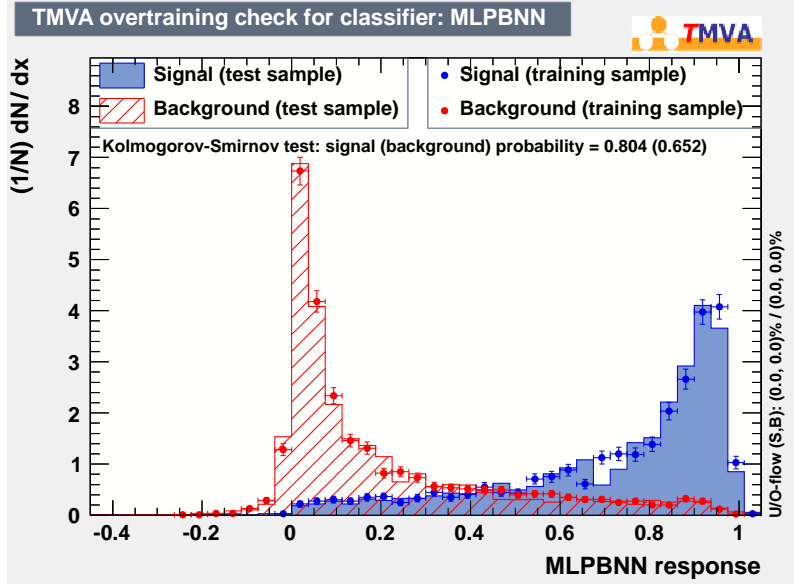


图 3.5 The MLP response for signal (blue) and background (red).

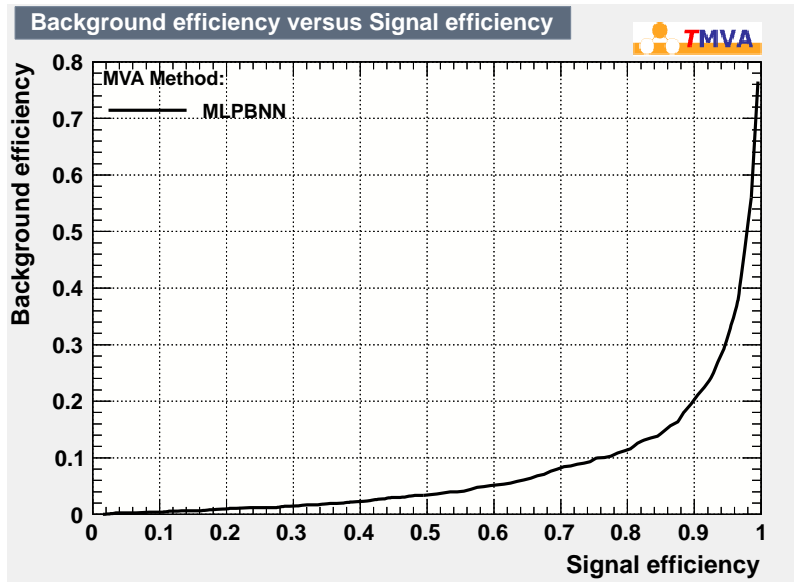


图 3.6 The efficiency of the signal vs. the retention rate of background.

表 3.4 L0Hadron selection cuts

Variable	Cut value
SPD hits	< 600
E_T in HCAL	> 3500 MeV/c

3.4.4 Trigger requirements

As mentioned in Section 2.3, only the events met one of the trigger lines are recorded. The events don't need to be trigger by the signal,

while for MC all the events reconstructed and passing the selections are recorded. The trigger requirements are imposed after the MLP cut. To minimise the systematic uncertainty, the trigger lines were chosen so that the same triggers could be used for the signal and control modes. Therefore the trigger requirements are then chosen to be a TOS chain on Λ_c^+ . since we do not know the efficiency of TIS triggers for Ξ_{cc} events and can't assume that they will be the same as for Λ_c^+ since the associated production may be very different

- L0: L0Hadron TOS on a Λ_c^+ daughter track
- HLT1: Hlt1TrackAllL0 TOS on a Λ_c^+ daughter track
- HLT2: Hlt2CharmHadLambdaC2KPPi TOS on the Λ_c^+

The selection cuts in the trigger lines are briefly introduced below. Note all the quantities used are from online, and they could be different from that of offline.

3.4.4.1 L0 trigger

In the TCK considered, the L0Hadron trigger line consists of two cuts below.

3.4.4.2 HLT1 trigger

The HLT1TrackAllL0 trigger line contains four steps to select signal and reject background efficiently. First it applies global event cuts to remove the events which would consume too much time to process. The requirements are listed here.

表 3.6 HLT1TrackAllL0 selection cuts: Step 2

Variable	Cut value
$ n_{\text{exp}} - n_{\text{obs}} $ hits in Velo	< 3
Velo hits	> 9
IP to any PV	$< 100\text{m m}$

表 3.7 HLT1TrackAllL0 selection cuts: Step 3

Variable	Cut value
hits in tracking system	> 16
p_T	$> 1700\text{ MeV}$
p	$> 10000\text{ MeV}$

表 3.5 HLT1TrackAllL0 selection cuts: Step 1

Variable	Cut value
OT hits	< 15000
IT hits	< 3000
Velo hits	< 10000

Then the primary vertices and VELO tracks are reconstructed, and several cuts are applied on the VELO tracks.

At the third step, the VELO tracks selected are then fully reconstructed. These tracks are selected further: The survived tracks are then re-fitted using a BiDirectional Kalman filter and asked to pass these cuts:

At least one of the tracks from Λ_c^+ should satisfy these requirements.

表 3.8 HLT1TrackAllL0 selection cuts: Step 4

Variable	Cut value
track $\chi^2/ndof$	< 2
min IP χ^2 to all PV	> 16

3.4.4.3 HLT2 trigger

The L0 and HLT1 lines are standard, but the HLT2 line is dedicated to charm baryon studies and is described here. The cuts in the trigger line are reported in Table 3.9. An unusual feature of this trigger is that it uses RICH PID information. Note this line was only introduced into the online trigger system in July 2011. So the TOS requirement means implicitly that only data taken after this time are used in the analysis.

表 3.9 HLT2 trigger criteria of criteria of Hlt2CharmHadLambdaC2KPPi.

Cut type	Variable	Cut value
Combination Cut	Invariant mass from sum of four-momenta of daughters	$2150 \text{ MeV}/c^2 < AM < 2430 \text{ MeV}/c^2$
Mother Cuts	p_T	$> 2500 \text{ MeV}/c$
	cosine of decay angle w.r.t PV	> 0.99985
	Flight distance $\chi^2/ndof$	> 16
	Vertex Fit $\chi^2/ndof$	< 15
All daughters	Track $\chi^2/ndof$	< 3
	p_T	$> 500 \text{ MeV}/c$
	IP χ^2 to own PV	> 9
Extra cuts for Proton	$ p $	$> 10 \text{ GeV}/c$
	PID DLL($p - \pi$)	> 0
	PID DLL($p - K$)	> 0

3.5 Efficiency ratio determination

With the selection criteria stated above, the efficiency of the signal mode can be decomposed as follows:

$$\epsilon_{\text{sig}} = \epsilon_{\text{sig}}^{\text{acc}} \epsilon_{\text{sig}}^{\text{sel|acc}} \epsilon_{\text{sig}}^{\text{PID|sel}} \epsilon_{\text{sig}}^{\text{mlp|PID}} \epsilon_{\text{sig}}^{\text{trigger|mlp}}, \quad (3-5)$$

where the pieces are: acceptance (acc), stripping and cut-based offline selection (sel), further offline PID cuts (PID), MLP multivariate selection (mlp), and trigger (trigger). Because of the inaccurate description of RICH information in Monte Carlo, PID cut efficiency should be found by data-driven method, instead of evaluated from Monte Carlo, like for other cuts in stripping and cut-based offline cuts. PID cuts are therefore isolated from main selection efficiency. The | symbol means “given” (e.g. $\epsilon_{\text{sig}}^{\text{sel|acc}}$ is the efficiency

to pass the selection given that a candidate is in the acceptance) and all selections are cumulative. The corresponding decomposition for the control mode is:

$$\varepsilon_{\text{con}} = \varepsilon_{\text{con}}^{\text{acc}} \varepsilon_{\text{con}}^{\text{sel|acc}} \varepsilon_{\text{con}}^{\text{PID|sel}} \varepsilon_{\text{con}}^{\text{trigger|sel}}, \quad (3-6)$$

with no multivariate selection. We can therefore express the production ratio R defined in eq. 3-3 as:

$$R = \frac{\varepsilon_{\text{con}}^{\text{acc}}}{\varepsilon_{\text{sig}}^{\text{acc}}} \frac{\varepsilon_{\text{con}}^{\text{sel|acc}}}{\varepsilon_{\text{sig}}^{\text{sel|acc}}} \frac{\varepsilon_{\text{con}}^{\text{PID|sel}}}{\varepsilon_{\text{sig}}^{\text{PID|sel}}} \frac{1}{\varepsilon_{\text{sig}}^{\text{mlp|PID}}} \frac{\varepsilon_{\text{con}}^{\text{trigger|PID}}}{\varepsilon_{\text{sig}}^{\text{trigger|mlp}}} \frac{N_{\text{sig}}}{N_{\text{con}}} = \alpha N_{\text{sig}} \quad (3-7)$$

The whole efficiency is decomposed into five steps: the acceptance efficiency, the stripping and offline efficiency, the PID efficiency, the MLP efficiency and the trigger efficiency. In the following sections, the ratio of each efficiency of the Λ_c^+ control mode and the Ξ_{cc} signal mode will be determined in order to calculate α as defined in Eq. 3-7.

3.5.1 Ratio of acceptance efficiencies

The LHCb detector only covers a small solid angle (10 to 300 mrad in the horizontal plane and 10 to 250 mrad in the vertical plane). But technically the acceptance efficiency is defined as the fraction of the events that have all the final-state particles in the solid cone of $10 < \theta < 400$ mrad, where θ is the angle between the momentum of the final track and z axis. However, it should be noted that the acceptance cut here is only a tool to prevent wasting computing power on events which can never be reconstructed. This simple angular cut does not exactly correspond to the LHCb acceptance exactly. But the overall efficiency is not overestimated, as the real effect of the acceptance will be accounted for by full simulation. The acceptance efficiency is computed with a generator-level Gauss simulation. The results are listed in the Table 3.10, and the ratio of acceptance efficiencies is measured to be 1.209 ± 0.009 .

表 3.10 The acceptance efficiency, evaluated with generator-level MC.

decay mode	MagUp	MagDown	Average
signal mode	0.17561 ± 0.00113	0.17785 ± 0.00114	0.17672 ± 0.00080
control mode	0.21287 ± 0.00190	0.21460 ± 0.00189	0.21374 ± 0.00134

3.5.2 Ratio of stripping and offline efficiency

The stripping and offline efficiency is figured out by MC. Note the PID related cuts are not included here, since they are not well modeled by MC. They're considered in the next subsection. For signal mode, 7187 of 2.26×10^6 Ξ_{cc}^+ MC events are left; for control mode, about 2.0×10^6 Λ_c^+ MC events produced and 2.6×10^4 events left. The stripping of MC is run in Flagging Mode, so the prescale factor of the control mode is not considered here. The ratio of (stripping and non-PID offline cut) efficiencies between control and signal modes is found to be 3.838 ± 0.051 .

表 3.11 The selection efficiency, including the stripping and non-PID offline selection, evaluated with full MC.

decay mode	# of events generated	# of events selected	selection efficiency
signal mode	2.26×10^6	7187	$(3.1766 \pm 0.0374) \times 10^{-3}$
control mode	2.0×10^6	26×10^3	$(1.2192 \pm 0.0077) \times 10^{-2}$

3.5.2.1 Tracking efficiency corrections

The tracking efficiency is included implicitly in the stripping efficiency, since only signal candidates which have all the final-state tracks reconstructed could pass the stripping selection. However, there are known data/MC discrepancies in the tracking efficiency which need to be corrected for. There is a standard procedure described below to correct for these differences. There will then be an additional systematic uncertainty due to limitations in the correction procedure, also mentioned below.

The LHCb tracking group have compared the tracking efficiency of data and MC, and calculate the data/MC efficiency ratio for individual tracks as a function of momentum and rapidity^[89]. However, before we get to that correction there is another effect we need to consider: as well as the track kinematics, the efficiency depends on the event track multiplicity. This is known not to match between data and MC, so we need to reweight the track multiplicity in the MC to match that expected in data. For the Λ_c^+ control mode we simply take the track multiplicity from our stripping line. However, we have a problem for the signal mode: we don't have a sample of data Ξ_{cc}^+ that we can use for the reweighting! Instead, we have to choose a suitable proxy. There are a few possibilities, none an exact match. We use B_s events, on the grounds that this also requires producing two non-

light quark-antiquark pairs ($b\bar{b}$ and $s\bar{s}$ instead of two $c\bar{c}$ pairs) The specific control sample used is a set of $B_s \rightarrow J\psi\phi$ decays in the StrippingBetaSBs2JpsiPhiPrescaledLine Stripping17 line. The sPlot^[2] method is used to extract the multiplicity distribution of B_s . For both the Λ_c^+ and B_s samples, we find that an empirical function consisting of a Landau multiplied by a Gaussian describes the distribution adequately. The fitted distributions are shown in Fig. 3.8 and ??.

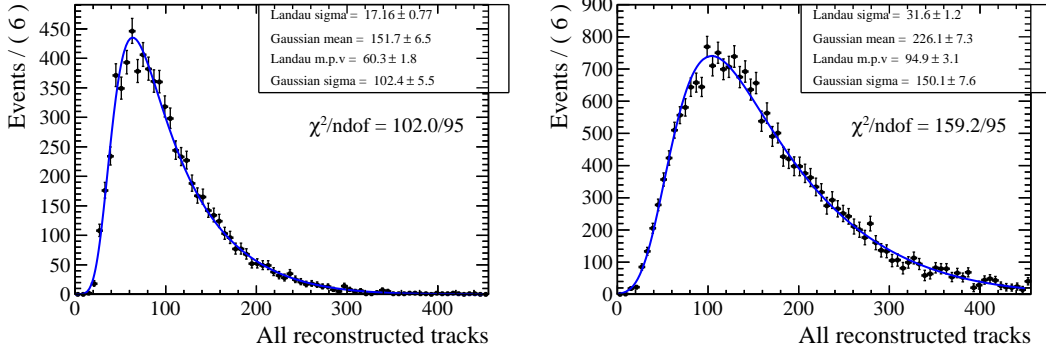


图 3.7 The best track multiplicity distribution for Ξ_{cc}^+ MC(left) and $B_s \rightarrow J/\psi\phi$ (right).

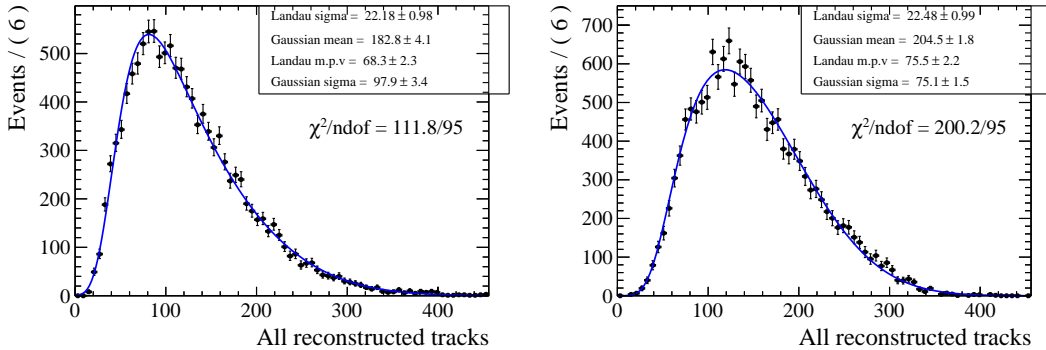


图 3.8 The best track multiplicity distribution for Λ_c^+ MC(left) and Λ_c^+ data(right)

Using the tag-and-probe method^[2] on $J/\psi \rightarrow \mu^+\mu^-$ sample, the tracking efficiency ratio between data/MC is evaluated as a function of momentum and pseudo-rapidity of the track, as is shown in Fig ??

We follow the method developed by B&Q working group^[128,129] to apply this correction. A toy MC method is used. For each toy experiment, the central values in the table as smeared according to their errors and then fixed as the true ratio values for that toy. Then for each daughter track of each candidate in the signal MC samples we can

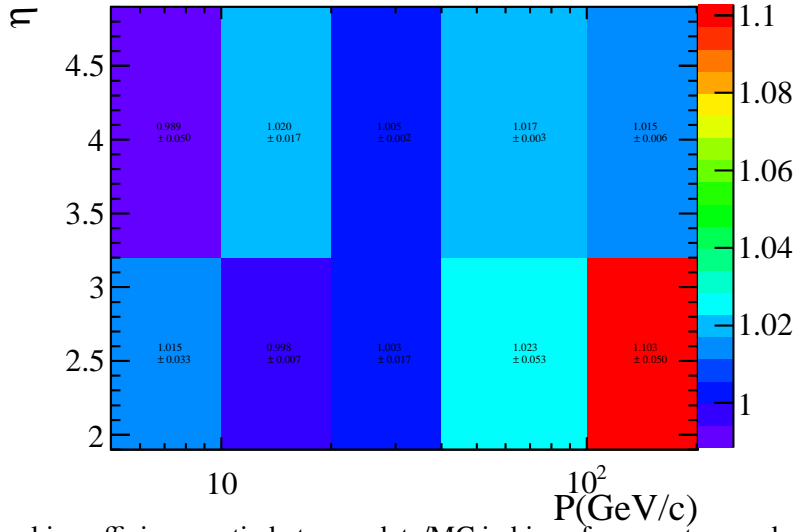


图 3.9 The tracking efficiency ratio between data/MC in bins of momentum and pseudo-rapidity of the track

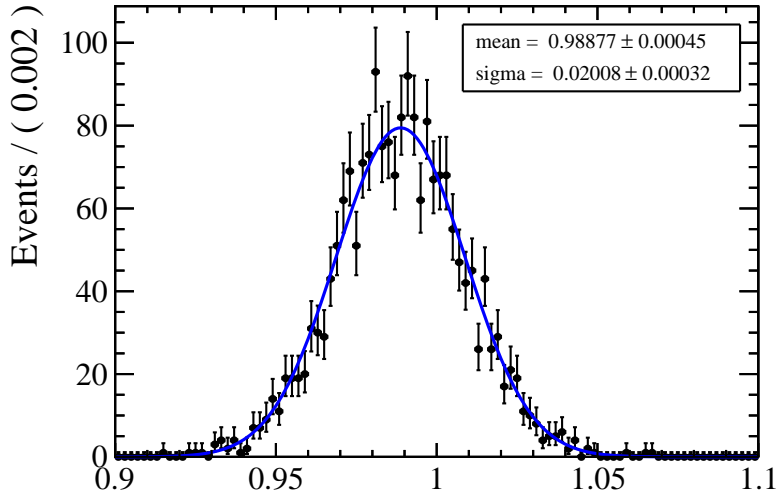


图 3.10 Fit the efficiency ratio from toy MC.

calculate the correction from the table. Combining the per-daughter corrections gives us a per-candidate correction, and we then average across the candidates (multiplicity-weighted as described above) to give us a per-toy correction for Ξ_{cc}^+ and for Λ_c^+ . From these we obtain a per-toy correction to $\frac{\mathcal{E}_{\text{con}}^{\text{sellacc}}}{\mathcal{E}_{\text{sig}}^{\text{sellacc}}}$. By performing many toy experiments we obtain a distribution of these correction ratios, shown in Fig. 3.10. Fitting this distribution we obtain a mean correction of 0.989 ± 0.020 .

Note that in this method the kinematic correlations among daughter tracks have been neglected—we'll assign a systematic uncertainty for this in Sec. ??.

Finally, we note that the efficiency tables described above were obtained with a

muon sample, while our modes involve hadronic final states which will suffer additional material interactions. A systematic uncertainty will be assigned for this in Sec. ??.

3.5.3 Ratio of PID cut efficiencies

It is known that the distribution of PID variables are different between data and MC, because several 2nd-order effects are not considered in simulation and the performance of RICH varies with running condition. The LHCb PID working group provides the PID-Calib package to solve this problem. It is assumed that the PID efficiency of a track depend on its momentum and pseudo-rapidity as well as the best track multiplicity of the event. Tracks from standard calibration samples selected without PID cuts can then be reweighted to match the distributions expected for tracks produced in Ξ_{cc} decays according to signal MC. The efficiency of our PID cuts can then be obtained by applying them to the weighted, background-subtracted calibration samples. The calibration sample used for kaons and pions is $D^{*+} \rightarrow D^0\pi_s$, $D^0 \rightarrow K^-\pi^+$, and that used for protons is $\Lambda \rightarrow p\pi$.

3.5.3.1 The calibration procedure

To reweight the calibration samples we need the kinematic distribution for the data before PID cuts. However, the standard stripping applied to signal MC includes PID cuts (and so could have a biased distribution). Instead, we rerun the stripping with the PID cuts disabled, and then apply the cut-based offline selection (again without PID cuts).

The multiplicity of Ξ_{cc}^+ is possibly seriously under-estimate in MC. Since the PID efficiency is known to be depend on the track multiplicity, this difference must be taken account in. We use a similar approach to that discussed in Sec. 3.5.2.1. The multiplicity distribution of Ξ_{cc}^+ MC is weighted to match that of $B_s \rightarrow J/\psi\phi$ data, and Λ_c^+ MC is weighted to match Λ_c^+ data.

The kinematics of the signal mode are very different from those of the calibration mode, and the statistics of the MC sample are not very large. Therefore we didn't use the default binning of these variables in the package but instead chose a binning better suited to our analysis (see Table ?? for K and π and Table ?? for p). The efficiencies obtained for the Ξ_{cc}^+ final state tracks can be found in Tables ??, ??, ??, ??, and ??. Those for the Λ_c^+ final state tracks can be found in Tables ??, ??, and ??.

表 3.12 The binning used for K and π for the PID calibration.

Variable	Binning
p [MeV]	[2000, 9300, 15600, 17675, 20000, 26000, 29650, 40000, 55000, 100000]
η	[1.5, 2.8, 3.6, 5]
multiplicity	[0, 120, 200, 400]

 表 3.13 The binning used for p for the PID calibration.

Variable	Binning
p [MeV]	[2000, 9300, 15600, 17675, 20000, 25000, 29650, 50000, 125000]
η	[1.5, 2.8, 3.6, 5]
multiplicity	[0, 120, 200, 400]

 表 3.14 The calibration of K from Λ_c^+ in Ξ_{cc}^+ MC

SubID	MagDown		MagUp	
	Run range	PIDK > 10 Efficiency	Run Runge	PIDK > 10 Efficiency
2	92821-93224	–	94261-96641	(86.43 ± 0.25)%
3	93225-97884	(87.09 ± 0.21)%	96642-100243	(86.48 ± 0.26)%
4	97885-98198	(87.65 ± 0.20)%	100244-102505	(86.17 ± 0.23)%
5	98199 -101905	(87.28 ± 0.21)%	102506-102893	(86.32 ± 0.23)%
6	101906-102378	(87.09 ± 0.21)%	102894-104263	(85.90 ± 0.36)%
7	102379-103361	(86.90 ± 0.19)%		–
8	103362-103686	(87.42 ± 0.20)%		–

 表 3.15 The calibration of p from Λ_c^+ in Ξ_{cc}^+ MC

SubID	MagDown		MagUp	
	Run range	PIDp > 10 Efficiency	Run Runge	PIDp > 10 Efficiency
2	92821-93224	–	94261-96641	(88.90 ± 0.38)%
3	93225-97884	(89.73 ± 0.40)%	96642-100243	(89.49 ± 0.74)%
4	97885-98198	(89.42 ± 0.28)%	100244-102505	(88.65 ± 0.50)%
5	98199 -101905	(89.87 ± 0.93)%	102506-102893	(88.55 ± 0.49)%
6	101906-102378	(89.42 ± 0.44)%	102894-104263	(89.05 ± 0.94)%
7	102379-103361	(90.17 ± 0.66)%		–
8	103362-103686	(88.63 ± 0.68)%		–

表 3.16 The calibration of π from Λ_c^+ in Ξ_{cc}^+ MC

SubID	MagDown		MagUp	
	Run range	PIDK < -5 Efficiency	Run Runge	PIDK < -5 Efficiency
2	92821-93224	–	94261-96641	(70.67 ± 0.21)%
3	93225-97884	(69.57 ± 0.18)%	96642-100243	(67.19 ± 0.22)%
4	97885-98198	(66.62 ± 0.19)%	100244-102505	(65.62 ± 0.22)%
5	98199 -101905	(68.09 ± 0.19)%	102506-102893	(67.27 ± 0.22)%
6	101906-102378	(67.85 ± 0.18)%	102894-104263	(65.81 ± 0.36)%
7	102379-103361	(67.84 ± 0.18)%		–
8	103362-103686	(65.50 ± 0.20)%		–

 表 3.17 The calibration of K from Ξ_{cc}^+ in Ξ_{cc}^+ MC

SubID	MagDown		MagUp	
	Run range	PIDK > 10 Efficiency	Run Runge	PIDK > 10 Efficiency
2	92821-93224	–	94261-96641	(87.02 ± 0.26)%
3	93225-97884	(86.90 ± 0.23)%	96642-100243	(87.06 ± 0.26)%
4	97885-98198	(87.63 ± 0.22)%	100244-102505	(86.89 ± 0.24)%
5	98199 -101905	(87.21 ± 0.23)%	102506-102893	(86.94 ± 0.23)%
6	101906-102378	(86.99 ± 0.23)%	102894-104263	(86.56 ± 0.37)%
7	102379-103361	(86.79 ± 0.21)%		–
8	103362-103686	(87.42 ± 0.22)%		–

 表 3.18 The calibration of π from Ξ_{cc}^+ in Ξ_{cc}^+ MC

SubID	MagDown		MagUp	
	Run range	PIDK < -5 Efficiency	Run Runge	PIDK < -5 Efficiency
2	92821-93224	–	94261-96641	(69.50 ± 0.20)%
3	93225-97884	(67.96 ± 0.21)%	96642-100243	(65.76 ± 0.21)%
4	97885-98198	(64.86 ± 0.22)%	100244-102505	(64.21 ± 0.21)%
5	98199 -101905	(66.40 ± 0.22)%	102506-102893	(65.98 ± 0.21)%
6	101906-102378	(66.22 ± 0.22)%	102894-104263	(64.34 ± 0.34)%
7	102379-103361	(66.18 ± 0.22)%		–
8	103362-103686	(63.71 ± 0.23)%		–

表 3.19 The calibration of K from Λ_c^+ in Λ_c^+ MC

SubID	MagDown		MagUp	
	Run range	PIDK > 10 Efficiency	Run Runge	PIDK > 10 Efficiency
2	92821-93224	–	94261-96641	(86.10 ± 0.18)%
3	93225-97884	(85.86 ± 0.17)%	96642-100243	(85.97 ± 0.19)%
4	97885-98198	(86.38 ± 0.17)%	100244-102505	(85.84 ± 0.17)%
5	98199 -101905	(86.14 ± 0.18)%	102506-102893	(85.79 ± 0.17)%
6	101906-102378	(85.77 ± 0.18)%	102894-104263	(85.62 ± 0.27)%
7	102379-103361	(85.64 ± 0.16)%		–
8	103362-103686	(86.12 ± 0.17)%		–

 表 3.20 The calibration of p from Λ_c^+ in Λ_c^+ MC

SubID	MagDown		MagUp	
	Run range	PIDp > 10 Efficiency	Run Runge	PIDp > 10 Efficiency
2	92821-93224	–	94261-96641	(88.92 ± 0.54)%
3	93225-97884	(89.56 ± 0.60)%	96642-100243	(89.42 ± 0.89)%
4	97885-98198	(89.03 ± 0.49)%	100244-102505	(88.65 ± 0.67)%
5	98199 -101905	(94.03 ± 1.22)%	102506-102893	(88.39 ± 0.59)%
6	101906-102378	(89.38 ± 0.70)%	102894-104263	(91.50 ± 1.21)%
7	102379-103361	(90.37 ± 1.17)%		–
8	103362-103686	(88.76 ± 0.71)%		–

 表 3.21 The calibration of π from Λ_c^+ in Λ_c^+ MC

SubID	MagDown		MagUp	
	Run range	PIDK < -5 Efficiency	Run Runge	PIDK < -5 Efficiency
2	92821-93224	–	94261-96641	(71.61 ± 0.18)%
3	93225-97884	(69.55 ± 0.18)%	96642-100243	(68.26 ± 0.19)%
4	97885-98198	(66.67 ± 0.18)%	100244-102505	(66.74 ± 0.18)%
5	98199 -101905	(68.09 ± 0.18)%	102506-102893	(68.27 ± 0.19)%
6	101906-102378	(67.82 ± 0.18)%	102894-104263	(66.91 ± 0.31)%
7	102379-103361	(67.82 ± 0.18)%		–
8	103362-103686	(65.55 ± 0.20)%		–

表 3.22 The lumi of each subsample

SubID	MagDown		MagUp	
	Run range	Lumi(p b ⁻¹)	Run Runge	Lumi(p b ⁻¹)
2	92821-93224	–	94261 -96641	33.02 ± 0.14
3	93225-97884	57.19 ± 0.19	96642 -100243	67.39 ± 0.21
4	97885-98198	68.23 ± 0.21	100244 -102505	69.76 ± 0.22
5	98199 -101905	68.94 ± 0.21	102506 -102893	67.94 ± 0.21
6	101906-102378	69.59 ± 0.21	102894-104263	25.26 ± 0.12
7	102379-103361	68.97 ± 0.21		
8	103362-103686	57.59 ± 0.18		

3.5.3.2 The luminosity of each run range

To account for the variation in RICH performance over time, the calibration samples are split into several subsamples according to changes in the data-taking conditions. The PID cut efficiencies are different between these samples. To minimize systematic effects, the efficiency ratio between control and signal modes is calculated for each run range seperately, then combined in a lumi-weighted average. Assuming the luminosity of sample i is L_i , and the efficiency ratio is r_i , then the average efficiency ratio r is

$$r = \frac{\sum_i L_i r_i}{\sum_i L_i} \quad (3-8)$$

The luminosity of each sample is listed in Table 3.22 and the efficiency ratio in each run range is given in Table 3.23.

表 3.23 The efficiency of each subsample

SubID	MagDown		MagUp	
	Run range	Efficiency ratio	Run Runge	Efficiency ratio
2	92821-93224	–	94261 -96641	1.670 ± 0.017
3	93225-97884	1.666 ± 0.017	96642 -100243	1.763 ± 0.026
4	97885-98198	1.727 ± 0.016	100244 -102505	1.816 ± 0.021
5	98199 -101905	1.783 ± 0.032	102506 -102893	1.755 ± 0.019
6	101906-102378	1.708 ± 0.019	102894-104263	1.870 ± 0.038
7	102379-103361	1.719 ± 0.028		
8	103362-103686	1.772 ± 0.023		

3.5.3.3 Ratio of PID cuts efficiencies

With all the above factors taken into account, the ratio of PID cut efficiencies is calculated to be 1.748 ± 0.034 .

3.5.4 MVA cut efficiency

To train and test the MVA we used two samples of signal MC. The test sample is used to evaluate the MVA cut efficiency. For the chosen MVA cut of > 0.8 (see Sec. ??), the efficiency is $\epsilon_{\text{sig}}^{\text{mva}} = 0.557 \pm 0.012$.

Note the MVA cut is only applied to the signal mode, not to the control mode. So taking the MVA efficiency for the control mode to be 1 by construction, the ratio of efficiencies is $(1/\epsilon_{\text{sig}}^{\text{mva}}) = 1.795 \pm 0.039$.

3.5.5 Trigger efficiency

The trigger lines chosen for this analysis are

- L0: L0Hadron TOS for Λ_c^+
- Hlt1: Hlt1TrackAllL0 TOS for Λ_c^+
- Hlt2: Hlt2CharmHadLambdaC2KPPi TOS for Λ_c^+

3.5.5.1 L0 efficiency

The MC doesn't represent the L0 efficiency well for a number of reasons, such as that the L0Calo efficiency is not constant over time due to HCAL and ECAL ageing and recalibration ^[130]. It is very difficult to take this account in MC since the variations for different zones are not the same. The Calo working group provides several trigger efficiency tables in bins of p_T for different types of track. These efficiencies are calculated using tracks from the PIDCalib sample with the TISTOS method^[131]. We have the same problem as for the PID calibration, namely that the kinematic distribution of protons in our Ξ_{cc} signal sample doesn't match that in the calibration sample very well: protons from inclusive Λ decays to long tracks are very soft, and hence events with $p_T > 4600$ MeV are very rare, but the signal sample has many events in this region and the trigger efficiency is a strong function of p_T . To get a more accurate result, the control sample ($\Lambda_c^+ \rightarrow pK^-\pi^+$) is used to evaluate the L0 trigger efficiency in the high p_T region, using the same method described below (following the documentation^[132,133] linked from the L0Calo twiki page^[131]).

The trigger efficiency is calculated using these efficiency tables with a toy MC method. For each toy MC experiment, the efficiency for each track is smeared according to the error in the corresponding p_T bin, then the trigger efficiency for this event is

$$\varepsilon = 1 - (1 - \varepsilon_p)(1 - \varepsilon_K)(1 - \varepsilon_\pi) \quad (3-9)$$

The individual track L0 efficiencies are plotted in Fig. 3.11, 3.12, and 3.13. After many toy experiments, the distribution of the efficiency could be drawn (Fig. 3.14) and the efficiency and the error can be extracted from a fit. Using a standard Gaussian to fit the distribution, the ratio of L0 efficiencies between control and signal modes is found to be 1.451 ± 0.002 .

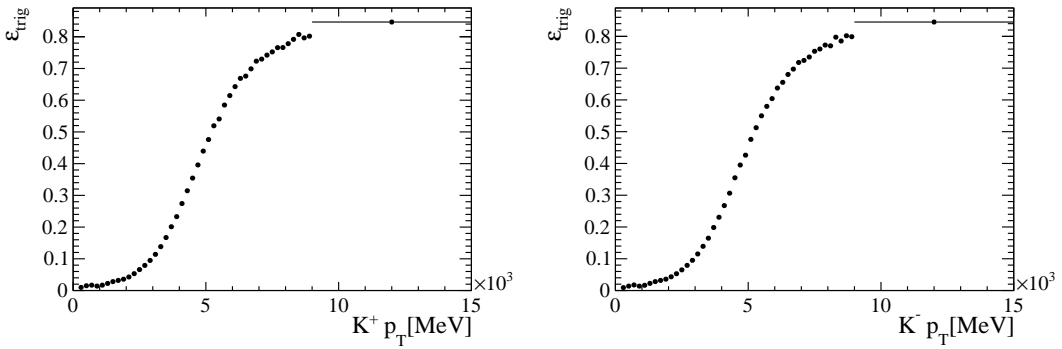


图 3.11 Trigger efficiency in bins of p_T for (a) K^+ and (b) K^-

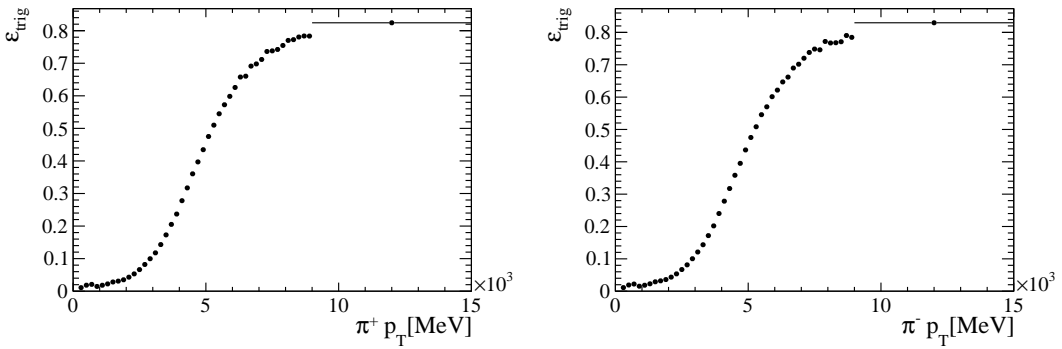


图 3.12 Trigger efficiency in bins of p_T for (a) π^+ and (b) π^-

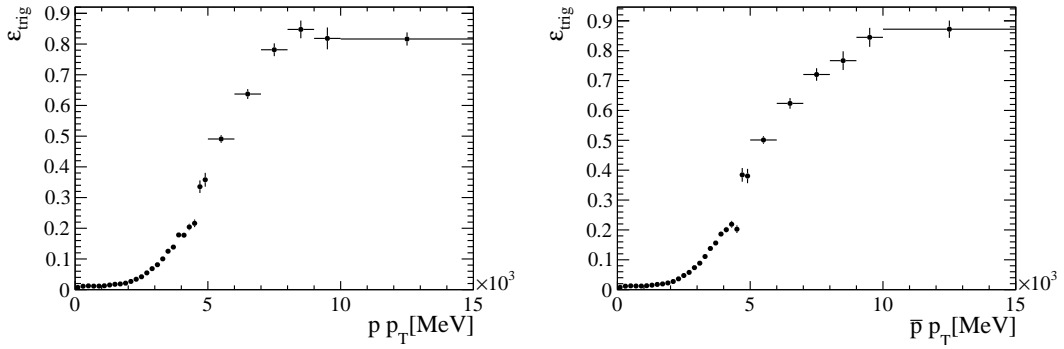
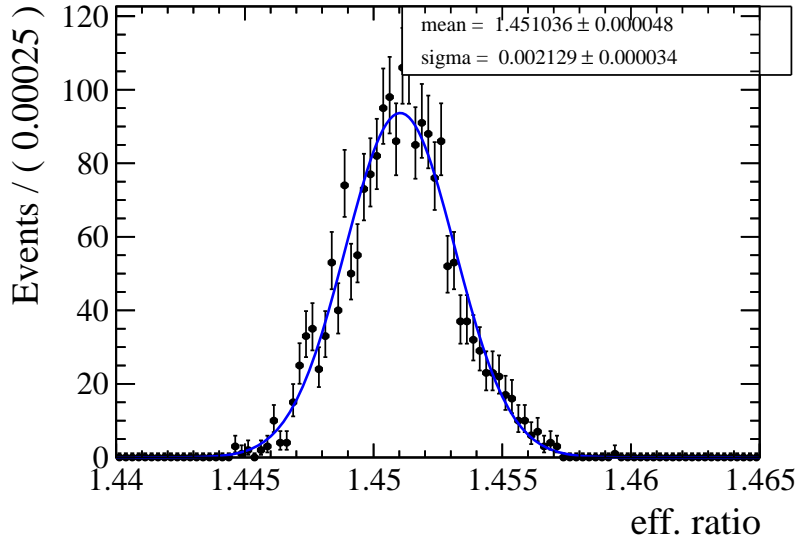

 图 3.13 Trigger efficiency in bins of p_T for (a) p and (b) \bar{p}


图 3.14 Fit of the trigger efficiency ratio of control mode and signal mode

3.5.5.2 HLT1 and HLT2 efficiency

The HLT1 and HLT2 are well described by MC, hence their efficiencies are calculated from MC directly. The results are shown in Table ???. The ratio of HLT efficiencies between the control and signal modes is measured to be 0.931 ± 0.165 .

3.5.5.3 Ratio of trigger efficiencies

Combine the L0, HLT1 and HLT2 efficiencies together, the ratio of trigger efficiencies between the control and signal modes is found to be 1.351 ± 0.259 .

表 3.24 Trigger efficiency(w.r.t the previous trigger)

Trigger line	Signal mode	Control mode
-	1028	15880
L0	76	2207
L0+Hlt1	46((60.53 \pm 5.61)%)	1314((59.54 \pm 1.04)%)
L0+Hlt1+Hlt2	23((50.00 \pm 7.37)%)	622((47.34 \pm 1.38)%)

3.5.6 Summary

Each of the efficiency ratios in eq. 3-7 has been considered and evaluated. We will consider systematic uncertainties on the efficiency ratios in sec. ??, then quote combined efficiency ratios (in terms of α) taking into account variation with lifetime in sec. ?. We will consider variation of α with $m(\Xi_{cc})$ in sec. ??.

3.5.7 Note on efficiency of Ξ_{cc}^+ mass window

In section 3.6.3 we will explain how the Ξ_{cc}^+ signal yield is measured. This will include requiring that the signal candidate sits inside a δm window of width 20 MeV/ c^2 . In practice there will be tails that lie outside this window, resulting in some efficiency loss. The resolution depends on the Q value of the decay, i.e. on δm . Therefore this will give a δm -dependent efficiency correction term. This will be considered as a correction in section ?? (in particular, section ??).

3.6 Yield determination

After applying the full selection, we are almost ready to extract the signal yield in data. In this section we describe some necessary preliminaries, then set out the yield extraction procedure. We are still blind at the time of writing, so this section is a bit abstract in places. For illustration we have run one toy experiment through the entire analysis chain described in this section as though it were the data, including making plots and quoting upper limits. This test is described in Appendix ??.

3.6.1 Fit to the Λ_c^+ control mode

After all the cuts and trigger requirements, the control mode has 105k candidates left. An unbinned maximum likelihood is performed to extract the Λ_c^+ events in the

control mode. The signal pdf is a double Gaussian and the background pdf is a first order Chebychev. The fit is shown in Fig. 3.15. The signal yield is found to be $N_{\text{con}} = 40910.9 \pm 363.849$. Note there is a prescale factor of 0.05 in the stripping line for the Λ_c^+ control mode, so the actual signal in the data sample is 20 times larger: $(818 \pm 7) \times 10^3$. This will be included in the calculation of α .

The resolution seen in this high-statistics fit will be used as a guide to the appropriate signal window size in Sec. 3.6.3. However, we do not assume that the lineshape is the same (and indeed it may not be since the kinematics of the Λ_c^+ may differ between the control and signal samples).

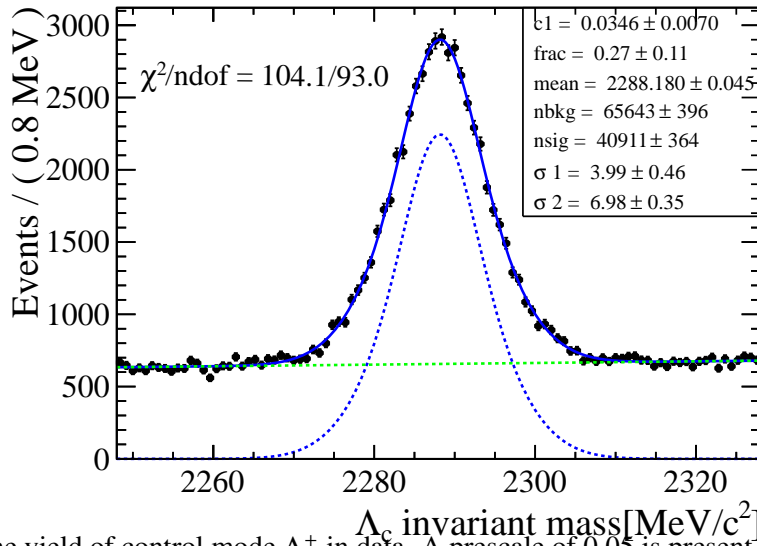


图 3.15 The yield of control mode Λ_c^+ in data. A prescale of 0.05 is present in the stripping.

3.6.2 Fit to the Ξ_{cc}^+ signal in Monte Carlo

We will use two different yield measurement strategies in data, but both use δm as a discriminating variable between signal and background, where δm is the mass difference defined in Eq. 3-4. Because the signal yield may be zero, we can't get the signal lineshape from the data. Instead, we will use signal MC as a guide. The yield extraction methods don't rely on us knowing the details of the signal lineshape, but we do need to know the resolution σ well enough to define a useful signal window.

Figure 3.16 shows the spectrum of δm in truth-matched signal events. The fitted lineshape is the sum of two Gaussians with a common mean. For the purposes of defining a signal window, we take the resolution to be $5 \text{ MeV}/c^2$.

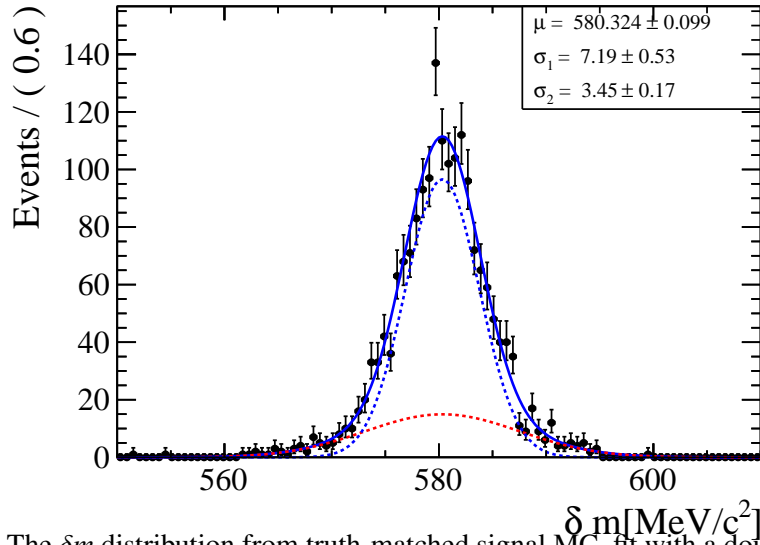


图 3.16 The δm distribution from truth-matched signal MC, fit with a double Gaussian.

3.6.3 Yield measurement procedures for Ξ_{cc}^+ in data

3.6.3.1 Overview

We will use two complementary procedures to extract the yield in data, described below. This serves as a cross-check of the procedure—one of the major causes of false discoveries in spectroscopy is improper modeling of the background. We use the same general approach in both cases, namely:

1. Pick a signal mass hypothesis (e.g. $\delta m_0 = 602 \text{ MeV}/c^2$).
2. Define a symmetric signal window around that mass (e.g. $\delta m_0 - 2\sigma < \delta m < \delta m_0 + 2\sigma$ for σ taken to be $5 \text{ MeV}/c^2$).
3. Use the data outside that window to determine the background level, and estimate the expected background N_b inside the signal window.
4. Count the number of events in the signal window N_{s+b} .
5. Thus, the signal yield is $N_s = N_{s+b} - N_b$.

This has the advantage that we don't need to fit the signal itself, which is difficult for a number of reasons^①. The penalty is that the method is not statistically optimal, in the sense that we could have more signal/background discrimination if we used the full signal lineshape, but we are willing to pay this price.

① Most problems arise because we have very low background and also an expected signal yield of zero or close to zero. This makes a χ^2 fit impossible, since χ^2 fits are biased when the yield per bin is small and the background is estimated from the data. It also makes likelihood fits difficult to interpret, since negative PDFs are not allowed so the signal yield must be bounded below at zero.

In both methods, we assume that the background can be described as the sum of two components: pure combinatorics and Λ_c^+ background. Both have a smooth distribution in δm (though not necessarily the same as one another). The combinatoric component is also smooth in $m(\Lambda_c^+)$, whereas the Λ_c^+ background is made of a real Λ_c^+ and so peaks in the right place in $m(\Lambda_c^+)$.

The first method, referred to as “25 Tiles”, is a 2D local sideband subtraction in $(m(\Lambda_c^+), \delta m)$ that does not use any fitting at all. Basically, it’s a just a generalization of plain old sideband subtraction to work in 2D and allow for some curvature in the background. We define a big rectangle of width 80 MeV/ c^2 in $m(\Lambda_c^+)$ and width 200 MeV/ c^2 in δm , and a small signal window of width 30 MeV/ c^2 in $m(\Lambda_c^+)$ and 20 MeV/ c^2 in δm at the centre of the rectangle. We assume that the combinatoric background can be described by a smooth 2D quadratic function and the Λ_c^+ background can be described as the product of a signal peak in $m(\Lambda_c^+)$ and a smooth 1D quadratic function in δm within the rectangle^①. We can then use the 2D sidebands to make an analytic estimate of the expected background in the small signal window along with its statistical uncertainty. (A detailed description of the procedure is available in Appendix ?? along with a diagram showing the 2D windows.)

The second method, referred to as “1D Fit & Count”, involves a 1D fit to the δm spectrum across a wide range, from threshold at $\delta m = 0$ up to an upper bound of $\delta m = 1500$ MeV/ c^2 but excluding the signal window of width 20 MeV/ c^2 . The fit function is then integrated across the signal window to give the expected background. The function used is a two-sided Landau, described in more detail below.

The final results will be quoted with the 25 Tiles method, which we consider to be more robust because it doesn’t require us to guess the functional shape of the background in the blinded region before unblinding.

① In effect, we’re making a Taylor expansion of the background. If you make your extrapolation window narrow enough, the background is linear; the wider the range you have to describe, the higher the order of polynomial required. We made toy MC tests with background models based on the data sidebands and found that for a δm window of width 200 MeV, a first-order polynomial wasn’t enough and led to a bias but second-order was OK.

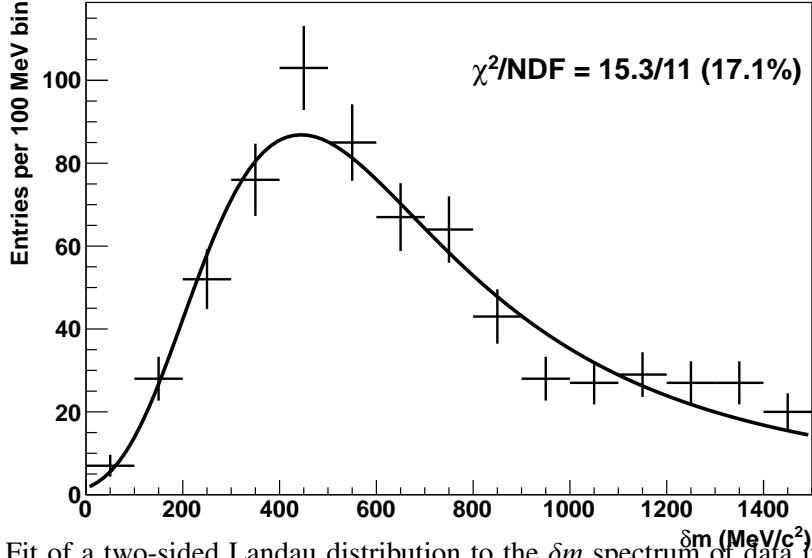


图 3.17 Fit of a two-sided Landau distribution to the δm spectrum of data in the $m(\Lambda_c^+)$ sidebands. All events in the region 2248–2328 MeV/c^2 are excluded. In this fit: $\mu = 484 \pm 33$, $\sigma_L = 177 \pm 18 \text{ MeV}/c^2$, $\sigma_R = 170 \pm 19 \text{ MeV}/c^2$.

3.6.3.2 Definition of two-sided Landau

When we need to fit the background shape in the δm projection, we use a two-sided Landau function defined as:

$$f(\delta m) = \begin{cases} L(\delta m; \mu, \sigma_L) & \delta m \leq \mu \\ aL(\delta m; \mu, \sigma_R) & \delta m \geq \mu \end{cases} \quad (3-10)$$

where $L(\delta m; \mu, \sigma)$ is a Landau distribution and a is chosen such that $L(\delta m; \mu, \sigma_L) = aL(\delta m; \mu, \sigma_R)$. A fit to data in the $m(\Lambda_c^+)$ sidebands is shown in Fig. 3.17. We also compare the δm spectrum in the $m(\Lambda_c^+)$ sidebands to that in the $m(\Lambda_c^+)$ signal region (blinded) in Fig. 3.18.

3.6.3.3 Validation with Toy MC

We use toy experiments to check that the yield measurement procedure is unbiased and reports correct statistical uncertainties. In these toys the data is assumed to consist of three components:

- Signal: Gaussian in both $m(\Lambda_c^+)$ and δm
- Λ_c^+ combinatorics: Gaussian in $m(\Lambda_c^+)$ and smooth in δm
- Pure combinatorics: Smooth in both $m(\Lambda_c^+)$ and δm

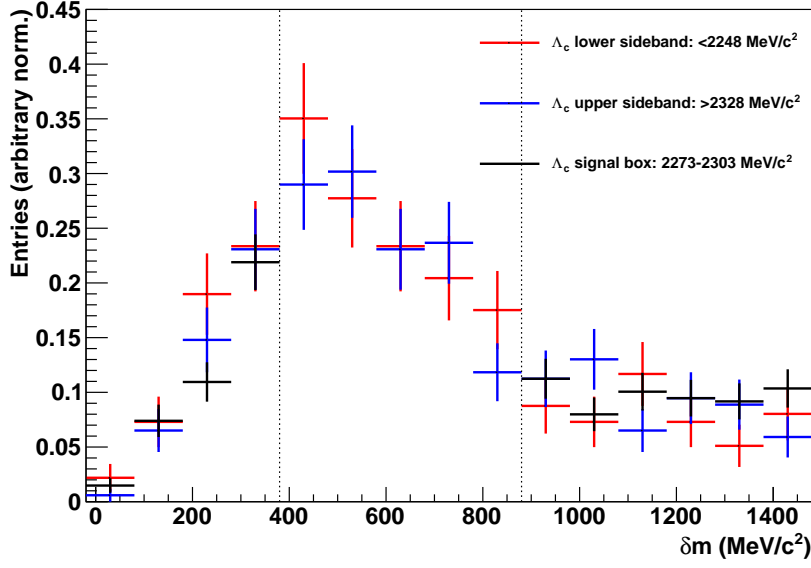


图 3.18 Comparison of the δm spectrum in the $m(\Lambda_c^+)$ sidebands (red, blue) to the blinded spectrum in the $m(\Lambda_c^+)$ signal region (black). The blinded δm signal window is indicated by the dotted vertical lines. The three datasets are normalized to have the same integral outside the blinded region. Note that the x -axis is shifted by 20 MeV/c^2 in order to align the bin edges with the blinded region.

The $m(\Lambda_c^+)$ shapes are taken from a fit to the inclusive $m(\Lambda_c^+)$ spectrum in the δm sidebands in data, with the peak described by a single Gaussian and the background described by a first-order polynomial. The δm shape for signal is taken to be a single Gaussian, and that for background is a two-sided Landau fitted to the δm spectrum in the $m(\Lambda_c^+)$ sidebands in data, as shown in Fig. 3.17. We assume that this describes the Λ_c^+ combinatorics as well as the pure combinatorics (since we can't check the Λ_c^+ combinatoric background shape in δm without unblinding).

A toy experiment consists of the following steps:

1. Choose expected background yields to be comparable to those expected in data (based on extrapolation from sidebands).
2. Choose expected signal yield.
3. Generate background data according to the distributions described above, with the number of background events of each category Poisson-fluctuated around the expected value.
4. Generate signal data according to the distribution described above, with the number of signal events Poisson-fluctuated around the expected value.
5. Step through the allowed range in δm . For each δm value, run the yield extraction

procedure and record the p-value for consistency with the null hypothesis. (See below for how this is defined.)

6. Record the results at each step, as well as the average p-value and the most significant (smallest) p-value seen in the toy.

For both the 25-Tiles and the 1D Fit & Count methods, we carry out toy studies as described above with the expected signal set to zero (i.e. never generating any signal events). We use δm steps of 25 MeV across the range 380–880 MeV (i.e. 21 points per toy experiment). We carry out 1000 toys for each method, finding an average p-value across all steps and toys of 0.504 for the 25-Tiles method and 0.511 for the 1D Fit & Count method.

It's a little tricky to obtain the local p-values described above—the difficulty is in getting the error estimates correct. This won't actually matter in the end because the local p-values are not used at all for setting upper limits and will only be used indirectly for the LEE-corrected significance (see Sec. 3.6.3.5: the final LEE-corrected p-values will be set using ensembles of toys). Nonetheless, it's worth explaining what's going on. The local p-value p_{local} is defined via the significance s as follows:

$$s = \frac{y_{\text{tot}} - y_{\text{bkg}}}{\sqrt{\sigma_{\text{tot}}^2 + \sigma_{\text{bkg}}^2}} \quad (3-11)$$

$$p_{\text{local}} = \frac{1}{2} \left(1 - \text{Erf}(s/\sqrt{2}) \right) \quad (3-12)$$

where y_{tot} is the observed yield in the signal box, y_{bkg} is the expected background yield estimated from sidebands, σ_{tot} is the uncertainty on the observed yield, and σ_{bkg} is the uncertainty on the estimate of the expected background yield. The problem is with σ_{tot} , and more specifically with how it is correlated with the signal yield. We can't simply take it as $\sqrt{y_{\text{tot}}}$, else we get p-values that are biased towards 1: upward fluctuations in the signal box yield get bigger uncertainties (so the significance is reduced) and downward fluctuations in the signal box yield get smaller uncertainties (so the significance is again reduced). Conversely, even under the null hypothesis we can't take it as $\sqrt{y_{\text{bkg}}}$, else we get p-values that are biased towards 0: downward fluctuations in the sidebands reduce the expected background, giving a bigger signal excess with a smaller uncertainty (vs. a smaller signal with a bigger uncertainty for upward sideband fluctuations). The compromise used is to set

$$\sigma_{\text{tot}} = \max(\sqrt{y_{\text{tot}}}, \sqrt{y_{\text{bkg}}}) \quad (3-13)$$

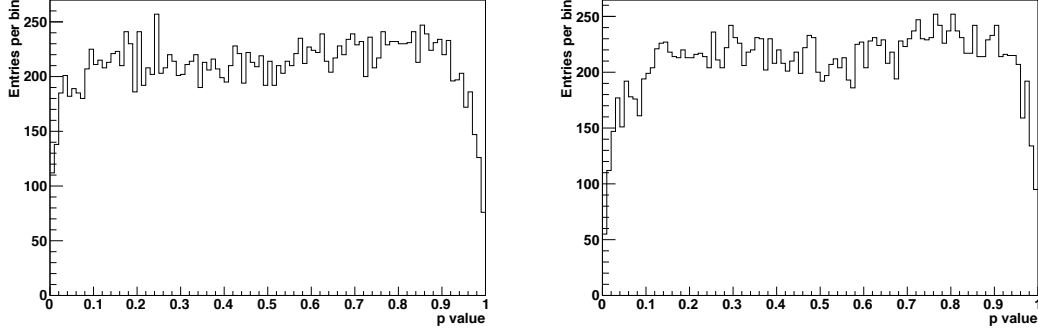


图 3.19 Distributions of local p-values obtained as described in Sec. 3.6.3.3 for the 25-Tiles method (left) and the 1D Fit & Count method (right) using a sample of 1000 toy experiments, taking 21 points per toy. See caveats in the text! These are not the final corrected p-values.

which tends to over-estimate the errors for large fluctuations in either direction but in a more-or-less symmetric way. The resulting local p-value distributions are shown in Fig. 3.19.

3.6.3.4 Quoting an upper limit on the yield

As described in Sec. 3.6.3.1, we define a signal box and then use data outside that box to estimate the background level inside the box and take the excess as an estimate of the signal yield.

We expect that the yield will be consistent with zero and that we will want to set an upper limit. This is done with the CL_s method. Define $CL_{s+b}(n_{\text{obs}}, n_{\text{exp}})$ to be the probability of seeing a count smaller than or equal to n_{obs} under a signal-plus-background hypothesis with expected signal yield n_{exp} . Define $CL_b(n_{\text{obs}})$ to be the probability of seeing a count smaller than or equal to n_{obs} under the background-only hypothesis. Then CL_s is defined as:

$$CL_s(n_{\text{obs}}, n_{\text{exp}}) = \frac{CL_{s+b}(n_{\text{obs}}, n_{\text{exp}})}{CL_b(n_{\text{obs}})}.$$

The 95% confidence level upper limit on the yield is the value of n_{exp} for which $1 - CL_s(n_{\text{obs}}, n_{\text{exp}}) = 0.95$ given the observed result n_{obs} . This calculation is simple to do: given an expected yield, we just sum over Poisson probabilities.

However, this just gives us the upper limit on the yield for a particular mass hypothesis (neglecting systematic errors). There are two more steps needed. First, we need to be able to convert this into an upper limit on R (from Eq. 3-3), which means including

the control channel yield and relative efficiency correction (and their associated uncertainties). Second, we need to combine mass hypotheses together—501 individual upper limits would be way too much information for anyone trying to interpret this. While we plan to include a plot of that in the paper for completeness, the main results will be quoted as follows (assuming a null result):

- We will quote the largest (i.e. worst) upper limit across the entire mass range, i.e. all 501 points in $380 < \delta m < 880 \text{ MeV}/c^2$ in steps of $1 \text{ MeV}/c^2$.
- We will also divide the data into disjoint 50 MeV intervals and quote the largest UL in each interval. This is probably rather more useful to a theorist who has a model with an approximate mass for the state.

When including systematic effects, the procedure is more complicated because we can no longer do a simple analytic calculation. Instead, we will use an MC-based calculation. This is discussed in more detail in Section ??.

3.6.3.5 The Look Elsewhere Effect

If we see no signal, the upper limits on R are the end of the story for this analysis. However, if we do see a clear peak then we need to establish its significance compared to the null hypothesis, taking into account the fact that we have tested many different mass hypotheses (the Look Elsewhere Effect). The procedure is as follows:

1. Run N toy experiments as defined in Sec. 3.6.3.3 with zero signal yield. In each toy experiment we do 501 steps of 1 MeV as in data. We record the smallest p-value seen in each toy experiment.
2. For any per-test p-value p_{test} , we can ask how many toys had a per-test p-value that small or smaller. Call the number of such toys $n(p_{\text{test}})$.
3. Then if we do the real experiment on data and the lowest per-test p-value we see is p_{data} , this corresponds to a LEE-corrected p-value of $n(p_{\text{data}})/N$.

In the limit that every step were completely independent, the LEE correction would be calculable analytically (roughly speaking, it would typically be a factor of 501). But because the measurements are correlated—especially for the 1D Fit & Count method, where essentially the same background sample is used for every step—the correction is smaller and the easiest way to estimate it is with toys. LEE correction curves are shown in Fig. 3.20.

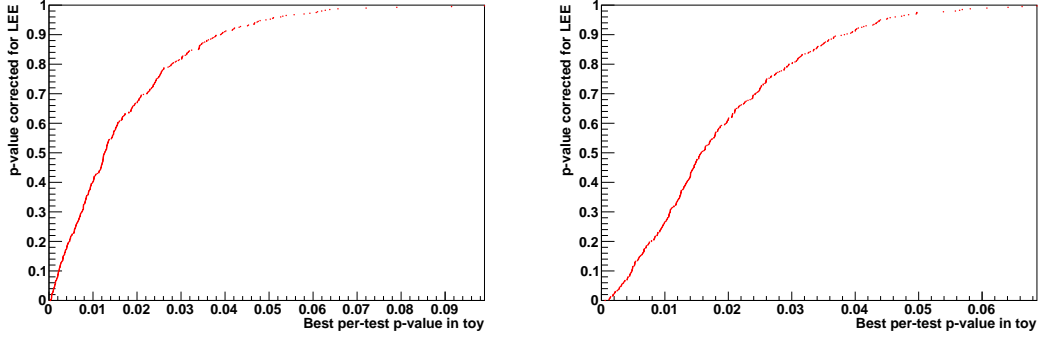


图 3.20 Example LEE corrections derived from toy studies, for the 25-Tiles method (left) and the 1D Fit & Count method (right). Each is made with a sample of 400 toys.

Note that to check for the existence of a peak we don't need to apply any efficiency correction, nor is there any systematic uncertainty associated with the efficiency.

3.6.4 Decays via a Σ_c

So far we have treated the Ξ_{cc} decay as pure 3-body. However, it may also decay via an intermediate resonance such as $\Xi_{cc}^+ \rightarrow \Sigma_c^{++} K^-$, $\Sigma_c^{++} \rightarrow \Lambda_c^+ \pi^+$ in analogy with the decay $\Lambda_c^+ \rightarrow \Delta^{++} K^-$, $\Delta^{++} \rightarrow p \pi^+$. By requiring an intermediate $\Sigma_c(2455)$ or $\Sigma_c(2520)$ we would reduce the BF but could potentially clean up a lot of background. We will do two such tests.

The PDG gives the following mass and width parameters:

$$m(\Sigma_c^{++}(2455)) - m(\Lambda_c^+) = 167.52 \pm 0.08 \text{ MeV}/c^2$$

$$m(\Sigma_c^{++}(2520)) - m(\Lambda_c^+) = 231.4 \pm 0.6 \text{ MeV}/c^2$$

$$\Gamma(\Sigma_c^{++}(2455)) = 2.26 \pm 0.25 \text{ MeV}/c^2$$

$$\Gamma(\Sigma_c^{++}(2520)) = 14.9 \pm 1.5 \text{ MeV}/c^2$$

Taking $m(\pi^+) = 139.57 \text{ MeV}/c^2$, this corresponds to:

$$m(\Sigma_c^{++}(2455)) - m(\Lambda_c^+) - m(\pi^+) = 27.95 \pm 0.08 \text{ MeV}/c^2$$

$$m(\Sigma_c^{++}(2520)) - m(\Lambda_c^+) - m(\pi^+) = 91.83 \pm 0.6 \text{ MeV}/c^2$$

Both the natural width and the expected experimental resolution are narrower for the $\Sigma_c^{++}(2455)$ than for the $\Sigma_c^{++}(2520)$. For the former, we take a window of $\pm 4.0 \text{ MeV}/c^2$

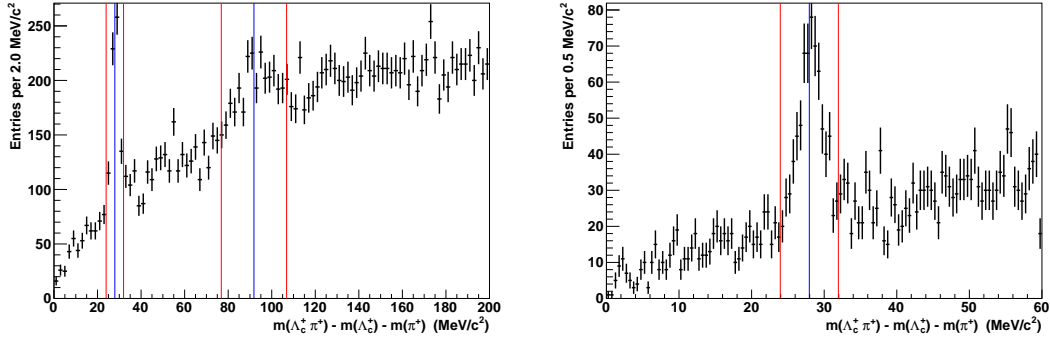


图 3.21 The inclusive $m(\Lambda_c^+\pi^+) - m(\Lambda_c^+) - m(\pi^+)$ spectrum in data close to threshold, for illustration. A cut of $2755 < m(\Lambda_c^+) < 2300$ MeV/ c^2 has been applied. The blue vertical lines indicate the nominal mass difference for the $\Sigma_c^{++}(2455)$ and the $\Sigma_c^{++}(2520)$, and the red lines show the cut windows that will be used to select these states. Both plots show the same data, but over different x -axis ranges.

around the nominal mass difference above—this is chosen by eye to capture nearly all of the peak in data. For the latter, we take a window of ± 15 MeV/ c^2 (i.e. $\pm\Gamma$, rounded off). These are illustrated in Fig. 3.21. After applying the appropriate mass window, we will repeat the yield extraction study discussed above (and LEE correction^①, if required). However, we will not quote a separate upper limit for R on the Σ_c resonances but (assuming a null result) will simply say that this was tested for and no significant signal seen.

① Note that for the Σ_c tests we'll make a LEE correction for testing different Ξ_{cc} δm hypotheses as usual if a peak is seen, but we will not add a further correction for the fact that we check both 3-body and quasi-two-body decays.

第 4 章 Systematic Uncertainties

There are many sources of systematic uncertainties, which may affect the results, as described below.

4.1 Tracking efficiency uncertainty

As mentioned in Section 3.5.2.1, the tracking efficiency is not accurately described by MC. Corrections are needed to account for differences between data and MC. According to the method provided by the tracking group, the corrections consist of three parts.

The first part is data-MC tracking efficiency ratio. The uncertainty of the ratio in each $p - \eta$ bin lead to an uncertainty of the overall efficiency ratio. We fit the distribution of the data-MC tracking efficiency ratio with a Gaussian function, this overall uncertainty can then be estimated by the width divided the mean of the fit. This source contributes an uncertainty of 2.1%.

The second part is the neglect of kinematic correlations between the daughter tracks in the calculation of the ratio in the previous part. We assign 0.7% correlated systematic per track following the procedure of Ref.^[129]. Both the signal and control channel contain Λ_c^+ decay, so we consider the Λ_c^+ part of the uncertainty cancel in the ratio, and only the two daughter tracks from Ξ_{cc}^+ contribute. The systematic uncertainty due to kinematics correlations is 1.4%.

The third comes from hadronic interactions of the daughter tracks. The tracks used for signal reconstruction should be long tracks, which should have hits in the downstream-most tracking stations. The hadronic interaction of the daughter tracks means the track is not reconstructed and would cause a loss of efficiency. This source of inefficiency is not corrected by the data-MC ratio table, as the data-MC ratio table is obtained by a tag-and-probe method using $J/\psi \rightarrow \mu^+ \mu^-$, which do not have hadronic interactions. Following the procedure of Ref.^[129], we assign 2% per hadron for the uncertainty on material interactions. As long as one of the tracks has the hadronic interaction, the event will not be reconstructed. Therefore the uncertainty should be fully correlated between all the daughter tracks. Again, the Λ_c^+ part of the uncertainty is expected to cancel in the

ratio. The systematic uncertainty due to hadronic interactions is 4%.

Combine the previous numbers in quadrature the systematic error due to tracking efficiency is 4.72%.

4.2 Multiple Candidates

After the whole selection chain, there are some candidates that have a common event number, which labels they are from the same event. In most cases, some of the candidates will share one or two tracks, so it is sure that at most only one of them could be the true signal. Even they don't have any track in common, it should be noted that the probability for one event has two Ξ_{cc}^+ is so small that it is almost certain that at least one of them should be a fake signal. Across the whole $1.5 \text{ GeV}/c^2$ signal window, we see this in about 6% of events. This is not surprising, given that the mass window is so huge and that a real Λ_c^+ can be combined with pair of tracks in more than one way. In the case of correlated multiple candidates, they may cause a peaking structure in the mass spectrum and an overestimation of the signal events. But as we shall see, for our case multiple candidates do not form peaking background. For the selected Ξ_{cc}^+ signal MC, the Λ_c^+ is randomly combined with a kaon track and a pion track from two other events. The kinematic selection is applied, but not the vertex or pointing cuts (e.g. no DOCA or vertex χ^2) due to the difficulty in defining these variables for tracks from different events. The “ Ξ_{cc}^+ ” sample generated by this procedure may not present all possible backgrounds, but it reveals the problem if multiple candidates cause a peaking structure. Fig. 4.1 shows the invariant mass spectrum of randomly combined “ Ξ_{cc}^+ ” candidates. No significant peak or structure is found across the mass range. The same procedure was done to form random Λ_c^+ candidates, with the spectrum shown in Fig. 4.2. No structure is found. Besides, to apply a veto/selection on multiple candidates would make our efficiency dependent on the background level and on the size of the mass window, which we don't want to do. So we do not apply any multiple candidate veto/selection and retain all candidates. Since the signal events will not be biased, we do not assign any systematic uncertainty due to multiple candidates.

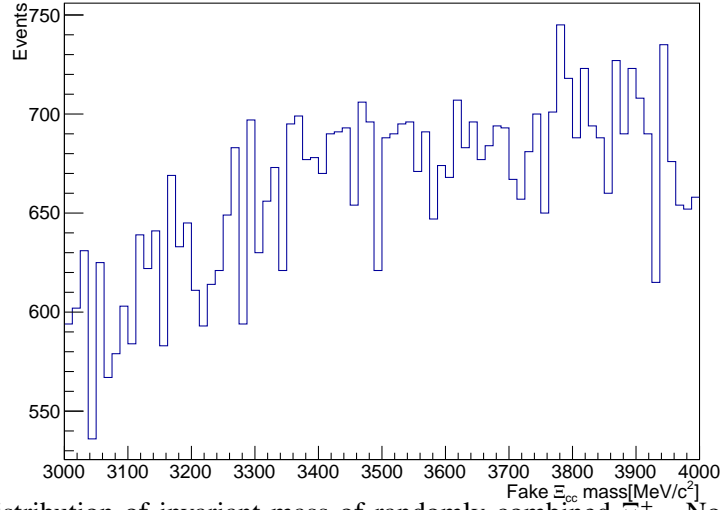


图 4.1 The distribution of invariant mass of randomly combined Ξ_{cc}^+ . No significant peak or structure is found in the mass range.

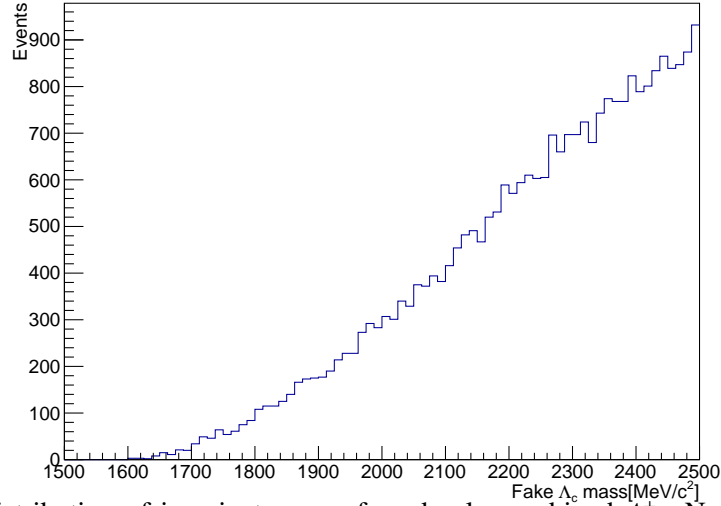


图 4.2 The distribution of invariant mass of randomly combined Λ_c^+ . No significant peak or structure is found in the mass range.

4.3 Stripping, offline cuts and MVA efficiency

The efficiency of these three steps are evaluated from Monte Carlo simulation. Most variables are well reproduced by MC (the PID related variables are not considered here), with one notable exception: the IP χ^2 .

To account for the IP χ^2 difference between MC and data, the tracking group developed a specific tool to smear the track parameters of MC, so that the IP χ^2 can agree with that observed in data^[134]. But one side-effect of the smearing is that the distribution of vertex χ^2 will also be changed and will disagree with data. We will use different strategies

to study this effect on (a) stripping + offline cuts, and (b) the MVA efficiency.

For stripping + offline cuts, we simply calculate the ratio of efficiencies between control and signal modes both with and without track smearing. The change seen when using smearing is 6.6% and is taken as the systematic uncertainty (Tab. 4.1). For the MVA, we cannot simply smear the MC sample and recheck the efficiency (because of the effect on the vertex χ^2 cut discussed above). Instead, we weight unsmeared test MC sample so that its IP χ^2 distribution matches that of the smeared sample, then apply the standard MVA with the standard cut of $MLP > 0.8$. The difference in efficiency before and after reweighting is found to be 6.7% and is taken as the systematic uncertainty (Fig. 4.3).

Finally, we combine the two systematic errors described above. To be conservative, we assume that the effects are fully correlated and so add the systematic errors linearly to obtain 13.3%.

表 4.1 The efficiency of the stripping and offline cuts (excluding PID) for MC samples with and without track smearing for IP χ^2 .

Sample	signal mode	control mode
standard sample	$(3.18 \pm 0.04) \times 10^{-3}$	$(1.22 \pm 0.01) \times 10^{-2}$
smeared sample	$(3.16 \pm 0.04) \times 10^{-3}$	$(1.29 \pm 0.01) \times 10^{-2}$

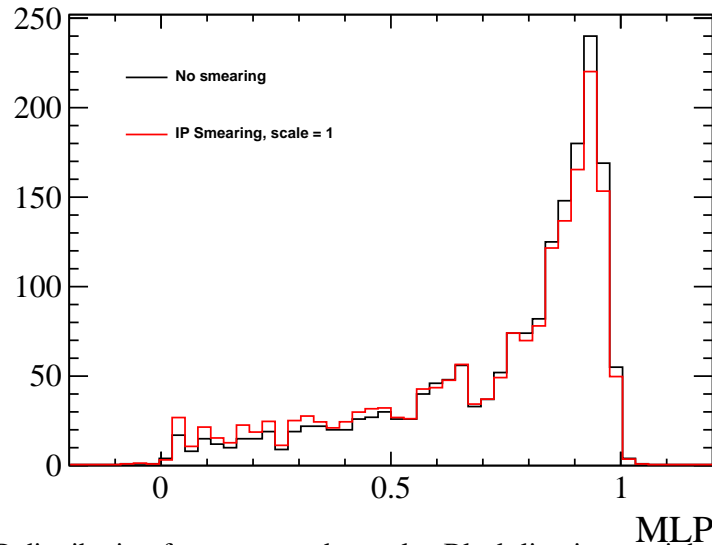


图 4.3 The MLP distribution for unsmeared sample. Black line is unweighted sample and red line is the sample with IP χ^2 weighted to smeared sample.

表 4.2 Ξ_{cc}^+ MC: final states correlation check. The product of the individual efficiencies is 0.483 and the efficiency when applying all cuts simultaneously is 0.509.

Cut	$\Lambda_c^+ p$ PIDp	$\Lambda_c^+ K$ PIDK	$\Lambda_c^+ \pi$ PIDK	$\Xi_{cc}^+ K$ PIDK	$\Xi_{cc}^+ \pi$ PIDK	events	eff.
Sample0	-	-	-	-	-	7187	-
Sample1	> 10	-	-	-	-	6893	0.959
Sample2	-	> 10	-	-	-	6547	0.911
Sample3	-	-	< -5	-	-	5725	0.797
Sample4	-	-	-	> 10	-	6544	0.911
Sample5	-	-	-	-	< -5	5478	0.762
Sample6	> 10	> 10	< -5	> 10	< -5	3655	0.509

4.4 PID calibration

The procedure of PID calibration is described in Chapter ???. Several approximations have been made to extract the PID cut efficiency, and they may cause systematic uncertainties.

4.4.1 The calibration result

The PID efficiency ratio estimated with the calibration samples is 1.748 ± 0.034 , so the quasi-statistical contribution to the systematic error is 1.95%.

4.4.2 The kinematic correlation between final tracks

Since the final-state tracks share the energy of their mother, there are kinematic correlations between them and hence the PID variables of these tracks are correlated. But in the calculation of the PID efficiency these correlations are neglected and the overall efficiency is simply the product of the individual efficiencies. There is a systematic uncertainty on the ratio of efficiencies of the control and signal modes associated with the assumption that the PID efficiencies factorize. To investigate this we will compare the ratio calculated in the baseline way (assuming that the PID efficiencies factorize) to the ratio calculated by applying all PID cuts simultaneously. The individual and simultaneous efficiencies are shown in Table 4.2 for Ξ_{cc}^+ and Table 4.3 for Λ_c^+ . The difference between the two approaches (ratio of 0.634/0.483 vs ratio of 0.648/0.509) is found to be 3%, and is taken as the systematic uncertainty.

表 4.3 Λ_c^+ MC: final states correlation check The product of the individual efficiencies is 0.634 and the efficiency when applying all cuts simultaneously is 0.648.

Cut	$\Lambda_c^+ p$ PIDp	$\Lambda_c^+ K$ PIDK	$\Lambda_c^+ \pi$ PIDK	events	eff.
Sample0	-	-	-	24689	-
Sample1	> 10	-	-	23234	0.941
Sample2	-	> 10	-	21786	0.882
Sample3	-	-	< -5	18870	0.764
Sample4	> 10	> 10	< -5	15999	0.648

4.4.3 The multiplicity of MC

As explained in Section 3.5.3, the PID efficiency depends on the RICH occupancy and therefore the multiplicity. But the true distribution of Ξ_{cc}^+ multiplicity is unknown, so this is an intrinsic uncertainty of PID calibration. In the baseline calculation of Sec 3.5.3, we reweighted the Ξ_{cc}^+ MC to match the multiplicity distribution of B_s data, and the Λ_c^+ MC to match that of Λ_c^+ data. We now consider two other cases: first as above except that the Ξ_{cc}^+ MC is reweighted to match Λ_c^+ data, and second to use unweighted MC (i.e. taking the multiplicity distributions from MC). For the first case the efficiency ratio becomes 1.740 (a shift of 0.5% from the baseline), and for the second case the ratio becomes 1.479 (a shift of 15% relative to the baseline). Taking the mean of these two cases, we assign a systematic uncertainty of 7.8%. (See Tab. 4.4, 4.5, 4.6, 4.7, 4.8, 4.9, 4.10, 4.11 for the result of the first case, and 4.12, 4.13, 4.14, 4.15, 4.16, 4.17, 4.18, 4.19 for the result of the second case.)

 表 4.4 The calibration of K from Λ_c^+ in Ξ_{cc}^+ MC, with Ξ_{cc}^+ MC multiplicity weighted to Λ_c^+ data

SubID	MagDown		MagUp	
	Run range	PIDK > 10 Efficiency	Run Runge	PIDK > 10 Efficiency
2	92821-93224	-	94261-96641	(86.99 ± 0.23)%
3	93225-97884	(87.01 ± 0.21)%	96642-100243	(87.02 ± 0.24)%
4	97885-98198	(87.64 ± 0.20)%	100244-102505	(86.76 ± 0.22)%
5	98199 -101905	(87.24 ± 0.22)%	102506-102893	(86.79 ± 0.21)%
6	101906-102378	(86.97 ± 0.22)%	102894-104263	(86.55 ± 0.33)%
7	102379-103361	(86.86 ± 0.20)%		-
8	103362-103686	(87.37 ± 0.20)%		-

表 4.5 The calibration of p from Λ_c^+ in Ξ_{cc}^+ MC, with Ξ_{cc}^+ MC multiplicity weighted to Λ_c^+ data

SubID	MagDown		MagUp	
	Run range	PIDp > 10 Efficiency	Run Runge	PIDp > 10 Efficiency
2	92821-93224	–	94261-96641	(89.12 ± 0.38)%
3	93225-97884	(89.81 ± 0.40)%	96642-100243	(89.61 ± 0.70)%
4	97885-98198	(89.58 ± 0.30)%	100244-102505	(88.91 ± 0.50)%
5	98199 -101905	(90.29 ± 0.87)%	102506-102893	(88.74 ± 0.47)%
6	101906-102378	(89.69 ± 0.49)%	102894-104263	(89.29 ± 0.91)%
7	102379-103361	(90.41 ± 0.70)%		–
8	103362-103686	(88.79 ± 0.67)%		–

 表 4.6 The calibration of π from Λ_c^+ in Ξ_{cc}^+ MC, with Ξ_{cc}^+ MC multiplicity weighted to Λ_c^+ data

SubID	MagDown		MagUp	
	Run range	PIDK < -5 Efficiency	Run Runge	PIDK < -5 Efficiency
2	92821-93224	–	94261-96641	(70.49 ± 0.21)%
3	93225-97884	(69.63 ± 0.18)%	96642-100243	(67.06 ± 0.22)%
4	97885-98198	(66.68 ± 0.19)%	100244-102505	(65.36 ± 0.21)%
5	98199 -101905	(68.19 ± 0.19)%	102506-102893	(67.01 ± 0.22)%
6	101906-102378	(67.92 ± 0.19)%	102894-104263	(65.57 ± 0.37)%
7	102379-103361	(67.91 ± 0.19)%		–
8	103362-103686	(65.54 ± 0.20)%		–

 表 4.7 The calibration of K from Ξ_{cc}^+ in Ξ_{cc}^+ MC, with Ξ_{cc}^+ MC multiplicity weighted to Λ_c^+ data

SubID	MagDown		MagUp	
	Run range	PIDK > 10 Efficiency	Run Runge	PIDK > 10 Efficiency
2	92821-93224	–	94261-96641	(87.24 ± 0.23)%
3	93225-97884	(87.16 ± 0.22)%	96642-100243	(87.27 ± 0.24)%
4	97885-98198	(87.87 ± 0.21)%	100244-102505	(87.15 ± 0.23)%
5	98199 -101905	(87.41 ± 0.22)%	102506-102893	(87.12 ± 0.22)%
6	101906-102378	(87.12 ± 0.23)%	102894-104263	(86.88 ± 0.35)%
7	102379-103361	(87.08 ± 0.21)%		–
8	103362-103686	(87.59 ± 0.21)%		–

表 4.8 The calibration of π from Ξ_{cc}^+ in Ξ_{cc}^+ MC, with Ξ_{cc}^+ MC multiplicity weighted to Λ_c^+ data

SubID	MagDown		MagUp	
	Run range	PIDK < -5 Efficiency	Run Runge	PIDK < -5 Efficiency
2	92821-93224	–	94261-96641	(69.42 ± 0.20)%
3	93225-97884	(67.80 ± 0.22)%	96642-100243	(65.72 ± 0.21)%
4	97885-98198	(64.67 ± 0.22)%	100244-102505	(64.09 ± 0.21)%
5	98199 -101905	(66.26 ± 0.22)%	102506-102893	(65.84 ± 0.21)%
6	101906-102378	(66.03 ± 0.22)%	102894-104263	(64.23 ± 0.35)%
7	102379-103361	(66.00 ± 0.23)%		–
8	103362-103686	(63.52 ± 0.24)%		–

 表 4.9 The calibration of K from Λ_c^+ in Λ_c^+ MC, with Λ_c^+ MC multiplicity weighted to Λ_c^+ data

SubID	MagDown		MagUp	
	Run range	PIDK > 10 Efficiency	Run Runge	PIDK > 10 Efficiency
2	92821-93224	–	94261-96641	(86.10 ± 0.18)%
3	93225-97884	(85.86 ± 0.17)%	96642-100243	(85.97 ± 0.19)%
4	97885-98198	(86.38 ± 0.17)%	100244-102505	(85.84 ± 0.17)%
5	98199 -101905	(86.14 ± 0.18)%	102506-102893	(85.79 ± 0.17)%
6	101906-102378	(85.77 ± 0.18)%	102894-104263	(85.62 ± 0.27)%
7	102379-103361	(85.64 ± 0.16)%		–
8	103362-103686	(86.12 ± 0.17)%		–

 表 4.10 The calibration of p from Λ_c^+ in Λ_c^+ MC, with Λ_c^+ MC multiplicity weighted to Λ_c^+ data

SubID	MagDown		MagUp	
	Run range	PIDp > 10 Efficiency	Run Runge	PIDp > 10 Efficiency
2	92821-93224	–	94261-96641	(88.92 ± 0.54)%
3	93225-97884	(89.56 ± 0.60)%	96642-100243	(89.42 ± 0.89)%
4	97885-98198	(89.03 ± 0.49)%	100244-102505	(88.65 ± 0.67)%
5	98199 -101905	(94.03 ± 1.22)%	102506-102893	(88.39 ± 0.59)%
6	101906-102378	(89.38 ± 0.70)%	102894-104263	(91.50 ± 1.21)%
7	102379-103361	(90.37 ± 1.17)%		–
8	103362-103686	(88.76 ± 0.71)%		–

表 4.11 The calibration of π from Λ_c^+ in Λ_c^+ MC, with Λ_c^+ MC multiplicity weighted to Λ_c^+ data

SubID	MagDown		MagUp	
	Run range	PIDK < -5 Efficiency	Run Runge	PIDK < -5 Efficiency
2	92821-93224	–	94261-96641	(71.61 ± 0.18)%
3	93225-97884	(69.55 ± 0.18)%	96642-100243	(68.26 ± 0.19)%
4	97885-98198	(66.67 ± 0.18)%	100244-102505	(66.74 ± 0.18)%
5	98199 -101905	(68.09 ± 0.18)%	102506-102893	(68.27 ± 0.19)%
6	101906-102378	(67.82 ± 0.18)%	102894-104263	(66.91 ± 0.31)%
7	102379-103361	(67.82 ± 0.18)%	–	–
8	103362-103686	(65.55 ± 0.20)%	–	–

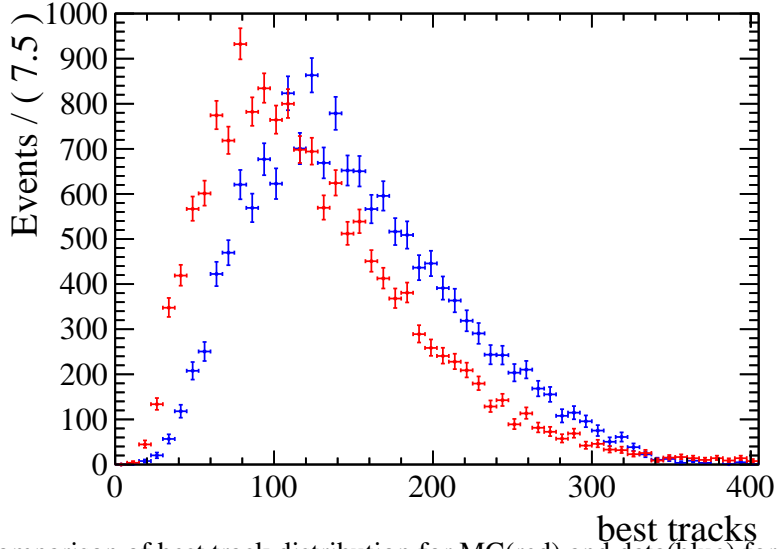

 图 4.4 Comparison of best track distribution for MC(red) and data(blue) for inclusive Λ_c^+ .

 表 4.12 The calibration of K from Λ_c^+ in Ξ_{cc}^+ MC

SubID	MagDown		MagUp	
	Run range	PIDK > 10 Efficiency	Run Runge	PIDK > 10 Efficiency
2	92821-93224	–	94261-96641	(89.81 ± 0.29)%
3	93225-97884	(90.16 ± 0.31)%	96642-100243	(89.65 ± 0.30)%
4	97885-98198	(90.26 ± 0.29)%	100244-102505	(89.40 ± 0.26)%
5	98199 -101905	(90.16 ± 0.27)%	102506-102893	(89.05 ± 0.28)%
6	101906-102378	(90.36 ± 0.33)%	102894-104263	(88.83 ± 0.50)%
7	102379-103361	(89.75 ± 0.29)%	–	–
8	103362 -103686	(90.47 ± 0.27)%	–	–

表 4.13 The calibration of p from Λ_c^+ in Ξ_{cc}^+ MC

SubID	MagDown		MagUp	
	Run range	PIDp > 10 Efficiency	Run Runge	PIDp > 10 Efficiency
2	92821-93224	–	94261-96641	(90.85 ± 0.30)%
3	93225-97884	(91.93 ± 0.43)%	96642-100243	(91.64 ± 0.55)%
4	97885-98198	(91.37 ± 0.26)%	100244-102505	(90.85 ± 0.41)%
5	98199 -101905	(91.02 ± 0.82)%	102506-102893	(90.44 ± 0.31)%
6	101906-102378	(91.21 ± 0.41)%	102894-104263	(89.88 ± 1.15)%
7	102379-103361	(91.91 ± 0.53)%		–
8	103362 -103686	(91.18 ± 0.77)%		–

 表 4.14 The calibration of π from Λ_c^+ in Ξ_{cc}^+ MC

SubID	MagDown		MagUp	
	Run range	PIDK < -5 Efficiency	Run Runge	PIDK < -5 Efficiency
2	92821-93224	–	94261-96641	(75.53 ± 0.27)%
3	93225-97884	(73.85 ± 0.25)%	96642-100243	(71.84 ± 0.30)%
4	97885-98198	(71.08 ± 0.27)%	100244-102505	(70.27 ± 0.33)%
5	98199 -101905	(72.34 ± 0.28)%	102506-102893	(72.05 ± 0.29)%
6	101906-102378	(72.31 ± 0.27)%	102894-104263	(70.43 ± 0.51)%
7	102379-103361	(72.39 ± 0.25)%		–
8	103362 -103686	(69.77 ± 0.30)%		–

 表 4.15 The calibration of K from Ξ_{cc}^+ in Ξ_{cc}^+ MC

SubID	MagDown		MagUp	
	Run range	PIDK > 10 Efficiency	Run Runge	PIDK > 10 Efficiency
2	92821-93224	–	94261-96641	(90.18 ± 0.31)%
3	93225-97884	(90.46 ± 0.31)%	96642-100243	(90.05 ± 0.32)%
4	97885-98198	(90.60 ± 0.29)%	100244-102505	(89.88 ± 0.29)%
5	98199 -101905	(90.45 ± 0.26)%	102506-102893	(89.46 ± 0.31)%
6	101906-102378	(90.59 ± 0.31)%	102894-104263	(89.21 ± 0.58)%
7	102379-103361	(90.11 ± 0.28)%		–
8	103362 -103686	(90.82 ± 0.27)%		–

表 4.16 The calibration of π from Ξ_{cc}^+ in Ξ_{cc}^+ MC

SubID	MagDown		MagUp	
	Run range	PIDK < -5 Efficiency	Run Runge	PIDK < -5 Efficiency
2	92821-93224	–	94261-96641	(74.38 ± 0.27)%
3	93225-97884	(72.57 ± 0.27)%	96642-100243	(70.45 ± 0.29)%
4	97885-98198	(69.70 ± 0.29)%	100244-102505	(68.89 ± 0.32)%
5	98199 -101905	(70.99 ± 0.31)%	102506-102893	(70.75 ± 0.29)%
6	101906-102378	(71.01 ± 0.29)%	102894-104263	(69.07 ± 0.50)%
7	102379-103361	(71.05 ± 0.28)%		–
8	103362 -103686	(68.33 ± 0.33)%		–

 表 4.17 The calibration of K from Λ_c^+ in Λ_c^+ MC

SubID	MagDown		MagUp	
	Run range	PIDK > 10 Efficiency	Run Runge	PIDK > 10 Efficiency
2	92821-93224	–	94261-96641	(87.77 ± 0.20)%
3	93225-97884	(87.59 ± 0.18)%	96642-100243	(87.57 ± 0.21)%
4	97885-98198	(87.91 ± 0.17)%	100244-102505	(87.43 ± 0.18)%
5	98199 -101905	(87.77 ± 0.18)%	102506-102893	(87.22 ± 0.19)%
6	101906-102378	(87.55 ± 0.19)%	102894-104263	(87.04 ± 0.33)%
7	102379-103361	(87.24 ± 0.17)%		–
8	103362 -103686	(87.85 ± 0.18)%		–

 表 4.18 The calibration of p from Λ_c^+ in Λ_c^+ MC

SubID	MagDown		MagUp	
	Run range	PIDp > 10 Efficiency	Run Runge	PIDp > 10 Efficiency
2	92821-93224	–	94261-96641	(90.08 ± 0.47)%
3	93225-97884	(90.92 ± 0.57)%	96642-100243	(90.74 ± 0.82)%
4	97885-98198	(90.18 ± 0.42)%	100244-102505	(89.95 ± 0.61)%
5	98199 -101905	(90.92 ± 0.92)%	102506-102893	(89.49 ± 0.48)%
6	101906-102378	(90.38 ± 0.63)%	102894-104263	(88.79 ± 0.88)%
7	102379-103361	(91.37 ± 0.87)%		–
8	103362 -103686	(88.91 ± 0.72)%		–

表 4.19 The calibration of π from Λ_c^+ in Λ_c^+ MC

SubID	MagDown		MagUp	
	Run range	PIDK < -5 Efficiency	Run Runge	PIDK < -5 Efficiency
2	92821-93224	–	94261-96641	(74.00 ± 0.19)%
3	93225-97884	(71.84 ± 0.19)%	96642-100243	(70.55 ± 0.20)%
4	97885-98198	(69.07 ± 0.20)%	100244-102505	(69.04 ± 0.21)%
5	98199 -101905	(70.39 ± 0.21)%	102506-102893	(70.63 ± 0.20)%
6	101906-102378	(70.20 ± 0.20)%	102894-104263	(69.25 ± 0.35)%
7	102379-103361	(70.22 ± 0.20)%		–
8	103362 -103686	(67.87 ± 0.22)%		–

4.4.4 The calibration method itself

The PID distribution may not only depend on momentum, pseudorapidity and the best track multiplicity, therefore there is an inherent uncertainty in the PID calibration procedure itself. Besides, the variable binnings which cause the lose of information could also be a source of systematic uncertainty. To estimate the size of this inherent uncertainty, a Monte Carlo version of PID calibration is performed, and the weighted distribution of the calibration sample can be compared with the true distribution (i.e. the distribution of the Monte Carlo sample), and the difference can be quoted as the systematic uncertainty. The same calibration procedure is used for the signal and control modes, so we assume that the method systematics associated with the Λ_c^+ part of the decay will cancel and therefore consider only the effect associated with the bachelor K and π .

We find that the pion behaves quite well but that the weighting procedure does not work so well for the kaon (compare the blue and red points in Fig. 4.5). This leads to a modest difference in the ratio of 2.02% for the kaon and a larger difference of 7.73% for the pion. Combining these in quadrature we obtain a total systematic uncertainty of 7.99%.

4.4.5 Summary for PID efficiency

Combining the various PID efficiency uncertainties in quadrature, a total uncertainty of 11.76% is obtained. This is dominated by the track multiplicity uncertainty.

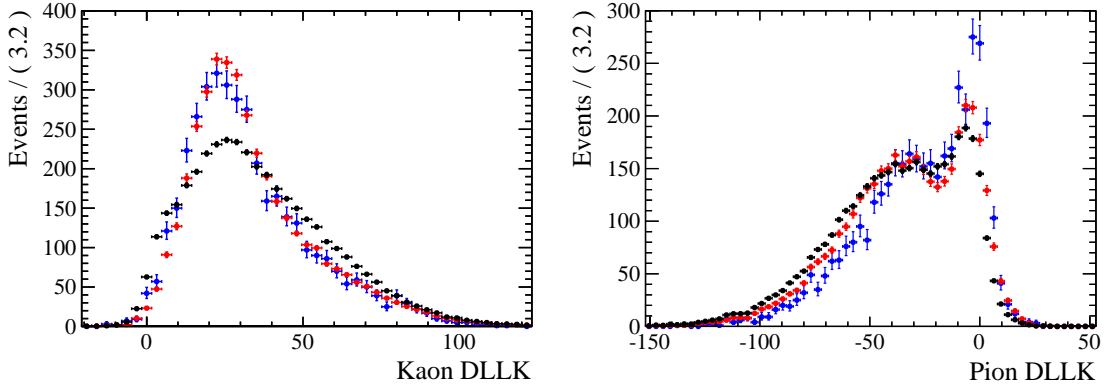


图 4.5 The PIDK distribution, Ξ_{cc}^+ MC(blue), weighted MC calibration sample(red), unweighted MC calibration sample(black)

4.5 Trigger efficiency

The HLT reconstruction is similar to that used offline, so we treat the HLT as well modelled in the MC given the existing systematic errors on tracking etc. However, $L0$ is rather different and is known not to be well modelled. We corrected for this in Section 3.5.5.1. However, there are uncertainties associated with this correction, namely the errors on the efficiencies in the look-up tables and the limited size of our signal MC sample. The efficiencies in the table have very small errors ($\sim 0.1\%$) so the associated systematic uncertainty is negligible. The size of the MC sample does play a role. Since the size of our Λ_c^+ MC sample is much larger than that of the Ξ_{cc}^+ MC, the latter will dominate the error. The method used to calculate the systematic uncertainty can be found in Appendix ??, and the result is found to be 3.27%.

4.6 Systematics related to yield measurement

The signal number is obtained from background subtraction (see Sec. 3.6.3.1), therefore the method used for background estimate and the efficiency of the signal window can be sources of systematics.

Two methods are used for the background estimate and they have very similar outputs, so we do not assign any further systematic uncertainty due to the background estimate method. An inaccurate estimate of the δm resolution could cause an incorrect estimate of the signal window efficiency. To assess the difference between the mass resolution in data and Monte Carlo, the Λ_c^+ data and MC samples are both fitted with a double-Gaussian function, and the weighted resolution is found to be very close (5.11 MeV/ c^2 in MC and

表 4.20 The resonance structures in $\Lambda_c^+ \rightarrow pK^-\pi^+$ decay.

Decay modes	Branching fraction
$p \bar{K}^{*0}$	$(1.6 \pm 0.5)\%$
$\Delta^{++} K^-$	$(8.6 \pm 3.0) \times 10^{-3}$
$\Lambda(1520)\pi^+$	$(1.8 \pm 0.6)\%$
$p K^- \pi^+$ nonresonant	$(2.8 \pm 0.8)\%$
Total	$(5.0 \pm 1.3)\%$

5.75 MeV/ c^2 in data). Hence the scale constant for the mass resolution is 1.12. We apply the constant to the δm resolution and find the efficiency difference is about 2%. This uncertainty is neglected since we already have a systematic uncertainty of about 25%.

The fitting of the control mode could also cause systematic uncertainty. The fit to the Λ_c^+ control mode, shown in Fig. 3.15, is of good quality. The statistical uncertainty on the fit is included in the error on α . Since the systematic uncertainty from efficiency calculation is clearly going to be subdominant, we do not assign further fit systematic uncertainty assigned.

4.7 Decay models

The signal MC was generated with both the Ξ_{cc}^+ and the Λ_c^+ decaying according to a phase-space distribution. This is not quite realistic since probably there are resonance structures in the Ξ_{cc}^+ and the Λ_c^+ decays. For the Λ_c^+ we do have some information on what resonances are present but no proper amplitude model, as shown in Table 4.20. Note that about half of the BF is non-resonant but no proper amplitude model.

For the Ξ_{cc}^+ we have no data. However, we can make reasonable speculation about what known resonances might be present. The list is quite short: $\Sigma_c(2455)^{++} \rightarrow \Lambda_c^+\pi^+$, $\Sigma_c(2520)^{++} \rightarrow \Lambda_c^+\pi^+$, $\Sigma_c(2800)^{++} \rightarrow \Lambda_c^+\pi^+$, $K^*(892)^0 \rightarrow K^-\pi^+$. There is also one resonance that has been seen to decay to $\Lambda_c^+K^-$, namely the $\Xi_c(2930)$. However, this is not considered confirmed in PDG and has not been seen in inclusive $\Lambda_c^+K^-$ so we ignore it here.

To check how the efficiency varies across the Ξ_{cc}^+ Dalitz plot ^①, we define regions where resonances might be present, and compute the expected yield fractions in these

^① Strictly speaking it's not a real Dalitz plot, since the Ξ_{cc}^+ and Λ_c^+ are not pseudoscalars, but it still can be a useful approach.

表 4.21 Signal MC event counts and fractions in various regions of the $\Xi_{cc}^+ \rightarrow \Lambda_c^+ K^- \pi^+$ Dalitz plot after the complete selection, and after applying only the stripping and trigger requirements. The expected fractions are also shown assuming a pure phase-space distribution. (MC PID values are used without calibration/correction.)

Region	Complete selection		Stripping + trigger		Expected
Whole D.P.	23	100%	151	100%	100%
$\Sigma_c(2455)/\Sigma_c(2520)$	4	$(17 \pm 8)\%$	17	$(11 \pm 3)\%$	11%
$\Sigma_c(2800)$	10	$(43 \pm 10)\%$	43	$(28 \pm 4)\%$	22%
$K^*(892)$	9	$(39 \pm 10)\%$	41	$(27 \pm 4)\%$	21%

regions from the proportion of the region to the whole Dalitz plot. The three regions defined are

- $\Sigma_c(2455)/\Sigma_c(2520)$ region: $m(\Lambda_c^+ \pi^+) < 2540 \text{ MeV}/c^2$
- $\Sigma_c(2800)$ region: $2750 < m(\Lambda_c^+ \pi^+) < 2850 \text{ MeV}/c^2$
- $K^*(892)$ region: $846 < m(K^- \pi^+) < 946 \text{ MeV}/c^2$

However, in the end we are limited by Monte Carlo statistics: only 23 signal MC events left after applying all the requirements. The efficiency variation within the Dalitz plot can not be analysed. Results of the expected and measured fraction are shown in Table 4.21. But the point here is that within the big MC statistics error the measured fractions are broadly compatible with the expected fractions, we don't think that quantitative conclusions can be drawn. And also none of these resonant regions shows serious depletion, and in particular that the $\Sigma_c(2455)/\Sigma_c(2520)$ corner is not empty.

No additional uncertainty due to the decay models is assigned: we are fully limited by the signal MC statistics for which there is already a large systematic uncertainty.

4.8 Summary

表 4.22 Summary of systematics

Source of uncertainty	σ_R/R
Tracking efficiency	4.72%
IP Smearing	13.32%
PID calibration	11.76%
Trigger efficiency	3.27%
MC statistics	18.02%
Total uncertainty	25.97%

第 5 章 Variation of the Efficiency Ratio

5.1 Variation of the efficiency ratio with Ξ_{cc}^+ mass

The efficiency ratio depend on the mass of the Ξ_{cc}^+ baryon in two ways. First, the signal efficiency relies on the kinematics of the daughter tracks. A larger Ξ_{cc}^+ mass implies a larger energy release and therefore harder p_T spectrums of the daughter tracks, hence the efficiency may vary as a function of mass. ^① Second, in the yield measurement the signal window is defined as the ± 10 MeV/ c^2 window of the δm value being tested. Since the δm resolution is a function of δm , the signal window cut efficiency also varies with mass hypothesis.

But as for the lifetime, the mass of the Ξ_{cc}^+ is not known a priori. The efficiency ratio should be determined for each δm point in the the range 380 – 880 MeV/ c^2 . The treatments of the efficiency variation are described in the following sections.

5.1.1 Effects from variation of kinematic distributions

The kinematic dependence of the signal efficiency can be investigated using many signal full simulation MC samples with different Ξ_{cc}^+ mass. (An exception is the acceptance efficiency, which can be studied directly through generator-level MC). However, this approach is very time consuming. It turns out the dependence can be estimated with the weighting technique, as detailed below.

For the mass hypothesis m , two generator-level MC samples with $m(\Xi_{cc}^+) = m$ and $m(\Xi_{cc}^+) = 3500$ MeV/ c^2 are generated, and will be denoted as sample A and A_0 in the following text. The p_T distributions of Ξ_{cc}^+ daughters (the Λ_c^+ , the bachelor K , and the bachelor π) of sample A_0 are reweighted to match those of A . The weights obtained are then used to reweight the full MC sample (with $m(\Xi_{cc}^+) = 3500$ MeV/ c^2), then the efficiency for the mass hypothesis m is recomputed.

The binning used for the reweighting is shown in Table 5.1.

^① There are measurements of the Ξ_{cc}^+ mass from the SELEX collaboration. But in the case of lack of confirmation, we still consider the Ξ_{cc}^+ mass to be unknown.

表 5.1 The p_T binning of Ξ_{cc}^+ daughters

Variable	Binning
$\Lambda_c p_T$ [MeV]	[0, 700, 1000, 1450, 1900, 2600, 3300, 4300, 15000]
$K p_T$ [MeV]	[0, 150, 250, 350, 450, 600, 850, 1150, 5000]
πp_T [MeV]	[0, 150, 250, 350, 450, 600, 850, 1150, 5000]

Note only two mass hypotheses are studied directly: $m(\Xi_{cc}^+) = 3300 \text{ MeV}/c^2, 3700 \text{ MeV}/c^2$. Efficiencies for other mass hypotheses will be obtained from linear interpolation.

The selection, PID, and trigger efficiencies are obtained by weighting the full MC as discussed above. For this exercise we don't bother with the full calibration procedure for PID and L0, instead simply taking the efficiencies straight from MC and assuming that data/MC differences are independent of Ξ_{cc}^+ mass.

The results are shown in Table 5.2 and the variation is shown in Fig. 5.1. We find that several components of the efficiency depend on $m(\Xi_{cc}^+)$ —notably the acceptance, stripping, and L0—but that these effects largely cancel out and the overall efficiency ratio only shows a weak dependency on $m(\Xi_{cc}^+)$. Nonetheless this variation is taken into account when setting upper limits.

表 5.2 The acceptance efficiency for different mass hypotheses, and corresponding values of α . Note that the errors are mainly driven by the limited full MC statistics and are highly correlated between the different mass hypotheses. The detail of the calculation of the error can be found in Appendix ??.

-	3300	3500	3700
$\epsilon_{\text{acc}}(\times 10^{-2})$	18.25 ± 0.08	17.67 ± 0.08	17.09 ± 0.08
$\epsilon_{\text{strip}}(\times 10^{-3})$	2.914 ± 0.038	3.168 ± 0.037	3.316 ± 0.041
$\epsilon_{\text{PID}}(\times 10^{-2})$	50.18 ± 0.65	51.47 ± 0.59	51.68 ± 0.64
$\epsilon_{\text{MVA}}(\times 10^{-2})$	56.45 ± 1.26	55.84 ± 1.16	55.53 ± 1.22
$\epsilon_{\text{L0}}(\times 10^{-2})$	7.89 ± 0.91	7.39 ± 0.82	7.07 ± 0.81
$\epsilon_{\text{Hlt}}(\times 10^{-2})$	31.52 ± 5.62	30.26 ± 5.27	31.55 ± 5.58
Ratio to 3500	1.041 ± 0.067	1.000	1.008 ± 0.061
$\alpha[\times 10^{-5}]$	2.285 ± 0.612	2.379 ± 0.618	2.360 ± 0.630

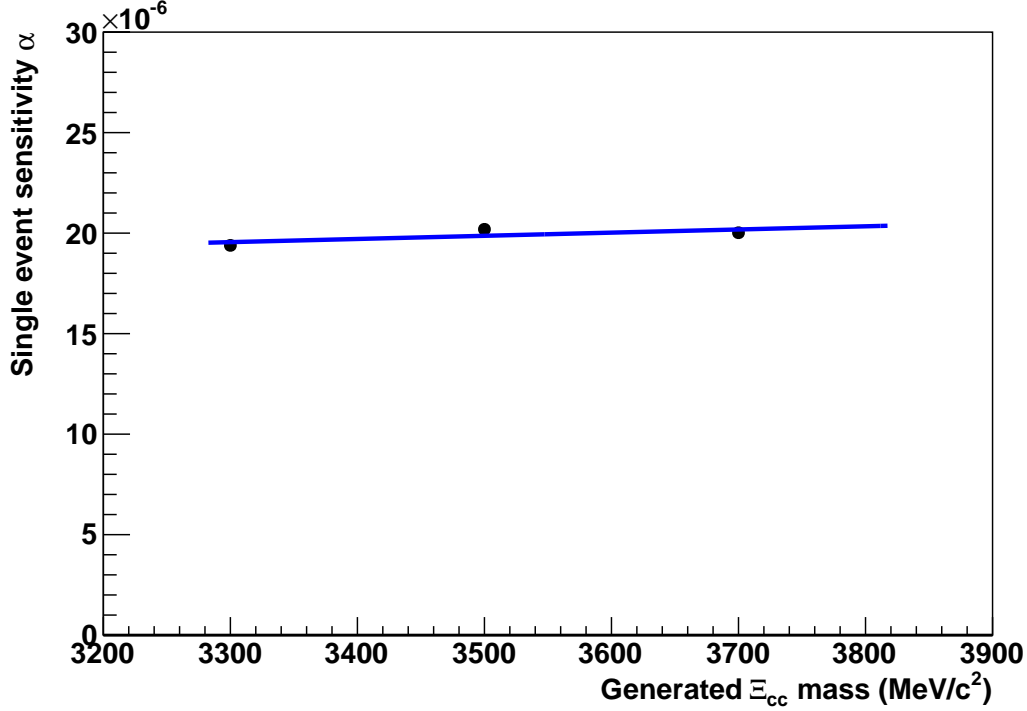


图 5.1 Variation of the single event sensitivity α with $m(\Xi_{cc}^+)$. The points are obtained from a sample of full MC with $m(\Xi_{cc}^+) = 3500 \text{ MeV}/c^2$ plus generator-level MC with $m(\Xi_{cc}^+) = 3300, 3700 \text{ MeV}/c^2$. To obtain the efficiencies at $m(\Xi_{cc}^+) = 3300, 3700 \text{ MeV}/c^2$, the full MC with $m(\Xi_{cc}^+) = 3500 \text{ MeV}/c^2$ is reweighted so that the kinematic distributions of the final state daughters match those at a different Ξ_{cc}^+ mass hypothesis as described in the text.

5.1.2 Correction for Ξ_{cc}^+ mass window

As described in section 3.6.3, candidates must lie within a $\pm 10 \text{ MeV}/c^2$ window of the δm value being tested. The δm lineshape was measured in signal MC for $m(\Xi_{cc}^+) = 3500 \text{ MeV}/c^2$ (corresponding to $\delta m = 580 \text{ MeV}/c^2$) and found to be described by the sum of two Gaussians whose weighted average σ is $4.36 \text{ MeV}/c^2$. Integrating the fitted lineshape across the signal window we find that this corresponds to an efficiency of 96%.

The mass resolution should depend linearly on δm over the energy range in question. Assuming that the resolution of the lineshape do scale linearly with δm , we can compute the efficiency of this signal window cut at any point considered. The efficiency evolves from 99% at $\delta m = 380 \text{ MeV}/c^2$ to 87% at $\delta m = 880 \text{ MeV}/c^2$. Combining this source of inefficiency with the kinematic dependence, we obtain the final δm -dependent correction to α .

5.2 Variation of the efficiency ratio with lifetime

As a result of the lifetime-related cuts in the trigger and stripping selections, the efficiency as well as R strongly depend on the lifetime hypothesis. However, as described in Chapter 1, the Ξ_{cc}^+ lifetime is not accurately predicted but has a considerable theoretical uncertainty. To cover the whole prediction range, we will consider a discrete set of lifetimes (100 fs, 150 fs, 250 fs, 333 fs, 400 fs), recompute the efficiency ratio and hence α for each, and then quote upper limits on R for each. ^①

As the only full signal MC sample we have is generated with a Ξ_{cc}^+ lifetime of 333 fs, a weighting technique is employed to evaluate the efficiency for other lifetimes. For a signal with decay time t , the weight w is defined as:

$$w = \frac{\frac{1}{\tau} e^{-\frac{t}{\tau}}}{\frac{1}{\tau_0} e^{-\frac{t}{\tau_0}}}$$

where τ is the lifetime we want to study, and τ_0 is the lifetime in the current MC sample: $\tau_0 = 333$ fs. The efficiency for a cut therefore is

$$\varepsilon = \frac{\sum_i^{\text{after cut}} w}{\sum_i^{\text{before cut}} w} = \frac{\sum_i^{\text{pass}} w_i}{\sum_i^{\text{pass}} w_i + \sum_j^{\text{fail}} w_j}$$

where the sum i runs over the events which pass the cut and j runs over the events that fail the cut.

The statistical error of the efficiency is not trivial as the binomial distribution. It is found to be:

$$\Delta\varepsilon = \frac{\sqrt{(\sum_j^{\text{fail}} w_j)^2 (\sum_i^{\text{pass}} w_i^2) + (\sum_i^{\text{pass}} w_i)^2 (\sum_j^{\text{fail}} w_j^2)}}{(\sum_i^{\text{pass}} w_i + \sum_j^{\text{fail}} w_j)^2}$$

MC statistics (including that on L0) varies significantly with the lifetime due to limited MC statistics, while others do not depend on lifetime at the first order. Besides, MC statistics is the dominated source of systematic uncertainties. Therefore, we only consider the systematic uncertainties of α due to MC statistics hypothesis; all other systematic uncertainties are left unchanged.

Although parts of the selection criteria are optimised for a specific lifetime, which may lead to a non-optimal selection for other lifetime hypothesis, the selection criteria are

^① The SELEX lifetime value, 33 fs, is not put in consideration. As we can find in the following text, the systematic uncertainty increases very sharply as we move towards smaller lifetime hypotheses. At the lifetime of 33 fs, the systematic uncertainty is so large that the upper limit on R do not contain meaningful information.

the same for all the lifetime. It should be noted that we only have one single δm spectrum and therefore the same measured yield for all lifetime hypotheses.

In the following sections we will consider each part of the efficiency ratio in turn.

5.2.1 Ratio of acceptance efficiency

The generator-level `DaughtersInLHCb` cut requires that the initial four-momenta of all stable charged daughters are in the polar angle range $10\text{mrad} < \theta < 400\text{mrad}$. This is fully independent of the lifetime, and so the value of $\frac{\epsilon_{\text{con}}^{\text{acc}}}{\epsilon_{\text{sig}}^{\text{acc}}}$ obtained in Sec. 3.5.1 applies to all lifetime hypotheses.

5.2.2 Ratio of stripping and offline efficiency

The generated samples are not lifetime-biased, so (in the limit of large statistics) the sum of weights before the cut is the same for all lifetime hypotheses, namely 2.26M. The sums of weights after the stripping and offline selection are given in Table 5.3, along with the resulting efficiency ratios. The ratio drops rapidly as the lifetime increases, since the stripping is very lifetime biased.

表 5.3 The stripping and offline efficiency for different lifetime

τ (fs)	$\sum_i^{\text{after cut}} w_i$	$\epsilon_{\text{sig}}^{\text{sel}}$	$\epsilon_{\text{con}}^{\text{sellacc}} / \epsilon_{\text{sig}}^{\text{sellacc}}$
100	543.44	$(2.40 \pm 0.07) \times 10^{-4}$	50.70 ± 1.41
150	1546.43	$(6.84 \pm 0.12) \times 10^{-4}$	17.81 ± 0.33
250	4461.78	$(1.97 \pm 0.02) \times 10^{-3}$	6.17 ± 0.09
333	7187	$(3.18 \pm 0.04) \times 10^{-3}$	3.84 ± 0.05
400	9363.05	$(4.14 \pm 0.05) \times 10^{-3}$	2.94 ± 0.04

5.2.3 Ratio of PID efficiencies

We repeat the PID calibration procedure for each lifetime hypothesis, using the lifetime-weighted MC sample. The ratio is essentially flat with lifetime (Table 5.4).

表 5.4 The PID efficiency for different lifetime

τ (fs)	$\mathcal{E}_{\text{con}}^{\text{PID sel}} / \mathcal{E}_{\text{sig}}^{\text{PID sel}}$
100	1.680 ± 0.034
150	1.714 ± 0.034
250	1.734 ± 0.034
333	1.748 ± 0.034
400	1.757 ± 0.034

5.2.4 Ratio of MLP efficiency

We use the same MLP selection (trained with MC of $\tau = 333$ fs) and the same cut (MLP > 0.8) for all lifetime hypotheses. The efficiency ratio is basically flat with lifetime, possibly with a gradual increase at very short lifetimes (Table 5.5).

表 5.5 The efficiency of MLP cuts for different lifetime

τ [fs]	$\mathcal{E}_{\text{sig}}^{\text{mlp}}$	$1/\mathcal{E}_{\text{sig}}^{\text{mlp}}$
100	0.512 ± 0.027	1.953 ± 0.102
150	0.554 ± 0.017	1.805 ± 0.056
250	0.565 ± 0.012	1.770 ± 0.038
333	0.557 ± 0.012	1.795 ± 0.037
400	0.549 ± 0.012	1.822 ± 0.040

5.2.5 Ratio of L0 efficiency

The L0 efficiency is obtained from the trigger efficiency tables. Since the lifetime is weighted, so the formula should be modified as

$$\bar{\varepsilon} = \frac{\sum_i w_i n_i \varepsilon_i}{\sum_i w_i n_i}$$

The error can be deduced from error propagation formula, though the expression is rather complicated. The details of the derivation can be found in Appendix ???. This is taken as the systematic error from L0 efficiency. The ratio is shown in Table 5.6 and shows variation with lifetime. (Note that this is not a feature of L0Hadron itself—the trigger is basically lifetime-unbiased—but rather due to the correlation with previous cuts. At short lifetimes, only high-momentum signal survives the impact parameter and FD cuts

in the stripping; at longer lifetimes, softer signal can survive the stripping but is then killed by $L0$ Hadron. This is why the ratio is lower—meaning that the signal efficiency is higher—at short lifetimes.)

 表 5.6 The $L0$ efficiency for different τ

τ [f s]	$\epsilon_{\text{con}}^{\text{trig}} / \epsilon_{\text{sig}}^{\text{trig}}$
100	0.9369 ± 0.0027
150	1.1611 ± 0.0019
250	1.3577 ± 0.0019
333	1.4510 ± 0.0021
400	1.5069 ± 0.0023

5.2.6 HLT1 and HLT2 efficiency

The HLT1 and HLT2 efficiency come from MC. The statistical error are horribly large due to very limited MC size and the weighting procedure (Table 5.7), but the trigger is clearly lifetime-biasing in favour of long-lived Ξ_{cc} .

表 5.7 The HLT efficiency for different lifetime

τ (fs)	HLT efficiency	$\epsilon_{\text{con}}^{\text{HLT}} / \epsilon_{\text{sig}}^{\text{HLT}}$
100	0.107 ± 0.046	2.636 ± 1.134
150	0.187 ± 0.050	1.503 ± 0.403
250	0.268 ± 0.051	1.053 ± 0.203
333	0.303 ± 0.053	0.931 ± 0.165
400	0.323 ± 0.055	0.872 ± 0.153

5.2.7 The systematic error for different lifetime

Most systematic errors for different lifetime are considered to be the same as 333 fs, but $L0$ is an exception, since the p_T of Λ_c^+ daughters will be different. The details of the treatment of this systematic error can be found in Appendix ???. The systematic error for different lifetime are summarized in Table 5.8.

表 5.8 The systematic errors for different lifetime

source of uncertainty	100fs	150fs	250fs	333fs	400fs
Tracking efficiency	4.72%	4.72%	4.72%	4.72%	4.72%
IP Smearing	13.32%	13.32%	13.32%	13.32%	13.32%
PID calibration	11.76%	11.76%	11.76%	11.76%	11.76%
L0 efficiency	12.70%	6.73%	3.89%	3.27%	3.03%
MC statistics	43.46%	27.10%	19.57%	18.02%	17.87%
total uncertainty	48.86%	33.43%	27.12%	25.95%	25.81%

5.2.8 Single event sensitivity for different lifetimes

Finally, putting all of the above together, we obtain the modified values of α and their uncertainties for the five lifetime hypotheses in Table 5.9.

表 5.9 α for different lifetime

τ (fs)	systematic error	$\alpha[\times 10^{-5}]$
100fs	48.86%	(60.036 \pm 29.341)
150fs	33.43%	(14.052 \pm 4.700)
250fs	27.13%	(3.956 \pm 1.074)
333fs	25.95%	(2.379 \pm 0.618)
400fs	25.81%	(1.807 \pm 0.467)

第 6 章 Upper Limit Calculation

We now have all of the procedures to compute upper limits. Given those inputs, we will want to draw a CL_s curve and to find the values of R for which $1 - CL_s = 0.95$ (or 0.9, or some other value). The procedure is as follows:

- We vary R in steps.
- For each value of R , we generate many random configurations, as defined below.
- For each configuration, the value of R is the same but the values of α and b are fluctuated within their uncertainties. This gives individual *expected* background and signal yields for that configuration. We then generate random yields for the background-only and signal-plus-background hypotheses separately and test whether they are less than or equal to n_{obs} .
- From the ensemble of configurations, we measure the fraction of background-only tests with yield below n_{obs} to obtain CL_b , and the fraction of signal-plus-background tests with yield below n_{obs} to obtain CL_{s+b} . Those fractions have (binomial) statistical uncertainties due to the finite number of configurations generated.
- We can then take the ratio CL_{s+b}/CL_b to obtain CL_s for that value of R . As before, there is a statistical error on that value due to the finite number of configurations generated.

In this way we produce a curve of CL_s vs R . We can read off the value of R which gives $CL_s = 0.05$ to obtain the upper limit on R at the 95% CL.

An example scan is shown in Fig. 6.1. Note that, while we can produce example plots like the one shown, we cannot run the full machinery while blind since we need the expected background as an input and this involves data points inside the blinded region. There will therefore be a delay between unblinding and obtaining the final UL results while we run toys.

We will want to produce such an upper limit for each step in δm . Since the efficiency can vary depending on the mass hypothesis, this means using a separate value of α for each δm step. In practice, though, the efficiency is essentially independent of δm . We include this variation in the UL calculation but it has almost no effect.

We will also need to quote separate limits for different lifetime hypotheses as described in the next section.

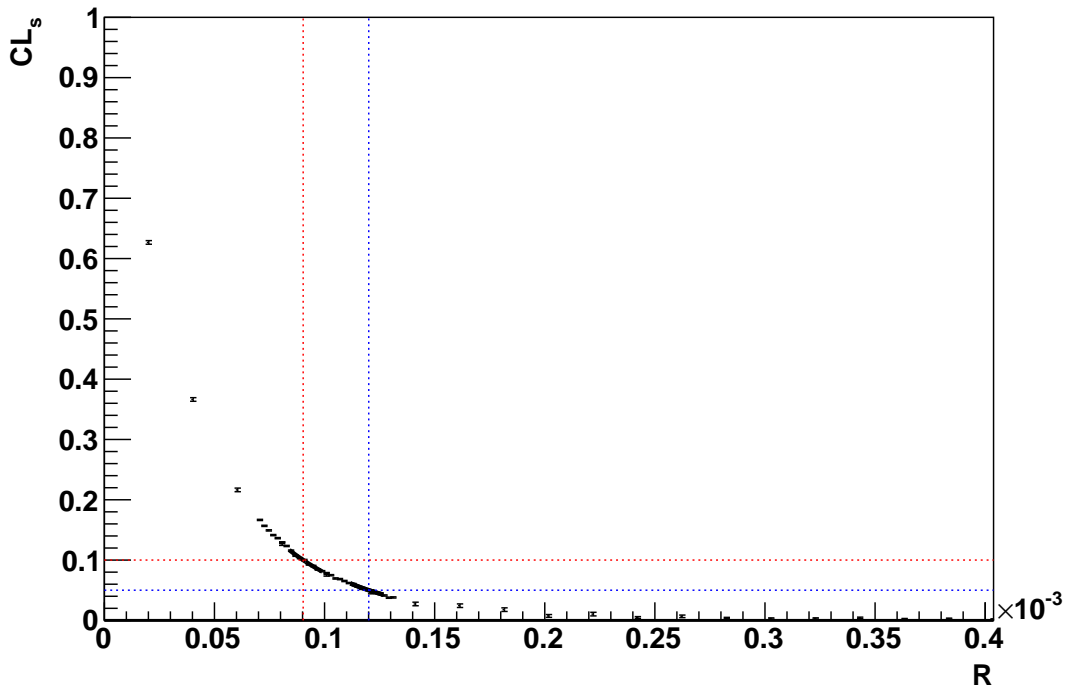


图 6.1 Example CL_s scan for the following input values: $n_{\text{obs}} = 2$, $b = 2.0 \pm 0.1$, $\alpha = (2.019 \pm 0.622) \times 10^{-5}$. The estimated CL_s upper limits for these example parameters are $R < 9.0 \times 10^{-5}$ at 90% CL, $R < 12.0 \times 10^{-5}$ at 95% CL. Toy MC is used to obtain the points, and local exponential fits are used to interpolate between points in the vicinity of $CL_s = 0.1$ and $CL_s = 0.05$. The error bars are due to finite MC statistics—note that the density of points and their statistical uncertainties are not uniform across the plot.

第 7 章 Results

The raw δm spectra of Ξ_{cc}^+ candidates are shown in Fig. 7.1: no strong peak is seen. Applying the yield measurement procedures described in Sec. 3.6.3, we obtain the signal yield spectra shown in Fig. 7.2. The yields fluctuate around zero but do not show a large excess. The local significance and local p-values (before LEE correction) are shown in Figs. 7.3 and 7.4. The largest local significance seen with the baseline 25-Tiles method is 1.46σ , and with the crosscheck 1D Fit & Count method it is 2.16σ . To account for the Look Elsewhere Effect, we use an ensemble of toy experiments as described in Sec. 3.6.3.5. In the ensemble we find that 99.1% of toys contain a smaller local 25-Tiles p-value than that seen in data, and 52.5% contain a smaller local 1D Fit & Count p-value than that seen in data (illustrated in Figure 7.5). Thus, we have no significant excess above background. We therefore set limits on the quantity R defined in eq. 3-3, following the procedure described in Section ???. The limits obtained are shown in Figure 7.6 and tabulated in Tables 7.1 and 7.2.

表 7.1 Upper limits on R at the 95% CL in blocks of δm with the 25-Tiles method, for a range of lifetime hypotheses. The upper limits across the entire 500 MeV/ c^2 range are also shown.

δm (MeV/ c^2)	100fs	150fs	250fs	333fs	400fs
380–429	1.3e-02	2.7e-03	7.3e-04	4.3e-04	3.3e-04
430–479	1.1e-02	2.4e-03	6.5e-04	3.9e-04	2.9e-04
480–529	1.5e-02	3.2e-03	8.5e-04	5.1e-04	3.9e-04
530–579	1.1e-02	2.3e-03	6.3e-04	3.8e-04	2.9e-04
580–629	1.1e-02	2.3e-03	6.3e-04	3.8e-04	2.9e-04
630–679	1.4e-02	3.0e-03	8.1e-04	4.8e-04	3.7e-04
680–729	9.5e-03	2.0e-03	5.6e-04	3.3e-04	2.5e-04
730–779	1.1e-02	2.3e-03	6.3e-04	3.7e-04	2.8e-04
780–829	1.3e-02	2.7e-03	7.4e-04	4.5e-04	3.3e-04
830–880	1.2e-02	2.6e-03	7.0e-04	4.2e-04	3.2e-04
380–880	1.5e-02	3.2e-03	8.5e-04	5.1e-04	3.9e-04

We also check the mass spectra after requiring an intermediate Σ_c resonance in the decay as described in section 3.6.4. The resulting raw mass spectra are shown in

Fig. 7.7. There is an interesting fluctuation around $\delta m = 550 \text{ MeV}/c^2$ when requiring a $\Sigma_c(2455)^{++}$, but it is not statistically significant.

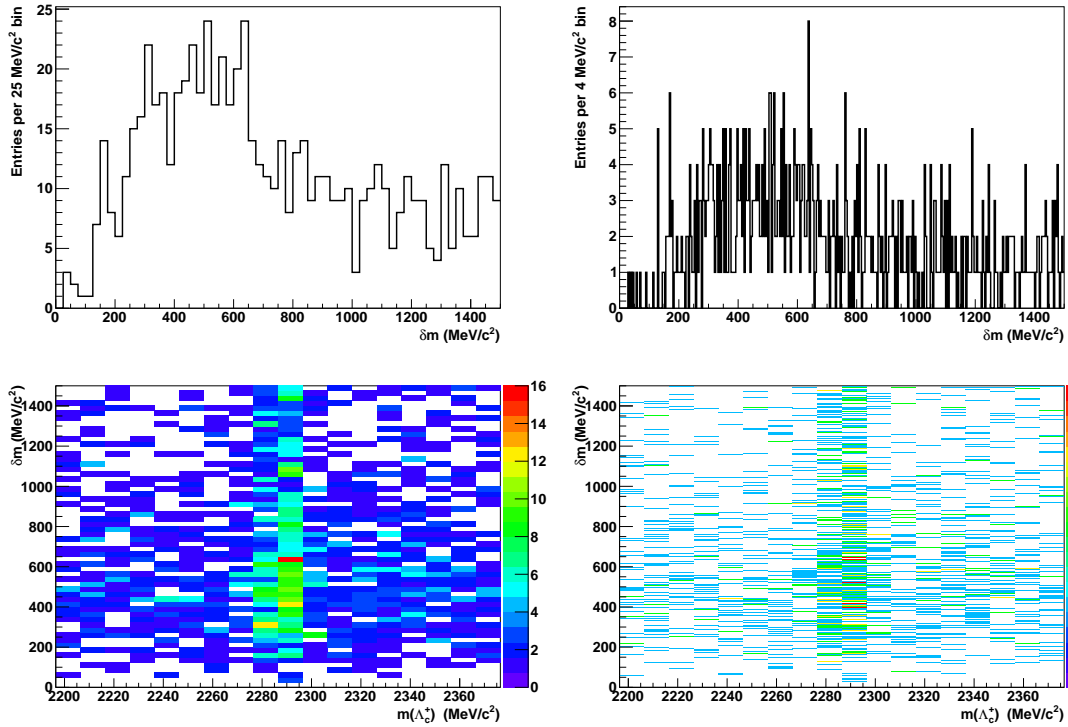


图 7.1 The raw δm spectra of selected Ξ_{cc}^+ candidates in the unblinded data set. The same sample of events is used for all four plots, except that for the 1D δm spectra a cut of $2273 < m(\Lambda_c^+) < 2303 \text{ MeV}/c^2$ has been applied. A finer δm binning is used for the right-hand plots, with bin width a little less than the expected mass resolution.

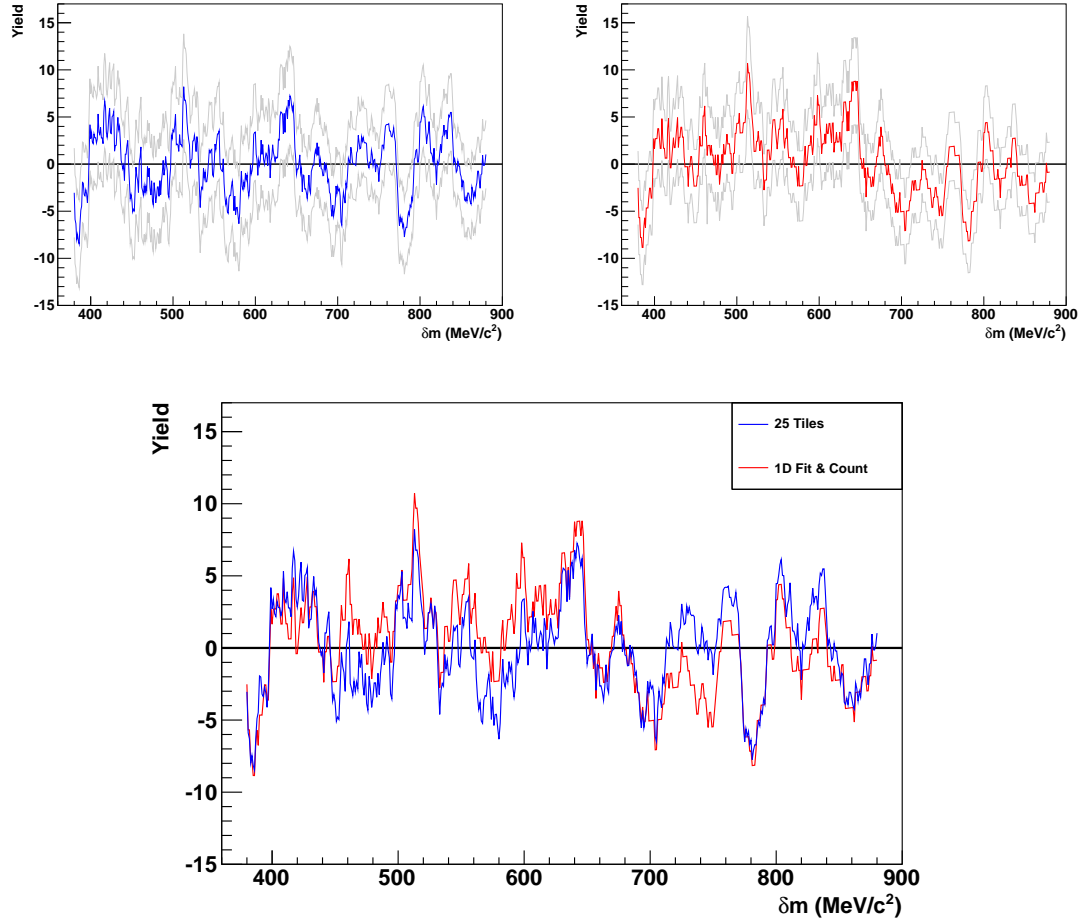


图 7.2 Measured signal yields as a function of δm in the unblinded data set. The upper row shows the estimated signal yield as a coloured line and the $\pm 1\sigma$ statistical error bands as grey lines for the baseline 25-Tiles method (upper left) and the crosscheck 1D Fit & Count method (upper right). The central values of the two methods are compared in the lower plot and found to agree well.

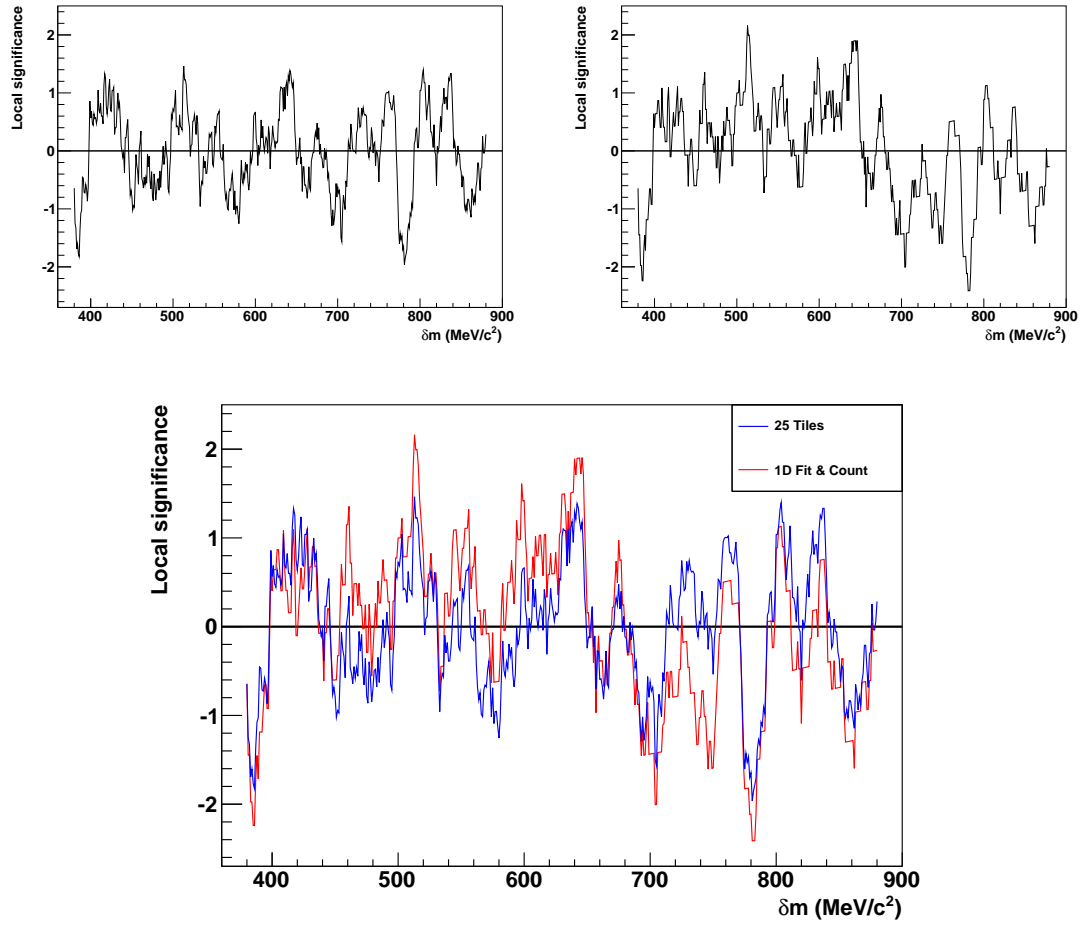


图 7.3 Local signal significance as a function of δm in the unblinded data set, for the baseline 25-Tiles method (upper left), and the crosscheck 1D Fit & Count method (upper right). The results from the two methods are compared in the lower plot.

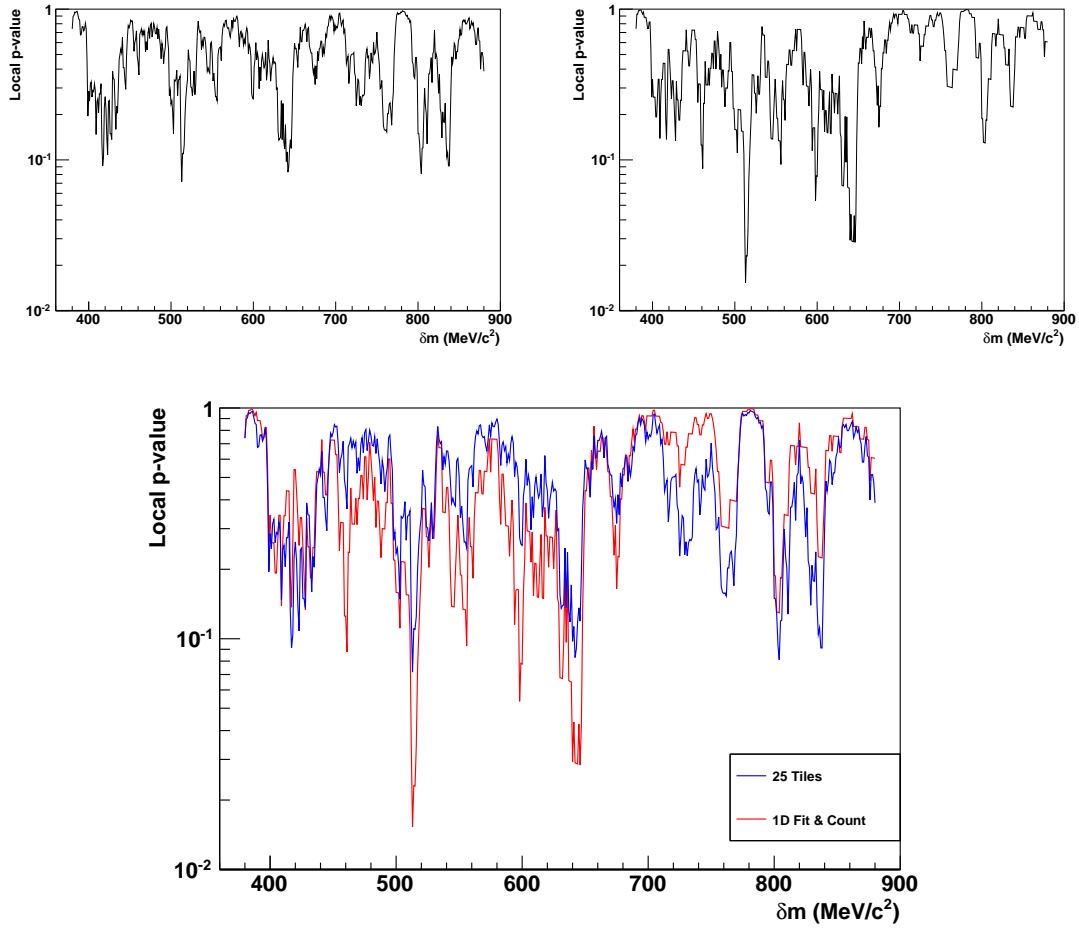


图 7.4 Local p-values as a function of δm in the unblinded data set, for the baseline 25-Tiles method (upper left), and the crosscheck 1D Fit & Count method (upper right). The results from the two methods are compared in the lower plot.

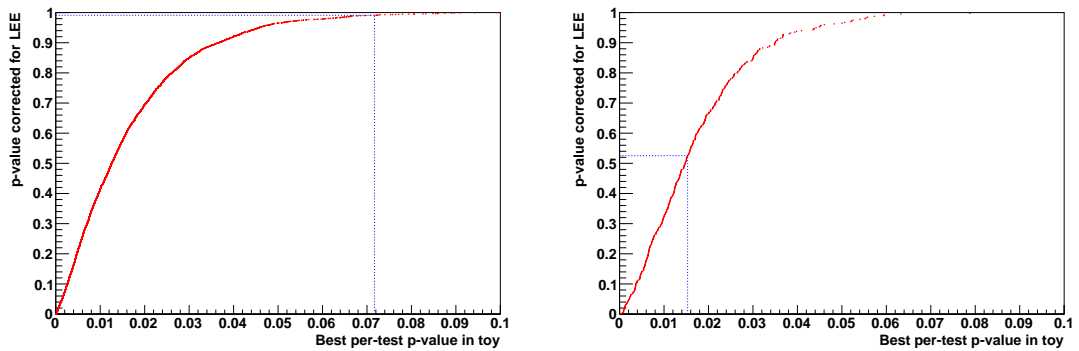


图 7.5 Look Elsewhere Effect correction for the baseline 25-Tiles method (left), and the crosscheck 1D Fit & Count method (right). The dotted lines indicate the smallest local p-value seen in the unblinded data.

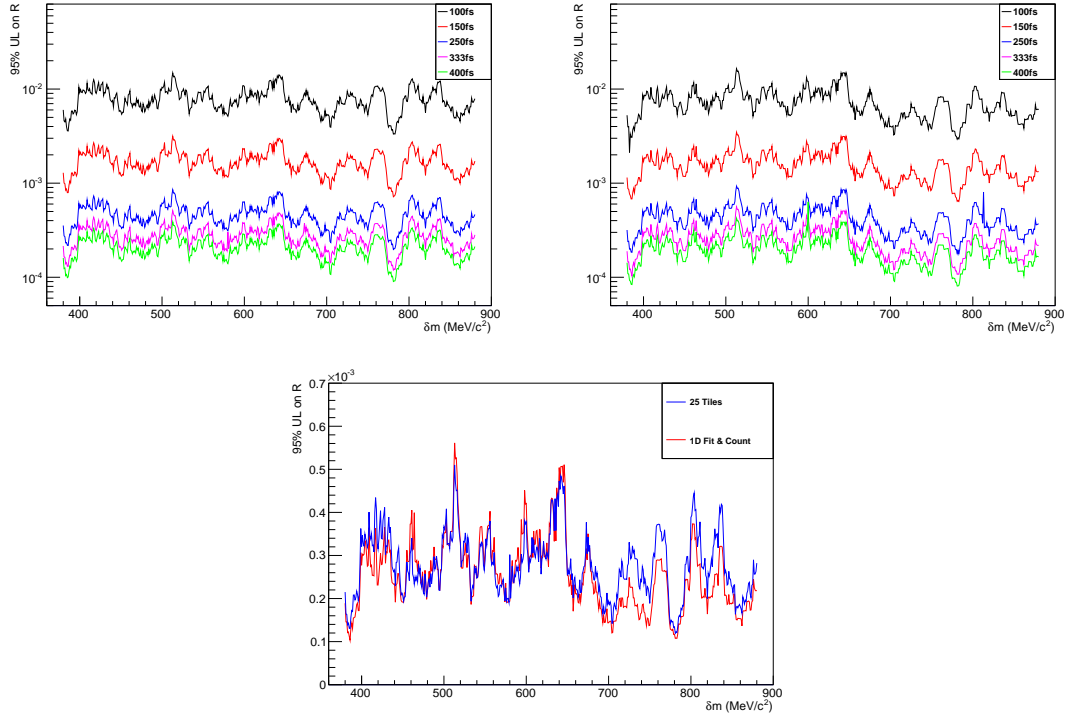


图 7.6 Upper limits on R at the 95% CL, as a function of δm , for the baseline 25-Tiles method (upper left), and the crosscheck 1D Fit & Count method (upper right). For comparison, the limits obtained with the two methods are plotted together for the 333 fs lifetime hypothesis in the lower plot.

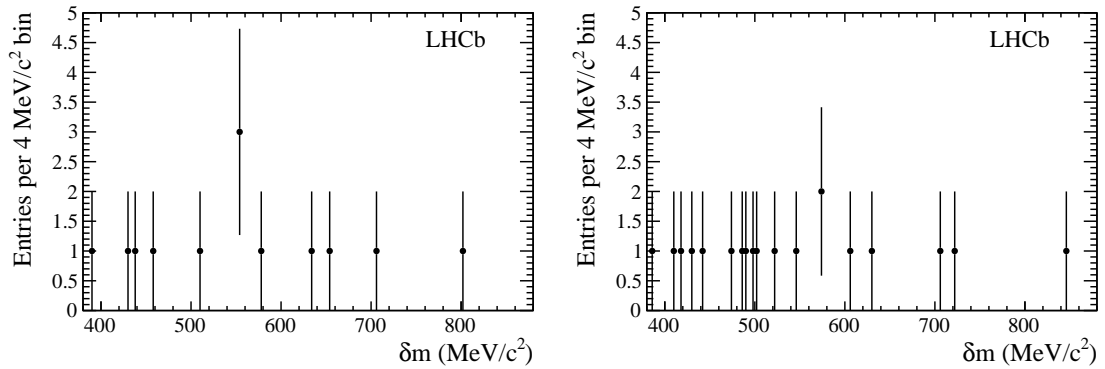


图 7.7 The raw δm spectra of selected Ξ_{cc}^+ candidates in the unblinded data set, requiring an intermediate $\Sigma_c(2455)^{++}$ (left) or $\Sigma_c(2520)^{++}$ (right) resonance in the decay. A cut of $2273 < m(\Lambda_c^+) < 2303$ MeV/c^2 has been applied.

表 7.2 Upper limits on R at the 95% CL in blocks of δm with the crosscheck 1D Fit & Count method, for a range of lifetime hypotheses. The upper limits across the entire 500 MeV/c^2 range are also shown.

δm (MeV/c^2)	100fs	150fs	250fs	333fs	400fs
380–429	1.1e-02	2.3e-03	6.1e-04	3.7e-04	2.8e-04
430–479	1.2e-02	2.5e-03	6.7e-04	4.1e-04	3.2e-04
480–529	1.6e-02	3.5e-03	9.3e-04	5.6e-04	4.2e-04
530–579	1.2e-02	2.5e-03	6.7e-04	4.0e-04	3.1e-04
580–629	1.3e-02	2.8e-03	7.6e-04	4.5e-04	6.3e-04
630–679	1.5e-02	3.2e-03	8.6e-04	5.1e-04	3.9e-04
680–729	7.0e-03	1.5e-03	4.1e-04	2.5e-04	1.9e-04
730–779	8.3e-03	1.8e-03	4.9e-04	2.9e-04	2.2e-04
780–829	1.1e-02	2.3e-03	8.1e-04	3.7e-04	2.8e-04
830–880	9.2e-03	2.0e-03	5.4e-04	3.2e-04	2.4e-04
380–880	1.6e-02	3.5e-03	9.3e-04	5.6e-04	6.3e-04

第 8 章 Conclusion

We have conducted a search for $\Xi_{cc}^+ \rightarrow \Lambda_c^+ K^- \pi^+$ in the 2011 data, using a sample of 0.65 fb^{-1} for which the necessary HLT2 trigger was running. As expected given our efficiency and theory predictions of the cross-section, no signal was observed. We set upper limits on the quantity R , which characterizes the cross-section-times-branching-fraction relative to that of Λ_c^+ , for a range of mass and lifetime hypotheses. We note that the limits quoted explicitly assume that the Ξ_{cc}^+ are produced following the kinematic distributions of the GenXicc model.

8.1 Overview of current experimental status

In this section the mass and lifetime of Ξ_{cc}^+ are assumed to be $3500 \text{ MeV}/c^2$ and 100 fs , and the branching ratio of $\Xi_{cc}^+ \rightarrow \Lambda_c^+ K^- \pi^+$ is assumed to be 5% . Then the upper limit of the production ratio is

$$R \equiv \frac{\sigma(\Xi_{cc}^+) \mathcal{B}(\Xi_{cc}^+ \rightarrow \Lambda_c^+ K^- \pi^+)}{\sigma(\Lambda_c^+)} < 7 \times 10^{-3} @ 95\% C.L. \quad (8-1)$$

The production cross-section of prompt Λ_c^+ , $\sigma(\Lambda_c^+)$, is measured to be $233 \pm 77 \mu\text{b}^{[62]}$, then we find $\sigma(\Xi_{cc}^+) < 30 \mu\text{b}$, which is several orders of magnitude higher than all the predictions. The experimental results unfortunately can not constrain the theoretical models.

The ratio measured by SELEX is $R = 9.6 \times 10^{-2}$, which is significantly higher than the results given by LHCb. But this could also be explained by the production environment, or if the Ξ_{cc}^+ lifetime is indeed very short.

8.2 Prospect of Ξ_{cc}^+ search at LHCb and Belle II

The Ξ_{cc}^+ search at LHCb using 2011 data do not constrain much theoretical models, but we remain optimistic about the sensitivity of the future analysis, which will be improved in three key ways:

1. The 2012 data will be included, which increases the statistics by a factor of 3.
2. Further decay modes, particularly final states with a charmed meson instead of a charmed baryon, for which the HLT and offline efficiency is much better due to the longer lifetime, will be added.

- $\Xi_{cc}^+ \rightarrow \Lambda_c^+ K^- \pi^+$
- $\Xi_{cc}^+ \rightarrow D^0 p K^- \pi^+$
- $\Xi_{cc}^+ \rightarrow D^+ p K^-$
- $\Xi_{cc}^+ \rightarrow \Xi_c^+ \pi^+ \pi^-$
- $\Xi_{cc}^+ \rightarrow \Xi_c^0 \pi^+$

3. Default stripping cuts that require the daughter tracks of the Ξ_{cc}^+ not to point back to the PV, which greatly reduced our sensitivity at short lifetimes in this analysis, will be removed.

A first glance hints that the efficiency of $\Xi_{cc}^+ \rightarrow \Lambda_c^+ K^- \pi^+$ at $\tau(\Xi_{cc}^+) = 100$ fs can be improved by a factor of 8, which will significantly increase our sensitivity.

To have a more quantitative estimate of the future search, the following assumptions will be made:

- The production cross-section of Ξ_{cc}^+ at the LHC is 100 nb.
- The BFs of $\Xi_{cc}^+ \rightarrow \Lambda_c^+ K^- \pi^+$, $\Xi_{cc}^+ \rightarrow D^0 p K^- \pi^+$, $\Xi_{cc}^+ \rightarrow D^+ p K^-$, $\Xi_{cc}^+ \rightarrow \Xi_c^+ \pi^+ \pi^-$, and $\Xi_{cc}^+ \rightarrow \Xi_c^0 \pi^+$ are all 5%.
- The efficiencies of $\Xi_{cc}^+ \rightarrow \Lambda_c^+ K^- \pi^+$, $\Xi_{cc}^+ \rightarrow D^0 p K^- \pi^+$, and $\Xi_{cc}^+ \rightarrow D^+ p K^-$ are the same, i.e. 2×10^{-6} , the efficiencies of $\Xi_{cc}^+ \rightarrow \Xi_c^+ \pi^+ \pi^-$ and $\Xi_{cc}^+ \rightarrow \Xi_c^0 \pi^+$ are 1×10^{-6} .
- The available luminosities for each decay mode
 - $\Xi_{cc}^+ \rightarrow \Lambda_c^+ K^- \pi^+$: 2.5 fb^{-1}
 - $\Xi_{cc}^+ \rightarrow D^0 p K^- \pi^+$: 3 fb^{-1}
 - $\Xi_{cc}^+ \rightarrow D^+ p K^-$: 3 fb^{-1}
 - $\Xi_{cc}^+ \rightarrow \Xi_c^+ \pi^+ \pi^-$: 1 fb^{-1}
 - $\Xi_{cc}^+ \rightarrow \Xi_c^0 \pi^+$: 1 fb^{-1}

Then the expected Ξ_{cc}^+ signal in the 2011 + 2012 dataset is about 7, which is quite difficult for a discovery. After 2015, LHCb will take data at a center-of-mass energy of 13/14 TeV. A data sample of 8 fb^{-1} is expected to be collected by the time 2018. During the run II phase, the whole output of the detector will be read out and the hardware trigger efficiency is expected to be increase significantly. Assuming the efficiency increases by a factor of 5, then the expected signal event will be about 100. This number hasn't considered the improvement on the selection efficiency.

The Belle II experiment will be the main competitor of LHCb in the next decade. The production cross-section of Ξ_{cc}^+ at Belle II will be several order of magnitude smaller ($70 - 230 \text{ fb}^{[57,60]}$), but it will compensate from much higher efficiency ($0.15^{[72]}$) and

much larger total luminosity (at the order of ab^{-1}), The Belle II experiment is expected to collect a luminosity of 5 ab^{-1} around 2019^[135]. Combining all the decay modes, the expected Ξ_{cc}^+ signal will be at the order of 500. This means that Belle II will be a very competitive experiment on doubly charmed baryon search.

参考文献

- [1] J. Jeans. An introduction to the kinetic theory of gases. CUP Archive, 1982.
- [2] J. Dalton. A new system of chemical philosophy, volume 1. Weale, 1840.
- [3] J. J. Thomson. *XL. Cathode Rays*. The London, Edinburgh, and Dublin Philosophical Magazine and Journal of Science, 1897, 44(269):293–316.
- [4] E. Rutherford. *The Scattering of α and β Particles by Matter and the Structure of the Atom*. Phil. Mag, 1911, 21(669):1911.
- [5] J. Chadwick. *Possible existence of a neutron*. Nature, 1932, 129(3252):312.
- [6] H. Yukawa. *On the interaction of elementary particles*. Proc.Phys.Math.Soc.Jap., 1935, 17:48–57.
- [7] S. H. Neddermeyer and C. D. Anderson. *Note on the nature of cosmic-ray particles*. Physical Review, 1937, 51(10):884–886.
- [8] C. M. G. Lattes, H. Muirhead, G. P. Occhialini, and C. F. Powell. *Processes involving charged mesons*. Nature, 1947, 159(4047):694–697.
- [9] G. Rochester and C. Butler. *Evidence for the existence of new unstable elementary particles*. Nature, 1947, 160(855):173.
- [10] M. GELL-MANN and Y. NE'EMAN. *The eightfold way*. Prog Theoret Phys (Kyoto), 1962, 27:949–966.
- [11] M. Gell-Mann. *A Schematic Model of Baryons and Mesons*. Phys.Lett., 1964, 8:214–215.
- [12] G. Zweig. *An $SU(3)$ model for strong interaction symmetry and its breaking. Version I*. CERN-TH-401.
- [13] E. D. Bloom, D. Coward, H. DeStaebler, J. Drees, G. Miller, et al. *High-Energy Inelastic $e p$ Scattering at 6-Degrees and 10-Degrees*. Phys.Rev.Lett., 1969, 23:930–934.
- [14] M. Breidenbach, J. I. Friedman, H. W. Kendall, E. D. Bloom, D. Coward, et al. *Observed Behavior of Highly Inelastic electron-Proton Scattering*. Phys.Rev.Lett., 1969, 23:935–939.
- [15] S. Glashow, J. Iliopoulos, and L. Maiani. *Weak Interactions with Lepton-Hadron Symmetry*. Phys.Rev., 1970, D2:1285–1292.
- [16] J. Augustin et al. *Discovery of a Narrow Resonance in $e^+ e^-$ Annihilation*. Phys.Rev.Lett., 1974, 33:1406–1408.
- [17] J. Aubert et al. *Experimental Observation of a Heavy Particle J* . Phys.Rev.Lett., 1974, 33:1404–1406.
- [18] M. Kobayashi and T. Maskawa. *CP-violation in the renormalizable theory of weak interaction*. Progress of Theoretical Physics, 1973, 49(2):652–657.
- [19] S. Herb, D. Hom, L. Lederman, J. Sens, H. Snyder, et al. *Observation of a Dimuon Resonance at 9.5-GeV in 400-GeV Proton-Nucleus Collisions*. Phys.Rev.Lett., 1977, 39:252–255.

- [20] F. Abe et al. *Observation of top quark production in $\bar{p}p$ collisions*. Phys.Rev.Lett., 1995, 74:2626–2631, [arXiv:hep-ex/9503002](#).
- [21] S. Abachi et al. *Search for high mass top quark production in $p\bar{p}$ collisions at $\sqrt{s} = 1.8$ TeV*. Phys.Rev.Lett., 1995, 74:2422–2426, [arXiv:hep-ex/9411001](#).
- [22] P. W. Higgs. *Broken Symmetries and the Masses of Gauge Bosons*. Phys.Rev.Lett., 1964, 13:508–509.
- [23] S. Glashow. *Partial Symmetries of Weak Interactions*. Nucl.Phys., 1961, 22:579–588.
- [24] A. Salam and J. C. Ward. *Electromagnetic and weak interactions*. Phys.Lett., 1964, 13:168–171.
- [25] S. Weinberg. *A Model of Leptons*. Phys.Rev.Lett., 1967, 19:1264–1266.
- [26] M. Neubert. *Heavy quark symmetry*. Phys.Rept., 1994, 245:259–396, [arXiv:hep-ph/9306320](#).
- [27] D. Ebert, R. Faustov, V. Galkin, and A. Martynenko. *Mass spectra of doubly heavy baryons in the relativistic quark model*. Phys.Rev., 2002, D66:014008, [arXiv:hep-ph/0201217](#).
- [28] A. Martynenko. *Ground-state triply and doubly heavy baryons in a relativistic three-quark model*. Phys.Lett., 2008, B663:317–321, [arXiv:0708.2033](#).
- [29] W. Roberts and M. Pervin. *Heavy baryons in a quark model*. Int.J.Mod.Phys., 2008, A23:2817–2860, [arXiv:0711.2492](#).
- [30] C. Albertus, E. Hernandez, J. Nieves, and J. Verde-Velasco. *Static properties and semileptonic decays of doubly heavy baryons in a nonrelativistic quark model*. Eur.Phys.J., 2007, A32:183–199, [arXiv:hep-ph/0610030](#).
- [31] J. Vijande, H. Garcilazo, A. Valcarce, and F. Fernandez. *Spectroscopy of doubly charmed baryons*. Phys.Rev., 2004, D70:054022, [arXiv:hep-ph/0408274](#).
- [32] S. S. Gershtein, V. V. Kiselev, A. K. Likhoded, and A. I. a. Onishchenko. *Spectroscopy of doubly heavy baryons*. Phys.Rev., 2000, D62:054021.
- [33] E. Bagan, M. Chabab, and S. Narison. *Baryons with two heavy quarks from QCD spectral sum rules*. Phys.Lett., 1993, B306:350–356.
- [34] J.-R. Zhang and M.-Q. Huang. *Doubly heavy baryons in QCD sum rules*. Phys.Rev., 2008, D78:094007, [arXiv:0810.5396](#).
- [35] N. Isgur and M. B. Wise. *Weak Decays of Heavy Mesons in the Static Quark Approximation*. Phys.Lett., 1989, B232:113.
- [36] N. Isgur and M. B. Wise. *WEAK TRANSITION FORM-FACTORS BETWEEN HEAVY MESONS*. Phys.Lett., 1990, B237:527.
- [37] M. A. Shifman, A. Vainshtein, and V. I. Zakharov. *QCD and Resonance Physics. Sum Rules*. Nucl.Phys., 1979, B147:385–447.
- [38] L. Reinders, H. Rubinstein, and S. Yazaki. *Hadron Properties from QCD Sum Rules*. Phys.Rept., 1985, 127:1.
- [39] M. E. Mattson. *Search for baryons with two charm quarks*. FERMILAB-THESIS-2002-03, UMI-30-43381.

- [40] Z.-G. Wang. *Analysis of the $\frac{1}{2}^+$ doubly heavy baryon states with QCD sum rules*. Eur.Phys.J., 2010, A45:267–274, **arXiv:1001.4693**.
- [41] V. Kiselev and A. Likhoded. *Baryons with two heavy quarks*. Phys.Usp., 2002, 45:455–506, **arXiv:hep-ph/0103169**.
- [42] D.-H. He, K. Qian, Y.-B. Ding, X.-Q. Li, and P.-N. Shen. *Evaluation of spectra of baryons containing two heavy quarks in bag model*. Phys.Rev., 2004, D70:094004, **arXiv:hep-ph/0403301**.
- [43] A. Valcarce, H. Garcilazo, and J. Vijande. *Towards an understanding of heavy baryon spectroscopy*. Eur.Phys.J., 2008, A37:217–225, **arXiv:0807.2973**.
- [44] D. Lichtenberg, R. Roncaglia, and E. Predazzi. *Mass sum rules for singly and doubly heavy flavored hadrons*. Phys.Rev., 1996, D53:6678–6681, **arXiv:hep-ph/9511461**.
- [45] R. Lewis, N. Mathur, and R. Woloshyn. *Charmed baryons in lattice QCD*. Phys.Rev., 2001, D64:094509, **arXiv:hep-ph/0107037**.
- [46] J. Flynn, F. Mescia, and A. S. B. Tariq. *Spectroscopy of doubly charmed baryons in lattice QCD*. JHEP, 2003, 0307:066, **arXiv:hep-lat/0307025**.
- [47] G. Bellini, I. I. Bigi, and P. Dornan. *Lifetimes of charm and beauty hadrons*. Phys.Rept., 1997, 289:1–155.
- [48] J. Beringer et al. *Review of Particle Physics (RPP)*. Phys.Rev., 2012, D86:010001.
- [49] C.-H. Chang, T. Li, X.-Q. Li, and Y.-M. Wang. *Lifetime of doubly charmed baryons*. Commun.Theor.Phys., 2008, 49:993–1000, **arXiv:0704.0016**.
- [50] V. Kiselev and A. Likhoded. *Comment on ‘First observation of doubly charmed baryon $\Xi(cc)^+$ ’*. **arXiv:hep-ph/0208231**.
- [51] V. Kiselev, A. Likhoded, and A. Onishchenko. *Lifetimes of doubly charmed baryons: $\Xi(cc)^+$ and $\Xi(cc)^{++}$* . Phys.Rev., 1999, D60:014007, **arXiv:hep-ph/9807354**.
- [52] B. Guberina, B. Melic, and H. Stefancic. *Inclusive decays and lifetimes of doubly charmed baryons*. Eur.Phys.J., 1999, C9:213–219, **arXiv:hep-ph/9901323**.
- [53] A. Likhoded and A. Onishchenko. *Lifetimes of doubly heavy baryons*. **arXiv:hep-ph/9912425**.
- [54] A. Berezhnoy, V. Kiselev, A. Likhoded, and A. Onishchenko. *Doubly charmed baryon production in hadronic experiments*. Phys.Rev., 1998, D57:4385–4392, **arXiv:hep-ph/9710339**.
- [55] V. D. Barger, A. Stange, and R. Phillips. *Four heavy quark hadroproduction*. Phys.Rev., 1991, D44:1987–1996.
- [56] A. F. Falk, M. E. Luke, M. J. Savage, and M. B. Wise. *Heavy quark fragmentation to baryons containing two heavy quarks*. Phys.Rev., 1994, D49:555–558, **arXiv:hep-ph/9305315**.
- [57] J. Ma and Z. Si. *Factorization approach for inclusive production of doubly heavy baryon*. Phys.Lett., 2003, B568:135–145, **arXiv:hep-ph/0305079**.
- [58] C.-H. Chang, C.-F. Qiao, J.-X. Wang, and X.-G. Wu. *Estimate of the hadronic production of the doubly charmed baryon $\Xi(cc)$ under GM-VFN scheme*. Phys.Rev., 2006, D73:094022, **arXiv:hep-ph/0601032**.

- [59] G. T. Bodwin, E. Braaten, and G. P. Lepage. *Rigorous QCD analysis of inclusive annihilation and production of heavy quarkonium*. Phys.Rev., 1995, D51:1125–1171, **arXiv:hep-ph/9407339**.
- [60] V. Kiselev, A. Likhoded, and M. Shevlyagin. *Double charmed baryon production at B factory*. Phys.Lett., 1994, B332:411–414, **arXiv:hep-ph/9408407**.
- [61] C.-H. Chang, J.-P. Ma, C.-F. Qiao, and X.-G. Wu. *Hadronic production of the doubly charmed baryon $\Xi(cc)$ with intrinsic charm*. J.Phys., 2007, G34:845, **arXiv:hep-ph/0610205**.
- [62] R. Aaij et al. *Prompt charm production in pp collisions at $\sqrt{s} = 7$ TeV*. Nucl.Phys., 2013, B871:1–20, **arXiv:1302.2864**.
- [63] J. Russ et al. *First charm hadroproduction results from SELEX*. CMU-HEP-98-07, DOE-ER-40682-103, **arXiv:hep-ex/9812031**.
- [64] M. Mattson et al. *First observation of the doubly charmed baryon Ξ_{cc}^+* . Phys.Rev.Lett., 2002, 89:112001, **arXiv:hep-ex/0208014**.
- [65] E. Gross and O. Vitells. *Trial factors or the look elsewhere effect in high energy physics*. Eur.Phys.J., 2010, C70:525–530, **arXiv:1005.1891**.
- [66] A. Ocherashvili et al. *Confirmation of the double charm baryon $\Xi_{cc}^+(3520)$ via its decay to pD^+K^-* . Phys.Lett., 2005, B628:18–24, **arXiv:hep-ex/0406033**.
- [67] J. Engelfried. *SELEX: Recent Progress in the Analysis of Charm-Strange and Double-Charm Baryons*. eConf, 2006, C0610161:003, **arXiv:hep-ex/0702001**.
- [68] J. Engelfried. *The experimental discovery of double-charm baryons*. Nucl.Phys., 2005, A752:121–128.
- [69] J. Engelfried. *Doubly charmed baryon results from SELEX*. <http://www.ectstar.eu/sites/www.ectstar.eu/files/talks/after-jurgen-feb13.pdf>.
- [70] S. Ratti, J. Link, M. Reyes, P. Yager, J. Anjos, I. Bediaga, C. Gobel, J. Magnin, A. Massafferri, J. de Miranda, et al. *New results on c-baryons and a search for cc-baryons in FOCUS*. Nuclear Physics-Section B-PS-Proceedings Supplements, 2003, 115:33–36.
- [71] R. Chistov et al. *Observation of new states decaying into $\Lambda_c^+K^-\pi^+$ and $\Lambda_c^+K_S^0\pi^-$* . Phys.Rev.Lett., 2006, 97:162001, **arXiv:hep-ex/0606051**.
- [72] Y. Kato et al. *Search for doubly charmed baryons and study of charmed strange baryons at Belle*. BELLE-PREPRINT-2013-29, KEK-PREPRINT-2013-57, **arXiv:1312.1026**.
- [73] L. Evans and P. Bryant. *LHC Machine*. JINST, 2008, 3:S08001.
- [74] D. Saxon. *The Higgs boson: what, why, how?* <http://www.maths.ed.ac.uk/~aar/rsesaxon.pdf>.
- [75] D. Abbaneo et al. *A Combination of preliminary electroweak measurements and constraints on the standard model*. SLAC-REPRINT-2000-098, CERN-EP-2000-016.
- [76] M. E. Peskin and J. D. Wells. *How can a heavy Higgs boson be consistent with the precision electroweak measurements?* Phys.Rev., 2001, D64:093003, **arXiv:hep-ph/0101342**.
- [77] H. E. Haber and G. L. Kane. *The Search for Supersymmetry: Probing Physics Beyond the Standard Model*. Phys.Rept., 1985, 117:75–263.
- [78] *PROTON SOURCE*. <http://www.lhc-closer.es/1/3/10/0>.

- [79] *The CERN Hadron Ion Sources*. <http://linac2.home.cern.ch/linac2/sources/source.htm>.
- [80] C. Hill, M. Vretenar, E. Tanke, and A. Lombardi. *Present performance of the CERN proton linac*.
- [81] A. Feschenko, C. Hill, A. Lombardi, A. Liou, R. Scrivens, et al. *Tests of the CERN proton linac performance for LHC-type beams*. CERN-PS-2000-053-PP.
- [82] G. Aad et al. *The ATLAS Experiment at the CERN Large Hadron Collider*. JINST, 2008, 3:S08003.
- [83] S. Chatrchyan et al. *The CMS experiment at the CERN LHC*. JINST, 2008, 3:S08004.
- [84] J. Alves, A. Augusto et al. *The LHCb Detector at the LHC*. JINST, 2008, 3:S08005.
- [85] K. Aamodt et al. *The ALICE experiment at the CERN LHC*. JINST, 2008, 3:S08002.
- [86] R. Aaij et al. *Measurement of J/ψ production in pp collisions at $\sqrt{s} = 7$ TeV*. Eur.Phys.J., 2011, C71:1645, **arXiv:1103.0423**.
- [87] M. Krasowski, M. Kucharczyk, W. Manner, W. Maenner, G. Polok, et al. *Primary vertex reconstruction*. CERN-LHCB-2007-011.
- [88] *LHCb Performance Paper*. <https://twiki.cern.ch/twiki/bin/view/LHCb/LHCbPerformancePaper>.
- [89] A. J. et.al. *Measurement of the track finding efficiency*. LHCb-PUB-2011-025.
- [90] P. A. Cherenkov. *Visible emission of clean liquids by action of γ radiation*. Doklady Akademii Nauk SSSR, 1934, 2:451.
- [91] R. Forty and O. Schneider. *RICH pattern recognition*. LHCb-98-040, CERN-LHCb-98-040.
- [92] R. Forty. *RICH pattern recognition for LHCb*. Nucl.Instrum.Meth., 1999, A433:257–261.
- [93] A. Powell. *Reconstruction and PID performance of the LHCb RICH detectors*. Nucl.Instrum.Meth., 2011, A639:260–263.
- [94] M. Adinolfi et al. *Performance of the LHCb RICH detector at the LHC*. Eur.Phys.J., 2013, C73:2431, **arXiv:1211.6759**.
- [95] M. Pivk and F. R. Le Diberder. *sPlot: a statistical tool to unfold data distributions*. Nucl.Instrum.Meth., 2005, A555:356–369, **arXiv:physics/0402083**.
- [96] *LHCb calorimeters: Technical design report*. CERN-LHCC-2000-036.
- [97] G. Bencivenni, G. Felici, F. Murtas, P. Valente, W. Bonivento, et al. *A triple-GEM detector with pad readout for the inner region of the first LHCb muon station*. LHCb-2001-051, CERN-LHCb-2001-051.
- [98] B. Botchine, V. Lazarev, N. Saguidova, A. Vorobyov, A. Kachtchouk, et al. *Wire pad chambers and cathode pad chambers for the LHCb muon system*. LHCb-2000-114, CERN-LHCb-2000-114.
- [99] *LHCb muon system technical design report*. CERN-LHCC-2001-010.
- [100] F. Archilli, W. Baldini, G. Bencivenni, N. Bondar, W. Bonivento, et al. *Performance of the Muon Identification at LHCb*. JINST, 2013, 8:P10020, **arXiv:1306.0249**.
- [101] E. Rodrigues. *The LHCb trigger system*. Nucl.Phys.Proc.Suppl., 2007, 170:298–302.

- [102] R. Aaij, J. Albrecht, F. Alessio, S. Amato, E. Aslanides, et al. *The LHCb Trigger and its Performance in 2011*. JINST, 2013, 8:P04022, **arXiv:1211.3055**.
- [103] A. Barczyk, G. Haefeli, R. Jacobsson, B. Jost, and N. Neufeld. *1 MHz Readout*. LHCb-2005-062, CERN-LHCb-2005-062.
- [104] V. Gligorov, C. Thomas, and M. Williams. *The HLT inclusive B triggers*. LHCb-PUB-2011-016, CERN-LHCb-PUB-2011-016, LHCb-INT-2011-030.
- [105] P. Spradlin. *The LHCb prompt charm triggers*. LHCb-PROC-2013-076, CERN-LHCb-PROC-2013-076, LHCb-PROC-2013-076, CERN-LHCb-PROC-2013-076, **arXiv:1311.7585**.
- [106] G. Barrand, I. Belyaev, P. Binko, M. Cattaneo, R. Chytrcek, et al. *GAUDI - A software architecture and framework for building HEP data processing applications*. Comput.Phys.Commun., 2001, 140:45–55.
- [107] *The GAUSS Project*. <http://lhcb-release-area.web.cern.ch/LHCb-release-area/DOC/gauss>.
- [108] I. Belyaev, P. Charpentier, S. Easo, P. Mato, J. Palacios, et al. *Simulation application for the LHCb experiment*. eConf, 2003, C0303241:TUMT003, **arXiv:physics/0306035**.
- [109] M. Clemencic et al. *The LHCb simulation application, Gauss: Design, evolution and experience*. J.Phys.Conf.Ser., 2011, 331:032023.
- [110] I. Belyaev et al. *Handling of the generation of primary events in Gauss, the LHCb simulation framework*. IEEE Nucl.Sci.Symp.Conf.Rec., 2010, 2010:1155–1161.
- [111] T. Sjöstrand, S. Mrenna, and P. Skands. *PYTHIA 6.4 physics and manual*. JHEP, 2006, 05:026, **arXiv:hep-ph/0603175**.
- [112] C.-H. Chang, J.-X. Wang, and X.-G. Wu. *GENXICC: A Generator for hadronic production of the double heavy baryons $\Xi(cc)$, $\Xi(bc)$ and $\Xi(bb)$* . Comput.Phys.Commun., 2007, 177:467–478, **arXiv:hep-ph/0702054**.
- [113] C.-H. Chang, J.-X. Wang, and X.-G. Wu. *GENXICC2.0: An upgraded version of the generator for hadronic production of double heavy baryons Ξ_{cc} , Ξ_{bc} and Ξ_{bb}* . Comput.Phys.Commun., 2010, 181:1144–1149, **arXiv:0910.4462**.
- [114] X.-Y. Wang and X.-G. Wu. *GENXICC2.1: An Improved Version of GENXICC for Hadronic Production of Doubly Heavy Baryons*. Comput.Phys.Commun., 2013, 184:1070–1074, **arXiv:1210.3458**.
- [115] F. Zhang. *GenXicc, a new generator for Xicc in Gauss*. <http://indico.cern.ch/getFile.py/access?contribId=1&resId=1&materialId=slides&confId=180853>.
- [116] D. J. Lange. *The EvtGen particle decay simulation package*. Nucl. Instrum. Meth., 2001, A462:152–155.
- [117] S. Agostinelli et al. *Geant4: a simulation toolkit*. Nucl. Instrum. Meth., 2003, A506:250.
- [118] J. Allison, K. Amako, J. Apostolakis, H. Araujo, P. Dubois, et al. *Geant4 developments and applications*. IEEE Trans.Nucl.Sci., 2006, 53:270.
- [119] *The BOOLE Project*. <http://lhcb-release-area.web.cern.ch/LHCb-release-area/DOC/boole>.
- [120] *The MOORE Project*. <http://lhcb-release-area.web.cern.ch/LHCb-release-area/DOC/moore>.
- [121] *The BRUNEL Project*. <http://lhcb-release-area.web.cern.ch/LHCb-release-area/DOC/brunel>.

-
- [122] *The DAVINCI Project*. <http://lhcb-release-area.web.cern.ch/LHCB-release-area/DOC/davinci>.
- [123] W. D. Hulsbergen. *Decay chain fitting with a Kalman filter*. Nucl.Instrum.Meth., 2005, A552:566–575, **arXiv:physics/0503191**.
- [124] D. O. Hebb. *The organization of behavior: A neuropsychological theory*. Psychology Press, 2005.
- [125] M. Mohri, A. Rostamizadeh, and A. Talwalkar. *Foundations of machine learning*. MIT Press, 2012.
- [126] A. Hoecker, P. Speckmayer, J. Stelzer, J. Therhaag, E. von Toerne, and H. Voss. *TMVA: the Toolkit for Multivariate Data Analysis with ROOT*. PoS, 2007, ACAT:040, **arXiv:physics/0703039**.
- [127] V. Gligorov. *Background Category*. <https://indico.cern.ch/event/262630/contribution/1/material/slides/0.pdf>.
- [128] B. Liu. *Tracking efficiency*. <https://indico.cern.ch/getFile.py/access?contribId=7&resId=0&materialId=slides&confId=189746>.
- [129] M. Needham. *Tracking Systematic for X(3872)*. <https://indico.cern.ch/getFile.py/access?contribId=4&resId=0&materialId=slides&confId=135014>.
- [130] L. C. group. *L0Calo efficiency*. <https://indico.cern.ch/getFile.py/access?contribId=2&resId=1&materialId=slides&confId=198143>.
- [131] L. C. group. *L0Calo efficiency twiki*. https://twiki.cern.ch/twiki/bin/viewauth/LHCBPhysics/CalorimeterObjectsToolsGroupDOC#L0_Hadron_trigger_efficiencies.
- [132] A. M. Sanchez et al. *Performances of the LHCb L0 Calorimeter Trigger*. LHCb-PUB-2011-026.
- [133] A. M. Sanchez. *Talk on TupleToolL0Calo*. <https://indico.cern.ch/getFile.py/access?contribId=2&resId=0&materialId=slides&confId=217143>.
- [134] L. tracking group. *TrackSmearingTool*. <https://twiki.cern.ch/twiki/bin/viewauth/LHCBPhysics/TrackSmearingTool>.
- [135] D. M. Asner, E. Dart, and T. Hara. *Belle II Experiment Network and Computing*. PNNL-SA-97204, **arXiv:1308.0672**.

致 谢

衷心感谢导师 xxx 教授和物理系 xxx 副教授对本人的精心指导。他们的言传身教将使我终生受益。

在美国麻省理工学院化学系进行九个月的合作研究期间，承蒙 xxx 教授热心指导与帮助，不胜感激。感谢 xx 实验室主任 xx 教授，以及实验室全体老师和同学们的热情帮助和支持！本课题承蒙国家自然科学基金资助，特此致谢。

感谢 THUThesis，它的存在让我的论文写作轻松自在了许多，让我的论文格式规整漂亮了许多。

本科学位论文的致谢和声明分页，硕士、博士学位论文不分页。所以本科可以多写一些，研究生少写一些。

声 明

本人郑重声明：所呈交的学位论文，是本人在导师指导下，独立进行研究工作所取得的成果。尽我所知，除文中已经注明引用的内容外，本学位论文的研究成果不包含任何他人享有著作权的内容。对本论文所涉及的研究工作做出贡献的其他个人和集体，均已在文中以明确方式标明。

签 名：_____ 日 期：_____

个人简历、在学期间发表的学术论文与研究成果

个人简历

1987年8月2日出生于福建省连江县。

2005年9月考入清华大学工程物理系工程物理专业，2009年7月本科毕业并获得工学学士学位。

2009年9月免试进入清华大学工程物理系攻读博士学位至今。

发表的学术论文

[1] The LHCb Collaboration, R. Aaij et al, *Search for the doubly charmed baryon Ξ_{cc}^+* , JHEP, 2013, 1312:090, **arXiv:1310.2538**

[2]